ANNUAL REPORT ON

RADAR IMAGE ENHANCEMENT, FEATURE EXTRACTION AND MOTION COMPENSATION USING JOINT TIME-FREQUENCY TECHNIQUES

Submitted by

Professor Hao Ling

Department of Electrical and Computer Engineering
The University of Texas at Austin
Austin, TX 78712-1084

May 1, 1999

19990524 070

REPORT DOCUMENTATION PAGE

Public reporting burden for this collection of information is estimated to average 1 hour per response, including the time for reviewing instructions, searching existing data sources, gathering and maintaining the data needed, and completing and reviewing the collection of information. Send comments regarding this burden estimate or any other aspect of this collection of information, including suggestions for reducing this burden to Washington Headquarters Services, Directorate for Information Operations and Reports, 1215 Jefferson Davis Highway, Suite 1204, Arlington, VA 22202-4302, and to the Office of Management and Budget, Paperwork Reduction Project (0704-0188), Washington, DC 20503.

1. AGENCY USE ONLY *(Leave blank)*	2. REPORT DATE May 1, 1999	3. REPORT TYPE AND DATES COVERED Annual Report 15 April 1998-14 April99

4. TITLE AND SUBTITLE Annual Report on Radar Image Enhancement, Feature Extraction and Motion Compensation Using Joint Time-Frequency Techniques	5. FUNDING NUMBERS Research Grant ONR N00014-98-1-0615

6. AUTHOR(S)

Hao Ling

7. PERFORMING ORGANIZATION NAMES(S) AND ADDRESS(ES) The University of Texas at Austin Department of Electrical and Computer Engineering Austin, Texas 78712-1084	8. PERFORMING ORGANIZATION REPORT NUMBER No. 1

9. SPONSORING / MONITORING AGENCY NAMES(S) AND ADDRESS(ES) Office of Naval Research Program Officer Ballston Centre Tower One William Miceli 800 North Quincy Street ONR 313 Arlington, VA 22217-5660	10. SPONSORING / MONITORING AGENCY REPORT NUMBER

11. SUPPLEMENTARY NOTES

a. DISTRIBUTION / AVAILABILITY STATEMENT Approved for Public Release Distribution Unlimited	12. DISTRIBUTION CODE

13. ABSTRACT *(Maximum 200 words)*

This Report summarizes the scientific progress on the research grant "Radar Image Enhancement, Feature Extraction, and Motion Compensation Using Joint Time-Frequency Techniques" during the period 15 April 1998-14 April 1999. Progress on removal of interferences due to rotating parts, image formation of measured data, and clutter rejection based on wavelet packets is presented.

14. SUBJECT TERMS Radar imaging, joint time-frequency, wavelet			15. NUMBER OF PAGES 78
			16. PRICE CODE

17. SECURITY CLASSIFICATION OF REPORT Unclassified	18. SECURITY CLASSIFICATION OF THIS PAGE Unclassified	19. SECURITY CLASSIFICATION OF ABSTRACT Unclassified	20. LIMITATION OF ABSTRACT

ANNUAL REPORT ON

RADAR IMAGE ENHANCEMENT, FEATURE EXTRACTION AND MOTION COMPENSATION USING JOINT TIME-FREQUENCY TECHNIQUES

J

Submitted by

Professor Hao Ling

Department of Electrical and Computer Engineering
The University of Texas at Austin
Austin, TX 78712-1084

May 1, 1999

RADAR IMAGE ENHANCEMENT, FEATURE EXTRACTION AND MOTION COMPENSATION USING JOINT TIME-FREQUENCY TECHNIQUES

Project Starting Date: April 15, 1998

Reporting Period: April 15, 1998 – April 14, 1999

Principal Investigator: Professor Hao Ling
(512) 471-1710
ling@ece.utexas.edu

Graduate Students: Y. Wang, J. Li, H. Deng

Research Associate: R. Bhalla (1 month)

A. SCIENTIFIC OBJECTIVES: The objective of this research program is to devise innovative joint time-frequency (JTF) processing concepts for radar image enhancement and physics-based feature extraction. In particular, we shall investigate how JTF techniques can be utilized to enhance synthetic aperture radar (SAR) and inverse synthetic aperture radar (ISAR) imageries by removing artifacts due to uncompensated target motion, complex target scattering physics, articulating target components and clutter and propagation effects. Furthermore, we set out to re-interpret the extracted artifacts in a more meaningful feature space so that they can be utilized to enhance the performance of target identification algorithms. This research is leveraged against our previous JTF work under the Joint Services Electronics Program, as well as our state-of-the-art radar signature simulation capabilities. At the end of this program, we plan to develop a set of JTF-based radar image processing tools in the standard MATLAB environment, so that this work can be easily disseminated to the radar community.

B. SUMMARY OF RESULTS AND SIGNIFICANT ACCOMPLISHMENTS: During the first year of this research program, three areas of investigation have been initiated. First, we have devised a joint time-frequency technique to remove the interference due to fast rotating parts from the ISAR imager of a target. We utilize a chirp-based JTF algorithm to extract Doppler lines in the ISAR image and estimate the

spin rate of the rotating part. Second, we have processed the measurement data from the TIRA radar. We apply the previously developed adaptive JTF algorithm to form high-resolution ISAR images of several air targets. Third, we have begun a study on using the adaptive wavelet packet transform for clutter suppression in SAR imagery. We show that an improved target signal-to-clutter ratio can be achieved in the wavelet domain. The detailed descriptions of these three projects are described below.

Removing Image Artifacts due to Articulating Target Components. It is well known that when rotating components exist on a target such as gimbaled antennas or propeller blades, image artifacts are introduced in the Doppler dimension of the ISAR image [1, 2]. These smeared features oftentimes overshadow the target geometrical features and hinder the proper interpretation of the ISAR image. We have developed a technique to remove such Doppler smear and produce a clear ISAR image of the target based on adaptive joint time-frequency processing [3, 4]. The technique entails adaptively searching for the linear chirp bases that best represent the time-frequency behavior of the signal. This is accomplished by projecting the signal onto all possible chirp bases and finding the one with the maximum projection value. After the optimal basis is found, the signal component associated with this basis is subtracted from the original signal. By iterating this search procedure, the signal can be fully parameterized with a set of chirp basis functions. Since the Doppler frequency due to the rotating component is both larger and more rapidly varying (in dwell time) than that from the target body, the signal components due to the fast rotating part are associated with those chirp bases having large displacement and slope parameters. On the other hand, the signal components due to the target body motion are represented by those chirp bases with relatively small displacement and slope parameters. By sorting these chirp bases according to their slopes and displacements, the scattering due to the fast rotating part can be separated from that due to the target body. Consequently a cleaned ISAR image of the target body can be reconstructed by using only those bases associated with the body motion. Furthermore, robust Doppler information extraction can be achieved by applying the period detection algorithm to the component associated with rotating parts only. We have applied this algorithm to both simulated data from the radar scattering prediction code Xpatch [11]

autocorrelation function versus dwell time of the extracted blade contribution. From this plot, we can determine the periodicity of the signal to be 0.056 s. The reciprocal of the period is 17.7 rps and it corresponds to the product of the blade rotation rate and the number of blades for this target. We believe this algorithm can also be extended to deal with jet engine modulation (JEM), although the jet problem is more challenging due to the high rotation rate of the blades and the electromagnetic propagation effect through the inlet duct structure. This topic is currently under investigation.

Application of JTF Motion Compensation Algorithm to NATO Data. We have devoted some efforts to process the TIRA radar data taken in Germany in November 1997. The objectives of this effort are to test our previously developed adaptive joint time-frequency (AJTF) algorithm [10] for ISAR motion compensation and to identify needed areas of research in ISAR-based target recognition. Our algorithm uses a search and projection technique in the joint (dwell time)-(Doppler frequency) plane to select and track the prominent point scatterers. The higher-order translation and rotation motions are then extracted and compensated for in the data to form a focused image of the target. The motion compensated images are compared against the reference images generated by using the motion information available in the instrumented ARDS data. Furthermore, comparison is also made with the simulated ISAR images of the air target from the radar signature prediction code Xpatch. A set of representative images is shown below. Figs. 2(a), (b) and (c) are the images for a target at azimuth=56° (0° being nose-on) generated using, respectively, AJTF motion compensation, ARDS sensor information and Xpatch simulation. The dynamic range of the displayed images is 55 dB. The look angle information was deciphered from the ARDS data. By comparing Figs. 2(a) and 2(b), we observe that the motion compensated image and the ARDS-derived reference image appear to be in good agreement. While this is true for most angles, we did find that the performance of our motion compensation algorithm depends on the availability of a clear point scatterer in the selected range cell. A general criterion should be further developed to automatically select the range cell that contains a strong, well-isolated point scatterer. This topic is being further pursued. When the Xpatch simulation is compared against the ARDS-derived reference image, the agreement in the prominent target features is fair.

(a) Motion compensated Image using
AJTF processing
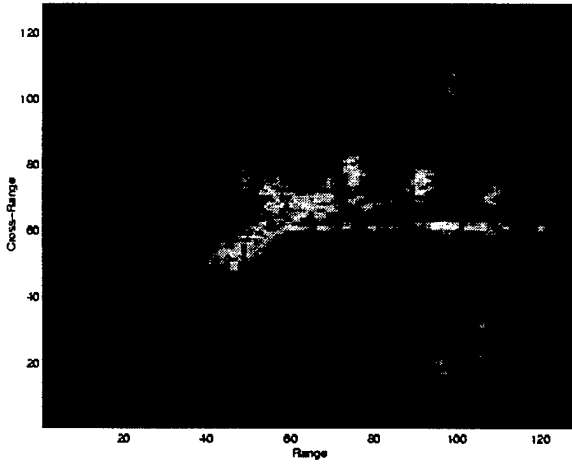
(b) Reference image based on ARDS
motion data
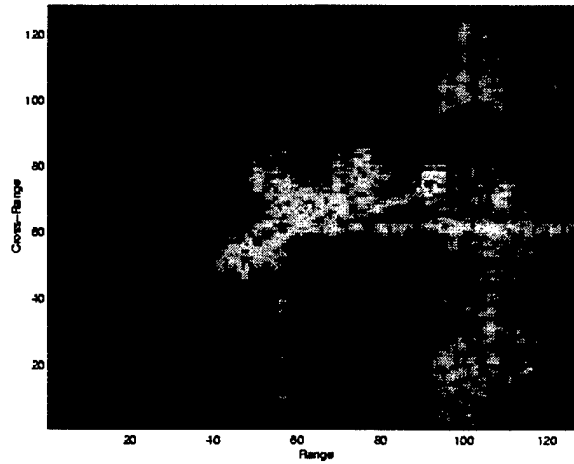
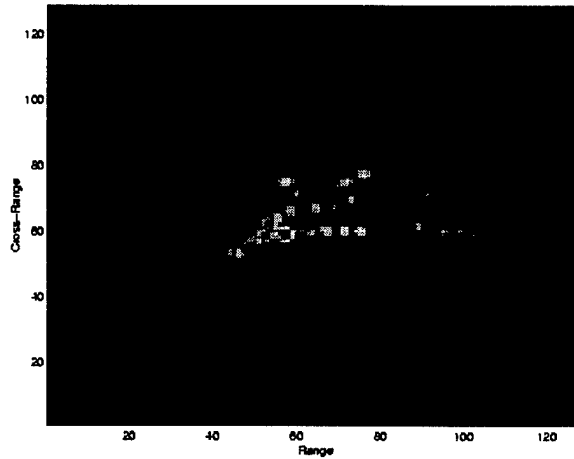(c) Synthetic image from Xpatch
simulation.

Fig. 2. A TIRA target at azimuth=56°.

The Xpatch image is more focused and does not exhibit the diffused characteristics of the measurement data. A more detailed CAD model should improve the quality of the predicted image. Furthermore, the measured images contain strong jet engine modulation (JEM) lines in the frontal look region of the aircraft. Since these features are sensitive to the engine spin rate relative to the radar pulse repetition frequency, an accurate prediction is difficult by Xpatch simulation. We plan to use this set of processed TIRA data to test our algorithm, to be developed under topic 1, for removing JEM artifacts from the measured data in order to unmask the geometrical features of the target.

Clutter Reduction for Radar Images Using Adaptive Wavelet Packet Transform.
Synthetic Aperture Radar (SAR) images of ground targets generally consist of target features and clutters from background scattering. In automatic target recognition (ATR) applications, it is desirable to remove the clutter from the target image before ATR processing. The standard way to suppress clutter is to apply an appropriate threshold level to the whole SAR image. However, this approach assumes that the target signal-to-clutter ratio (SCR) is large enough. Otherwise this direct threshold approach results in either target feature loss or remnant clutter residue. In this work, we set out to develop a decluttering algorithm to automatically extract the target image from a SAR image by maximizing the SCR using the adaptive wavelet packet transform (AWPT) [5]. The wavelet packet basis is a generalization of the conventional wavelet basis [6] and has been applied for image compression [7] and moment matrix sparsification [8]. Our approach is to transform the SAR image to a new domain using the wavelet packet basis. Since a typical target image usually consists of point scatterers and more diffused region features, the multi-scaled wavelet basis is well suited to focus the target image. Clutter image, on the other hand, is statistically uncorrelated from pixel to pixel, and the transformed clutter image under the same set of bases remains unfocused. Therefore, we expect that the SCR can be increased by transforming the original image using an appropriately chosen set of wavelet packet basis. The cost function of our AWPT algorithm is chosen to describe how well the target signal is focused in the transform domain. An efficient basis search algorithm is implemented to find the best wavelet packet basis. Our algorithm is tested using the MSTAR SAR data set [9]. Fig. 3(a) shows an MSTAR image in which the target is a ground vehicle and the clutter is due to vegetation. There are several strong point scatters in the front of the vehicle, but the scattering from the back part is relatively weak. Fig. 3(b) shows the result of applying the direct thresholding method to the image. Fig. 3(c) shows the decluttered image by applying the AWPT algorithm. We choose Daubechies filter with order of 6 as the wavelet filter. By visually comparing Figs. 3(b) and 3(c), we note that some crucial features of the target are kept in the AWPT-processed image. In both processing methods, there is some target information loss. Fig. 3(d) shows the signal-to-clutter ratio
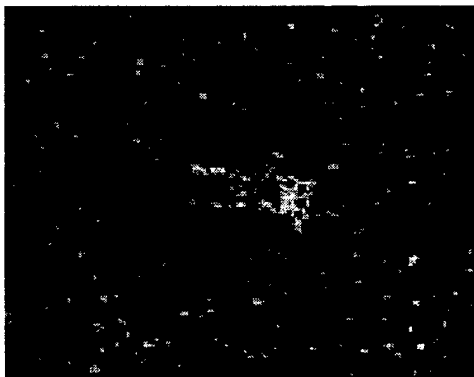
Fig. 3(a). SAR image of a ground
vehicle with clutter

Fig. 3(b). Clutter rejection using
the direct thresholding method.

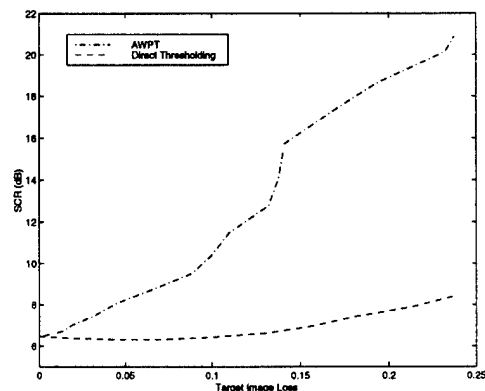Fig. 3(c). Clutter rejection using
the AWPT approach.

Fig. 3(d). SCR vs. target image loss for
the two processing methods.

versus average target image loss for the two processing methods. It is observed that for a
fixed target image loss the AWPT method always achieves a higher SCR value than the
direct thresholding method. Similar results are obtained when the algorithm is applied to
other MSTAR targets. We plan to examine SAR data from other available sources, as
well as to examine the applicability of this technique to ISAR data.

C. FOLLOW-UP STATEMENT:

During the coming year, our research efforts will be devoted to three areas. First, we will continue our work on extracting Doppler effects in ISAR images. We plan to develop algorithms for the more challenging problem of jet engine modulation. The algorithms will be tested using the processed TIRA images that we have generated during the first year. Second, we will devise improved algorithms for ISAR motion compensation to overcome computational time and robustness issues. We also plan to develop a variable dwell time algorithm to maximize cross range resolution and combat target motion jitters encountered in measured ISAR data. It is anticipated that a new measurement data set from the MERIC radar will be made available to us for processing and testing. Third, we will continue our initial study to address the clutter suppression issue using joint time-frequency concepts. We will begin to examine ISAR data containing clutter by requesting and processing ship data from the Navy small craft ATR program.

D. REFERENCES:

1. C. C. Chen and H. C. Andrews, "Target motion induced radar imaging," *IEEE Trans. Aerospace Electron. Syst.*, vol. 16, pp. 2-14, Jan. 1980.

2. A. Ausherman, A. Kozma, J. L. Waker, H. M. Jones and E. C. Poggio, "Developments in radar imaging," *IEEE Trans. Aerospace Electron. Syst.*, vol. 20, pp. 363-400, Apr. 1984.

3. S. Qian and D. Chen, "Signal representation using adaptive normalized Gaussian functions," *Signal Processing*, vol. 36, no. 1, pp. 1-11, Mar. 1994.

4. S. G. Mallat and Z. Zhang, "Matching pursuits with time-frequency dictionaries," *IEEE Trans. Signal Processing*, vol. 41, pp. 3397-3415, Dec. 1993.

5. M. V. Wickerhauser, *Adapted Wavelet Analysis from Theory to Software*, A.K.Peters, Wellesley, Mass. 1994.

6. C. K. Chui, *An Introduction to Wavelets*. Academic Press, New York, 1992.

7. R. R. Coifman, Y. Meyer, and M. V. Wickerhauser, "wavelet analysis and signal processing." In *Wavelets and their applications*, pp. 153-178, Jones and Barlett, Boston, 1992.

8. H. Deng and H. Ling, "Fast solution of electromagnetic integral equations using adaptive wavelet packet transform," to appear in *IEEE Trans. Antennas Propagat.*, Apr. 1999.

9. MSTAR SAR data set, clutter and targets, collected by Sandia National Lab, released by DARPA, Apr. 1997.

E. PUBLICATIONS:

I. LIST OF JOURNAL ARTICLES (ONR supported in whole or in part)

10. Y. Wang, H. Ling and V. C. Chen, "ISAR motion compensation via adaptive joint time-frequency technique," *IEEE Trans. Aerospace Electronic Sys.*, vol. AES-34, pp. 670-677, Apr. 1998.

11. R. Bhalla and H. Ling, "A fast algorithm for simulating Doppler spectra of targets with rotating parts using the shooting and bouncing ray technique," *IEEE Trans. Antennas Propagat.*, vol. AP-46, pp. 1389-1391, Sept. 1998.

12. V. C. Chen and H. Ling, "Joint time-frequency analysis for radar signal and image processing," *IEEE Signal Processing Mag.*, Special Issue on Joint Time-Frequency Analysis, vol. 16, pp. 81-93, Mar. 1999.

II. LIST OF CONFERENCE PROCEEDINGS (ONR supported in whole or in part)

13. Y. Wang, H. Ling and V. C. Chen, "ISAR imaging of targets with fast rotating parts using adaptive joint time-frequency processing," SPIE AeroSense '98, Wavelet Applications, Orlando, FL, Apr. 1998.

14. H. Ling, "Joint time-frequency processing of electromagnetic backscattered data," SPIE AeroSense '98, Wavelet Applications, Orlando, FL, Apr. 1998.

15. Y. Wang, H. Ling and V. C. Chen, "Application of adaptive joint time-frequency processing to ISAR image enhancement and Doppler feature extraction for targets with rotating parts," SPIE 43rd Annual Meeting, Radar Processing, Technology, and Applications, pp. 156-163, San Diego, CA, July 1998.

16. H. Ling, Y. Wang, J. Li and R. Bhalla, "ISAR image formation of TIRA data using adaptive joint time-frequency processing," NATO Sensors and Electronics Technology Symposium on High Resolution Radar Techniques, Granada, Spain, Mar. 1999.

17. H. Deng and H. Ling, "Clutter reduction for synthetic aperture radar images using adaptive wavelet packet transform," to be presented at the International IEEE AP-S Symposium, Orlando, FL, July 1999.

III. LIST OF RELATED PRESENTATIONS

18. "Electromagnetic signature simulation and feature extraction for radar target identification," Naval Research Laboratory, Radar Division Seminar, Washington DC, July 8, 1998.

19. "Signature exploitation research at UT-Austin," Mission Research Corporation, Dayton, OH, Oct. 28, 1998.

20. "Modeling and simulation of scattering and radiation phenomena using scattering centers and radiation centers," Sensor Technologies Integration Laboratory, Air Force Wright Lab, Dayton, OH, Oct. 29, 1998.

21. "Electromagnetic signature simulation and feature extraction for radar target identification," University of Illinois, Signal Processing Seminar, Champaign, IL, Feb. 3, 1999.

22. "Radar image simulation: solving Maxwell's equations for radar target identification," University of Illinois, ECE Department Graduate Seminar, Champaign, IL, Feb. 4, 1999.

IV. LIST OF THESES AND DISSERTATIONS

None.

V. CONTRACTS AND GRANTS

H. Ling, "Advanced studies of electromagnetic scattering," Wright-Patterson Air Force Base (via DEMACO, Inc.), June 1, 1995 - August 1, 1998.

W. Vogel, H. Ling and H. Foltz, "An automated cellular base-station siting tool for urban locations," Texas Advanced Technology Program, January 1, 1996 - August 31, 1998.

R. Chen and H. Ling, "Si CMOS process-compatible optical vias for intra- and inter- multi-chip-module optoelectronic interconnects," Texas Advanced Technology Program, January 1, 1996 - August 31, 1998.

H. Ling, "Advanced research and development for the MSTAR prediction module," Defense Advanced Research Project Agency (via DEMACO, Inc.), June 1, 1995 - January 31, 1999.

H. Ling, "MURI center for computational electromagnetics research," Air Force Office of Scientific Research (via Univ. of Illinois), December 15, 1995 - December 14, 2000.

H. Ling, "Application of model-based signal processing methods to computational electromagnetics simulators," Office of Naval Research, December 1, 1997 - November 30, 2000.

H. Ling, "Radar image enhancement, feature extraction and motion compensation using joint time-frequency techniques," Office of Naval Research, April 15, 1998 - April 14, 2001.

H. Ling, "Moving target modeling and simulation," Air Force Research Laboratory (via DEMACO, Inc.), October 1, 1998 – April 30, 1999.

H. Ling, "Electromagnetic scattering from periodic surfaces," Lockheed Martin Corporate Grant, November 15, 1998 - December 31, 1999.

F. INTERACTIONS/COLLABORATIONS WITH NAVY SCIENTISTS:

Our key collaborator in this program is Dr. Victor Chen of Naval Research Laboratory. Our interactions with Dr. Chen include the exchange of data and algorithms. We have also co-authored a number of publications on JTF processing. It is expected that our close collaboration will continue since it provides an excellent way for us to stay informed of the problems of interest to the Navy and for us to quickly disseminate our research to the Navy labs.

The PI visited Naval Research Laboratory in July of 1998 and presented a seminar to the Radar Division. He had extensive discussion with Dr. William Pala on high-frequency radar signature prediction. Dr. Pala also briefed the PI on the small craft ATR program. We expect to receive the ship ISAR measurements from this program and to explore possible applications of JTF algorithms to the data.

G. NEW DISCOVERIES, INVENTIONS, OR PATENT DISCLOSURES:

None.

H. HONORS AND AWARDS:

Dr. Ling has been elected to IEEE Fellow for 1999 for his "contribution to the development of radar signature prediction and feature extraction techniques."

APPENDIX

Publications Supported by ONR

Research Grant N00014-98-1-0615

ISAR Motion Compensation Via Adaptive Joint Time-Frequency Technique

A novel approach for inverse synthetic aperture radar (ISAR) imaging is presented for both target translational motion and rotational motion nonuniformity compensation. The basic idea is to perform Doppler tracking to individual scatterers via an adaptive joint time-frequency (AJTF) projection technique. After maximizing the projection of the phase function to a set of basis functions in time-frequency plane, the Doppler frequency drift of the strongest scatterer in the range bin is automatically tracked out and the multiple prominent point processing (PPP) scheme is implemented to eliminate both the translational motion error and rotational motion nonuniformity. Further the azimuth spacing can be estimated, which permits polar reformatting of the original collected data.

I. INTRODUCTION

In real-world ISAR (inverse synthetic aperture radar) imaging scenarios, the target being imaged is often engaged in complicated maneuvers that combine translational and rotational motions. Unless a good motion compensation algorithm is implemented, serious blurring can result in the ISAR image formed by Fourier processing. A motion compensation algorithm usually consists of two parts, range alignment and cross range (Doppler) tracking. For various existing motion compensation algorithms, the manner in which range alignment is performed is fairly standard. It is accomplished by tracking the time history of a reference point (such as the peak or the centroid) in the range compressed data and fitting it to a polynomial [1]. There are, however, many different schemes to perform Doppler tracking, such as the subaperture approach [2–4], the cross-range centroid tracking approach [5] and the phase gradient autofocus technique (PGA) [6]. All of these methods consider the Doppler frequency shift for the target as a whole, and apply the same correction vector to all the scatterers in the image. However, when the dwell time is long or when the target exhibits fast maneuvers, the phase error will not be the same for all the scatterers in the image. Therefore, a technique which can automatically track the Doppler frequency shifts of individual scatterers is needed

acquire the complete information about the target motion. We propose a technique which utilitzes joint time-frequency concepts to achieve this goal.

Joint time-frequency techniques have previously been used to address the motion compensation issue [7]. By applying the time-frequency distribution series (TFDS) [8] in place of the Fourier transform engine, the ISAR image can be effectively examined at each time instant, thus eliminating range drift and cross-range smearing. Unfortunately, the TFDS technique is based on the Wigner-Ville distribution and therefore does not preserve the phase information of the original image. In addition, the cross-range resolution achievable in this manner is still less than the full angular aperture of the original data. Recently, the adaptive joint time-frequency (AJTF) concept was introduced by [9 and 10]. One application of this concept in radar image processing is to separate the scattering mechanisms and resonance mechnisms of ISAR image [11]. The basic idea of AJTF is adaptively looking for the basis functions which best represent the joint time-frequency behavior of the signal, thus parametrizing the signal using these bases. Here the AJTF technique is used as a powerful tool to perform Doppler frequency tracking [12]. By using a search and projection procedure in the time-frequency plane, the reference points can automatically be selected and the desired motion parameters can be figured out, thus all the motion error can be well eliminated by multiplying the phase correction vector, interpolating to the uniform azimuth scale, and polar reformatting the original collected data. The original phase information of the image is kept and full aperture resolution is achieved.

This paper is organized as follows. In Section II, we introduce the mathmatical model of motion errors. If the target only contains translational motion, the phase error can be well compensated by tracking one reference point using the AJTF technique in the target. Further, if the target also includes the nonuniform rotational motion, using AJTF technique to track two or three different reference points, a more complex motion compensation model like multiple prominent point processing (PPP) algorithm [13, 14] can be utilized to compensate both translational and rotational motion error. But unlike what original PPP requires, here no multiple dominant, well-isolated point scatterers in their respective range cells are needed. Since the azimuth scale factor can also be obtained in this way, the polar reformatting is possible for the imaging of large targets [2].

I. ANALYTICAL MODEL

We assume that the target rotation outside of the plane between the radar and target is small, and standard range alignment has been applied to the data so that the coarse translational motion has been removed. All the scatterers stay in the right range cells. Then the phase variation as a function of dwell time t (time index of each pulse) in a particular range cell x can be written as

$$f(x,t) = \sum_{k=1}^{N_k} A_k$$
$$\times \exp\left[-j\frac{4\pi f}{c}(R(t) + x_k\cos\theta(t) + y_k\sin\theta(t))\right]$$

$$(1)$$

where N_k is the number of point scatterers and A_k is the magnitude of the kth point scatterer. $R(t)$ is the residual uncompensated translational displacement and $\theta(t)$ is the rotational displacement. Note that either $R(t)$ or $\theta(t)$ is no longer the simple constant or linear relationship which is assumed for ideal no-motion error ISAR imaging; they can be expanded in Taylor series as

$$\begin{cases} R(t) = R_0 + \dot{v}t + \frac{1}{2}v't^2 + \frac{1}{3}v''t^3 + \cdots \\ \theta(t) = \Omega t + \frac{1}{2}\Omega't^2 + \frac{1}{3}\Omega''t^3 + \cdots \end{cases} \quad (2)$$

Taking the first three terms of the Taylor series, we have

$$f(x,t) = \sum_{k=1}^{N_k} A_k \exp\left[-j\frac{4\pi f}{c}(R_0 + (v + y_k\Omega)t \right.$$
$$\left. + \frac{1}{2}(v' + x_k\Omega^2 + y_k\Omega')t^2 + \cdots)\right].$$

$$(3)$$

The simplified phase term can be considered as a sum of polynomials in time where the coefficients of each polynomial are determined by the coordinates of the scatterers and the target motion parameters such as velocity and angular velocity. The constant phase term in (3) has nothing to do with the imaging procedure and thus can be ignored. While the first order term is the way to achieve cross-range resolution, the second and higher order terms are the source of the phase error which cause the image blurring. Hence to estimate and eliminate these higher order phase terms is the main task of the following motion compensation.

III. ADAPTIVE JOINT TIME-FREQUENCY TECHNIQUE

The AJTF technique used here is basically a dechirping procedure just like other conventional time-frequency methods for detecting a chirp signal in the noise [15]. Nevertheless, for a special kind of signal such as radar Doppler frequency, AJTF technique proves to be a more effective and efficient approach to track the Doppler frequency shifts which behave like a bunch of linear or higher order chirps in the time-frequency plane. For simplicity, we illustrate

the procedure of performing AJTF search only for linear chirps. As shown in Fig. 1, if only quadratic phase error terms exist in (3), the radar Doppler frequency shifts via dwell time can be described by those linear chirps with different displacements and slopes. Each chirp represents an individual point scatterer. The goal of AJTF is to map out several strong ones and extract their displacement and slope parameters. For this goal, a set of basis functions are constructed as,

$$h_p(t) = \exp[-j2\pi(f_0 t + \tfrac{1}{2}f_1 t^2 + \cdots)]. \tag{4}$$

They are basically a collection of unit chirps with all possible displacement and slope values, (the dotted line in Fig. 1). Hence projecting the radar Doppler signal to these unit chirps and using a search procedure to maximize the projection value, the basis function which looks most "alike" to the strongest chirp signal will be picked out. The projection procedure is searching the parameters $(f_0, f_1, \ldots)$ which satisfy

$$|B_p|^2 = \max_{f_0, f_1 \cdots} \left| \int f(x,t) h_p^*(t)\, dt \right|^2 \tag{5}$$

where B_p is the complex coefficient of the strongest chirp. Therefore we can extract this strongest chirp signal out from $f(x,t)$ and running the above procedure again to search for the second strongest chirp in the signal. For the specific motion compensation application in this work, we only need search the first strongest scatterer in one range cell, then look for other scatterers in other range cells if more than one scatterer needs to be tracked. The search of the first-order coefficient can be accomplished by using fast Fourier transform (FFT) algorithm, then only a one-dimensional parameter search is required to find f_1, the quadratic phase error. The algorithm can also be extended for the third or higher order phase errors except more computation time is needed. The resolution between chirps is expected to be the Fourier resolution of the full azimuth aperture resolution. It doesn't require that the tracked point scatterer is dominant or well isolated in the range cell.

IV. MODEL FOR MOTION ERROR ELIMINATION

Once the phase information of individual scatterers is measured. The next task is to eliminate those quadratic or higher order phase terms for all the scatterers. Here we implement the model of multiple PPP algorithm to eliminate the phase error step by step.

Considering the right-hand side of the formula (3), the coefficients of quadratic phase terms consist of three parts. The range and cross-range independent terms represent translational motion error, while the cross-range dependent terms represent rotational
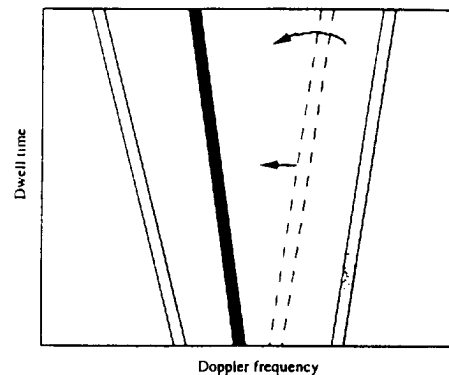

Fig. 1. Search procedure of AJTF processing for radar signal with quadratic phase error.

motion error and the range dependent terms represent wide-angle imaging error. Thus it is possible to determine all the motion parameters using the information provided by three reference scatterers. The basic idea of the multiple PPP algorithm is, suppose that there are three prominent point scatterers whose phase components are known, the translational motion error can be removed by unwrapping the higher order phase component of the first prominent point. Then a nonlinear relationship between the rotation angle and dwell time can be obtained using the phase information of the second prominent points. From this relationship, the uniformly azimuth distributed data can be interpolated from the original collected data in nonuniform azimuth mesh and thus the rotational motion error can be removed. At last, the rotation rate can be estimated by measuring the phase of the third prominent points, so that the polar reformatting can be applied to eliminate the wide-angle imaging error. The limitation of PPP is assuming the availability of target prominent points so that they can be easily separated out from the other scatterers using a windowing technique. The selection and tracking of those points is often done manually. Here, instead of an interactive procedure, AJTF technique is used as a powerful, automatic tool to select and track the reference points. As to detailed procedure to conduct PPP, one can refer to [13, 14].

V. SOME EXAMPLES

We use the simulated step frequency data from a B727 airplane as an example to describe the whole motion compensation procedure. The center frequency of radar is 9 GHz and the bandwidth is 150 MHz. The total number of pulses is 256. After compressing the image in both range and cross-range direction, a total of 64 range cells and 256 cross-range cells image is produced. Fig. 2(a) is the ISAR image after range alignment and cross-range centroid focusing. Since the target contains a significant amount of nonuniform rotational motion, only a part of the
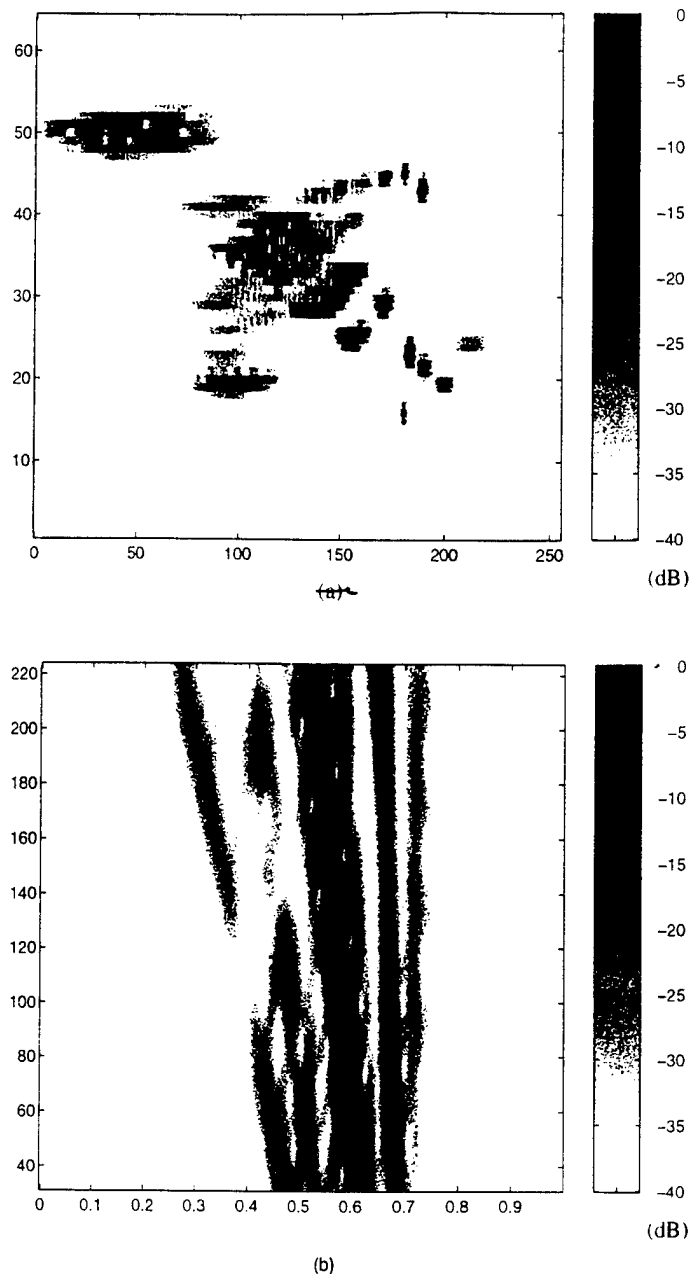
Fig. 2. (a) Simulated B727 ISAR image after range alignment and coarse motion compensation. (b) STFT spectrogram of signal in particular range cell.

airplane is well focused while the part away from the focus are seriously blurred. To describe the underlying mechanism of autofocusing more explicitly, we plot the variation of Doppler frequency versus dwell time in a particular range cell in the time-frequency plane in Fig. 2(b). The short time Fourier transform (STFT) is used to generate the time-frequency spectrogram. We can almost see a bunch of lines in the spectrogram, where each line represents the time-varying phase characteristics of a scattering center in the range cell. For example, the displacement of the line represents the coefficient of the linear phase terms and the slope of the line represents the

coefficient of the quadratic phase term. Unfortunately, it is not possible to extract the desired parameters from such a fuzzy image due to the low resolution of the STFT. Instead, the AJTF technique is employed because of its full azimuth aperture resolution.

First we search the first reference point to be focused in this particular range cell. AJTF automatically pick out the strongest scatterer, which is represented by the strongest line in the spectrogram. Multiplying a phase correction vector to the original signal, the image obtained at this stage is shown in Fig. 3(a). As seen in the time-frequency display of
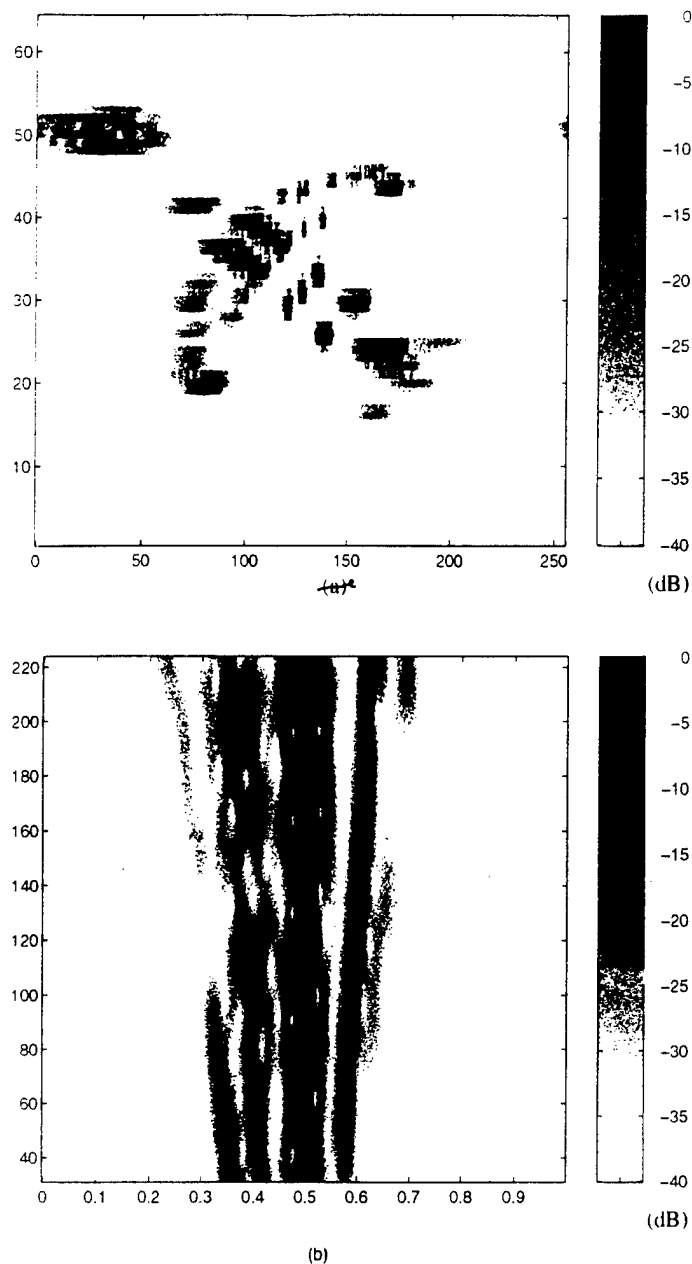
(b)

Fig. 3. (a) ISAR image obtained by focusing on first reference point. (b) STFT spectrogram of signal in particular range cell.

Fig. 3(b), the strongest line has been straightened and shifted to the center of the cross-range axis. This step is only for translational motion removal and thus can be applied directly to the range aligned data in place of conventional translational motion compensation algorithm. For this example, it is used as a finer tuning to the previous focusing algorithm and to prepare a fixed origin for the next steps. As we can see in Fig. 3(a), the image around the origin is well focused while the other part is still defocused due to the rotational error. Thus a second reference point must be selected to determine the rotation rate nonuniformity of the target. The second reference point is selected by searching the strongest scatterer

in another range cell using AJTF. After interpolating the nonuniform azimuth mesh to uniform azimuth mesh, the image becomes well focused everywhere on the target as in Fig. 4(a). As we can see in the time-frequency display of Fig. 4(b), all the lines are straightened, implying that all the quadratic phase terms are eliminated and all the points are well focused. In Fig.4 (c), we show the image from the simulated data without any added motion error as a reference of comparison. For this example, since two point focusing has made the image well focused, which means the wide-angle imaging error is not serious, there is no necessity to do the third point focusing.
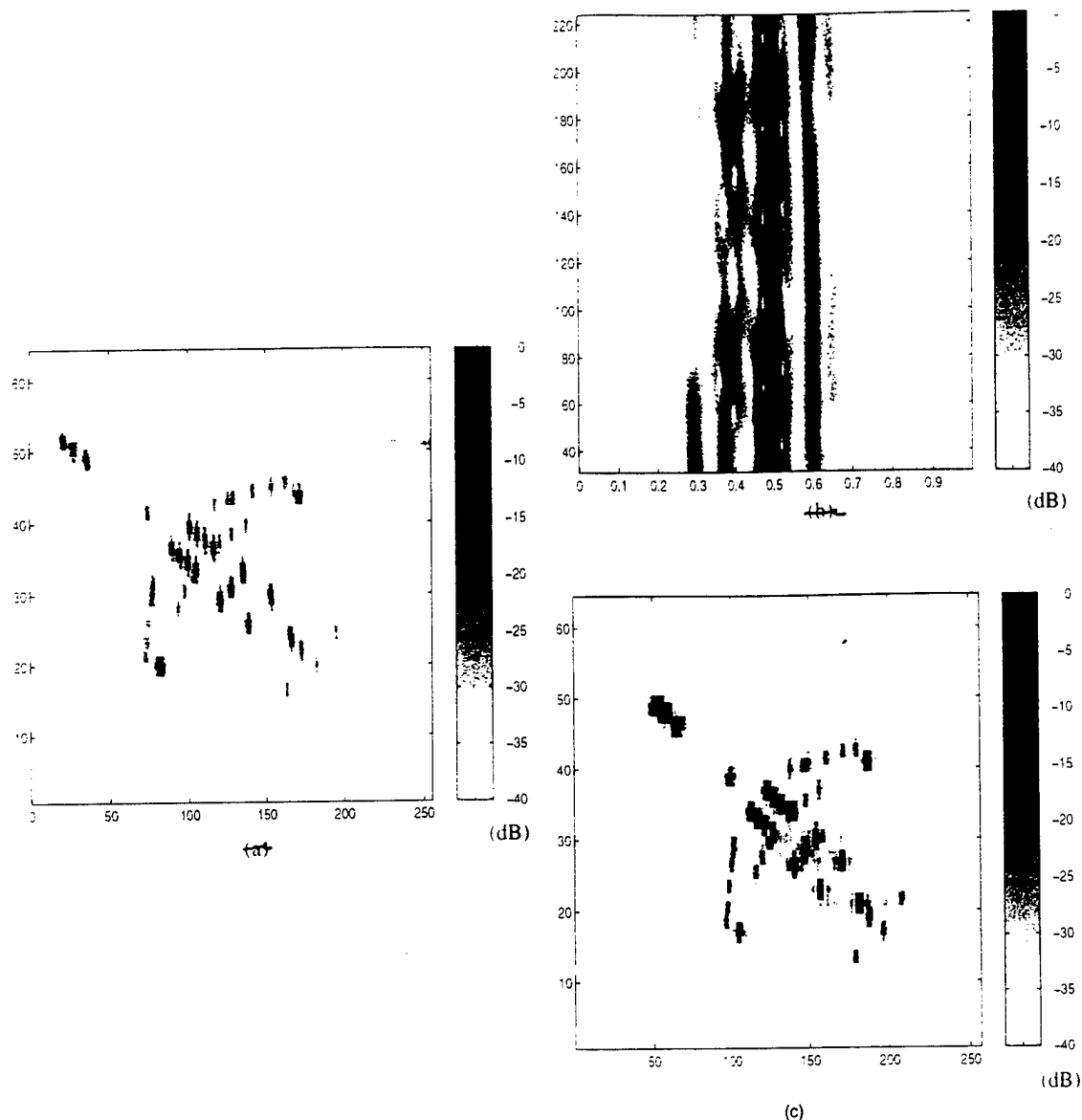
Fig. 4. (a) Final motion compensated B727 ISAR image by focusing on two reference points. (b) STFT spectrogram of signal in particular range cell. (c) Simulated B727 ISAR image without any motion added in.

Another example is a simulated MIG25 airplane. The radar center frequency is 9 GHz and bandwidth is 500 MHz. A total of 64 range cells and 256 cross-range cells are used for the imaging. The coarsely motion compensated image is in Fig. 5(a). After one point focusing algorithm like above, the focus is shifted to about the center of the target, but it is still smeared away from the center, as Fig. 5(b). Consequently, the second point focusing algorithm is applied but doesn't improve at all, which means the target itself doesn't contain much rotational error. The smearing is simply because the large rotation angle makes the polar reformatting necessary. Thus, a third reference point is tracked in the same way and its phase measured. The quadratic phase component provides a reasonable estimate of the angular rotation rate. For this target, the total rotation angle

is estimated to be about 20 deg. Once the angular spacing is found, the original data is polar reformatted to eliminate the range walk and cross-range smearing caused by wide-angle imaging. The final image is obtained in Fig. 5(c). All the scatterers are well focused in their individual range and cross-range cells.

Furthermore, AJTF technique has also been utilized for motion compensation of the measurement data from a few real airplanes. It proves to be rather stable and insensitive to the background clutter.

VI. CONCLUSIONS

An AJTF technique based on time-frequency dechirping concept has been proposed to automatically
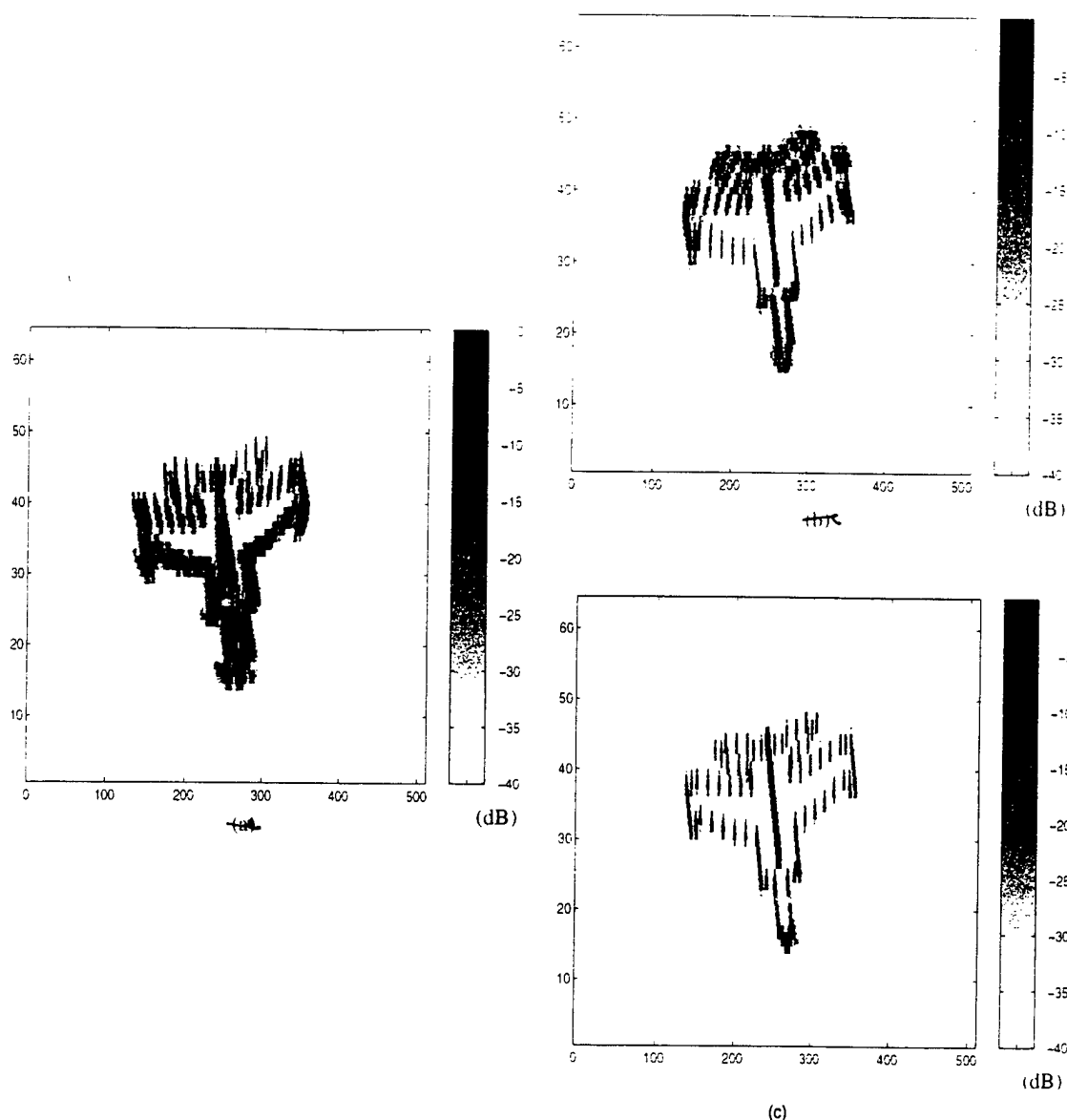
Fig. 5. (a) Simulated MIG25 ISAR image before motion compensation. (b) ISAR image obtained by focusing on first reference point. (c) Final motion compensated ISAR image by focusing on three reference points.

perform Doppler tracking to single or multiple scatterers in ISAR imaging for the moving target. After applying AJTF, several reference point scatterers are automatically selected and their phase components measured. The PPP model thus is applied for the compensation of both translational and rotational motion error, as well as the azimuth spacing estimation. The algorithm has been applied to two simulated airplanes to illustrate the feasibility and the detailed procedure of motion compensation and automatically polar reformatting. The high resolution and stability, and the capability to track individual scatterers prove to be the main advantages of AJTF Doppler tracking.

YUANXUN WANG
HAO LING
Dept. of Electrical and
    Computer Engineering
The University of Texas at Austin
Austin, TX 78712-1084

VICTOR C. CHEN
Airborne Branch
Naval Research Laboratory
Washington, DC 20375

REFERENCES

[1]   Chen, C. C., and Andrews, H. C. (1980)
        Target motion induced radar imaging.
        IEEE Transactions on Aerospace and Electronic Systems,
        AES-16, 1 (Jan. 1980), 2–14.

[2] Ausherman, D. A., Kozma, A., Walker, J. L., Jones, H. M., and Poggio, E. C. (1984)
     Developments in radar imaging.
     IEEE Transactions on Aerospace and Electronic Systems,
     AES-20, 4 (July 1984), 363–400.
[3] Jain, A., and Patel, I. (1992)
     SAR/ISAR imaging of a nonuniformly rotating target.
     IEEE Transactions on Aerospace and Electronic Systems,
     28, 1 (Jan. 1992), 317–321.
[4] Calloway, T. M., and Donohoe, G. W. (1994)
     Subaperture autofocus for synthetic aperture radar.
     IEEE Transactions on Aerospace and Electronic Systems,
     30, 2 (Apr. 1994), 617–621.
[5] Itoh, T., Sueda, H., and Watanabe, Y. (1996)
     Motion compensation for ISAR via centroid tracking.
     IEEE Transactions on Aerospace and Electronic Systems,
     32, 3 (July 1996), 1191–1197.
[6] Wahl, D. E., Eichel, P. H., Ghiglia, D. C., and Jakowatz, C. V., Jr. (1994)
     Phase gradient autofocus—A robust tool for high
     resolution SAR phase correction.
     IEEE Transactions on Aerospace and Electronic Systems,
     30, 3 (July 1994), 827–835.
[7] Chen, V. C. (1995)
     Reconstruction of inverse synthetic aperture images using
     adaptive time-frequency wavelet transforms.
     SPIE Proceedings on Wavelet Application, **2491** (1995),
     373–386.
[8] Qian, S., and Chen, D. (1994)
     Decomposition of the Wigner-Ville distribution and
     time-frequency distribution series.
     IEEE Transactions on Signal Processing, **42,** 10 (Oct.
     1994), 2836–2842.
[9] Qian, S., and Chen, D. (1994)
     Signal representation using adaptive normalized Gaussian
     functions.
     Signal Processing, **36** (Mar. 1994), 1–11.
[10] Mallat, S. G., and Zhang, Z. (1993)
     Matching pursuits with time-frequency dictionaries.
     IEEE Transactions on Signal Processing, **41** (Dec. 1993),
     3397–3415.
[11] Trintinalia, L. C., and Ling, H. (1997)
     Joint time-frequency ISAR using adaptive processing.
     IEEE Transactions on Antennas and Propagation, **45,** 2
     (Feb. 1997), 221–227.
[12] Ling, H., Wang, Y., and Chen, V. C. (1997)
     ISAR image formation and feature extraction using
     adaptive joint time-frequency processing.
     SPIE Proceedings on Wavelet Application, **3078** (1997).
[13] Werness, S., Carrara, W., Joyce, L., and Franczak, D. (1990)
     Moving target imaging algorithm for SAR data.
     IEEE Transactions on Aerospace and Electronic Systems,
     26, 1 (Jan. 1990), 57–67.
[14] Carrara, W. G., Goodman, R. S., and Majewski, R. M.
     (1995)
     *Spotlight Synthetic Aperture Radar: Signal Processing
     Algorithms.*
     Boston: Artech House, 1995.
[15] Wood, J. C., and Barry, D. T. (1994)
     Radon transformation of time-frequency distributions for
     analysis of multicomponent signals.
     IEEE Transactions on Signal Processing, **42,** 11 (Nov.
     1994), 3166–3177.

A Fast Algorithm for Simulating Doppler Spectra of Targets with Rotating Parts Using the Shooting and Bouncing Ray Technique

Rajan Bhalla and Hao Ling

Abstract—We present a fast algorithm for the shooting and bouncing ray technique to simulate the Doppler spectra of targets with rotating parts. The fast algorithm gives an order of magnitude speedup in computation time while maintaining good agreement with the brute-force results.

Index Terms—Doppler effect, geometrical theory of diffraction, rotating bodies.

I. INTRODUCTION

It is well known that when rotating parts exist on a target such as propellers or rotors, additional features are introduced in the Doppler frequency spectra. These features give valuable information about the structure and motion of the rotating part and can be utilized for target identification applications [1]–[3]. Therefore it is important to develop the capability to simulate this effect from first-principle electromagnetics and to relate the observed effects to the target structure [4], [5]. In this paper, we present a fast method to compute the Doppler spectra of complex targets using the shooting and bouncing ray (SBR) technique [6]–[8]. The standard methodology to generate the Doppler spectra requires the computation of the scattered field at different time snapshots of the target as the moving part undergoes motion. The resulting time-varying scattered field is then Fourier transformed to arrive at the Doppler spectrum. From the SBR simulation perspective, each time snapshot on the target with a different moving part position is a new electromagnetic problem and requires that the whole computation be carried out from scratch. This can be very computationally intensive for a complex target. For example, a typical helicopter rotor having a blade length of 20 ft and

rotating at 350 rpm must be sampled in time at an interval of 0.34 ns or less to avoid aliasing in the Doppler spectrum. In order to map out one complete rotor revolution at 10 GHz, approximately 5110 time snapshots of the target are needed. If we use SBR to carry out the scattering calculation at each rotor position, it would take roughly 100 days (5110 × 30 min/run on a typical workstation) to compute the Doppler spectra at just one look angle. In this work, we present a fast Doppler simulation algorithm for the SBR method. The basic idea is to take advantage of the instantaneous Doppler information available for each ray being traced through the target. By adjusting for the differential phase difference due to target motion on a ray-by-ray basis, it is possible to generate the time snapshots of the target at M nearby time instances from ray tracing at only one time snapshot. Thus, we achieve a saving of M ray-tracing operations. A similar idea has been devised earlier by us to the angular extrapolation of range profiles [8].

II. ALGORITHM

Based on SBR, the time-varying scattered field of a target containing moving parts takes on the form

$$E^s(t) = \sum_{i\ \text{rays}} \gamma_i(t)e^{-j\varphi_i(t)} \tag{1}$$

where γ_i is magnitude contribution of each ray to the total scattered field. $\varphi_i = (2\pi f_0/c)\,d_i$ is the phase of each ray, where f_0 is the radar frequency, c is the speed of light and d_i is the distance traveled by the ray. We will assume that the target is stationary except for the moving parts. As time evolves the moving parts undergo motion and those rays which interact with the moving parts will have a different γ_i and φ_i at each time instance.

We shall now attempt to extrapolate the scattered field to a new time t from information at t_0 by making several approximations. We first assume that the ray hit points on the target remain the same at the new time instance. In addition, we assume

$$\gamma_i(t) \cong \gamma_i(t_0) \tag{2a}$$

$$\varphi_i(t) \cong \varphi_i(t_0) + \left.\frac{d\varphi_i}{dt}\right|_{t_0}(t - t_0). \tag{2b}$$

Clearly, these approximations hold only if the moving parts have not undergone large displacements from t_0 to t. When these approximations are valid, however, we see that we can easily compute $E^s(t)$ from the available ray information $\{\gamma_i(t_0), \varphi_i(t_0)\}$, plus the quantity $(d\varphi_i/dt)|_{t_0}$ for each ray.

To compute $(d\varphi_i/dt)|_{t_0}$ for each ray, it is more convenient to define

$$f_{Di} = \frac{1}{2\pi}\left.\frac{d\varphi_i}{dt}\right|_{t_0} \tag{3}$$

which can be interpreted as the "instantaneous" Doppler frequency of ray i. As shown in Fig. 1, at each bounce on the target, a ray undergoes a positive or negative Doppler shift depending on the velocity of the target at the hit point $\vec{v}_n$ and the directions of the incident and reflected rays $\hat{k}_{inc}$ and $\hat{k}_{ref}$. If we assume the incident ray is at a frequency $f_i^{(n-1)}$, the frequency of the reflected ray after the impact is given by

$$f_i^{(n)} = f_i^{(n-1)}\left(1 - \frac{\hat{k}_{inc} \cdot \vec{v}_n}{c}\right)\left(1 + \frac{\hat{k}_{ref} \cdot \vec{v}_n}{c}\right),$$

$$n = 1, 2, \cdots, N. \tag{4a}$$

After N bounces, the total Doppler frequency shift experienced by the ray is then

$$f_{Di} = f^{(N)} - f^{(0)} \tag{4b}$$

where $f_i^{(0)} = f_0$ is the original radar frequency. Therefore, once we have computed the instantaneous Doppler experienced by each ray via (4), we have the necessary information to carry out the scattered field extrapolation to other time instances.

We should point out that the ray summation process of (1) can be accelerated via a fast Fourier transform (FFT)-based fast algorithm. The details of the algorithm has already been reported in [7] and will not be repeated here. The result of applying the fast algorithm is that the ray summation takes essentially negligible time relative to the ray-tracing time. Therefore, the total computational time speedup of using a single ray trace and extrapolating the data to M nearby time instances versus generating the time snapshots via brute force is the factor M.

III. NUMERICAL RESULTS

The Doppler spectrum of a model helicopter with a rotor having four blades is generated using the extrapolation scheme and compared against the brute-force approach. The target is a model helicopter. The blade length of the rotor is 10 ft. One commonly used display of the time-varying Doppler information is the joint time-frequency spectrogram. It is generated by applying a short-time Fourier transform to the time-varying scattered field data. Fig. 2(a) shows the joint time-frequency plot of the helicopter Doppler spectrum using the standard brute-force approach. For this example, it is assumed that the fuselage is stationary and only the blades are rotating at 350 rpm. The incident angle on the target is 10° from nose-on and the radar frequency is 2 GHz. The 1400 time samples of the scattered field are computed over one complete revolution of the rotor blade (360° or 0.171 s). A 35-point running window in time is then used to generate the joint time-frequency plot. The total computation time to generate the data is 1400 × 2 min/run = 2800 min on an SGI Indigo2 workstation (R4400/200MHz CPU). Fig. 2(b) shows the joint time-frequency plot generated using the extrapolation scheme. Ray tracing is carried out at every 9° of rotor revolution and the rest of the data are extrapolated from the ray information at these positions. Therefore, to generate the complete joint time-frequency plot, ray tracing is carried out 40 times. The total computation time for the fast scheme is 40 × 2 min/run = 80 min. This speedup is essentially equal to the theoretical estimate of 35(= 1400/40) since the extrapolation overhead is negligible. The joint time-frequency plot generated using the extrapolation algorithm compares well with that from the brute-force approach. The joint time-frequency plots show four fairly distinct patterns corresponding to the Doppler features from the four blades. The blade flashes at the cardinal angles can be seen for each blade. As the blade rotates, the tip maps out a sinusoidal pattern in time (or angle). The body
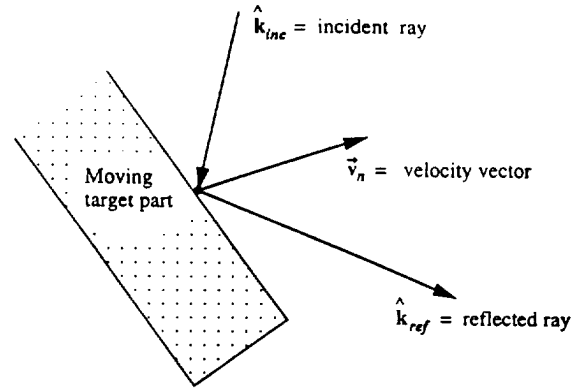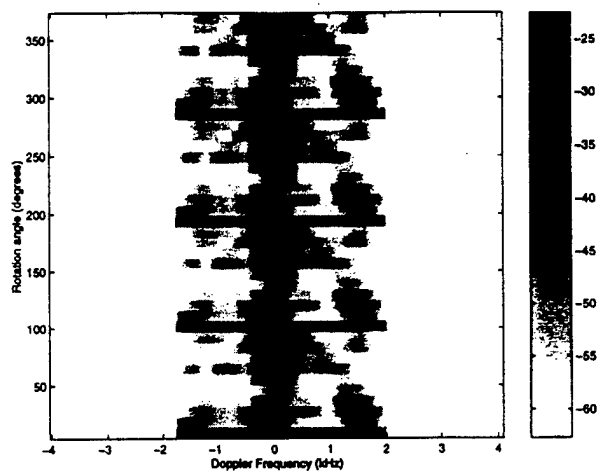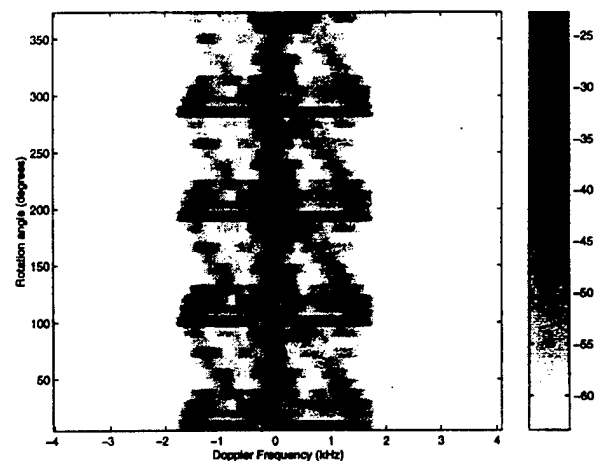

Fig. 1. Each time a ray hits a moving part, it undergoes a Doppler frequency shift depending on the velocity of the part, $\vec{v}_n$ and the directions of the incident and reflected rays $\hat{k}_{int}$ and $\hat{k}_{ref}$.

Figure labels: $\hat{k}_{inc}$ = incident ray; Moving target part; $\vec{v}_n$ = velocity vector; $\hat{k}_{ref}$ = reflected ray

[6] H. Ling, R. Chou, and S. W. Lee, "Shooting and bouncing rays: Calculating the RCS of an arbitrarily shaped cavity," *IEEE Trans. Antennas Propagat.*, vol. 37, pp. 194–205, Feb. 1989.

[7] R. Bhalla and H. Ling, "A fast algorithm for signature prediction and image formation using the shooting and bouncing ray technique," *IEEE Trans. Antennas Propagat.*, vol. 43, pp. 727–731, July 1995.

[8] R. Bhalla, H. Ling, and H. Nussbaum, "Multiaspect range profile extrapolation for the shooting and bouncing ray technique," *J. Electromagn. Waves Applicat.*, vol. 10, pp. 249–268, Feb. 1996.

(a)

(b)

Fig. 2. Comparison of the joint time–frequency plots generated using the standard brute-force approach and the fast extrapolation algorithm. (a) Brute-force approach. (b) Fast extrapolation scheme.

of the helicopter corresponds to the zero Doppler bin since it is assumed to be stationary. There is some spreading of scattered energy about the zero Doppler bin due to body-rotor interactions. Finally, we should point out that the 9° extrapolation window used in the present example is chosen by experience and will in general be governed by target complexity.

REFERENCES

[1] F. E. Nathanson, *Radar Design Principles.* New York: McGraw-Hill, 1969, pp. 173–183.

[2] R. Hynes and R. E. Gardner, "Doppler spectra of S-band and X-band signals," *IEEE Trans. Aerosp. Elect. Syst.*, vol. AES-3, pp. 356–365, Nov. 1967.

[3] M. Bell and R. A. Grubbs, "JEM modeling and measurement for radar target identification," *IEEE Trans. Aerosp. Elect. Syst.*, vol. 29, pp. 73–87, Jan. 1993.

[4] R. Bhalla, H. Ling, S. W. Lee, and D. J. Andersh, "Dynamic simulation of Doppler spectra of targets using the shooting and bouncing ray technique," *Microwave Opt. Tech. Lett.*, vol. 7, no. 18, pp. 840–842, Dec. 1994.

[5] D. C. Ross, J. L. Volakis, and H. T. Anatsassiu, "Hybrid finite element—Modal analysis of jet engine inlet scattering," *IEEE Trans. Antennas Propagat.*, vol. 43, pp. 277–285, Mar. 1995.

Joint Time-Frequency Analysis for

RADAR SIGNAL
and IMAGE
PROCESSING

Applying
JTF analysis
to radar
backscattering,
feature
extraction, and
imaging of
moving targets.

Joint time-frequency (JTF) analysis, introduced in [1], has been applied successfully to many areas of signal processing. Here, we take a deeper look into how JTF analysis can be applied to radar signal and image processing.

A radar transmits electromagnetic waves to a target and receives reflected signals from the target as well as from clutter (Fig. 1). Any unwanted radar return that can interfere with the detection of the desired target is referred to as clutter. It is useful to distinguish this from noise, which also interferes with the detection of wanted signals [2]-[6].

Suppose a radar transmits a signal $s_T(t) = \exp\{j2\pi ft\}$, and the received signal $s_R(t)$ reflected from a point target is proportional to the round-trip delayed transmitted signal $s_T(t-\tau)$ and the reflectivity function ρ of the point target,
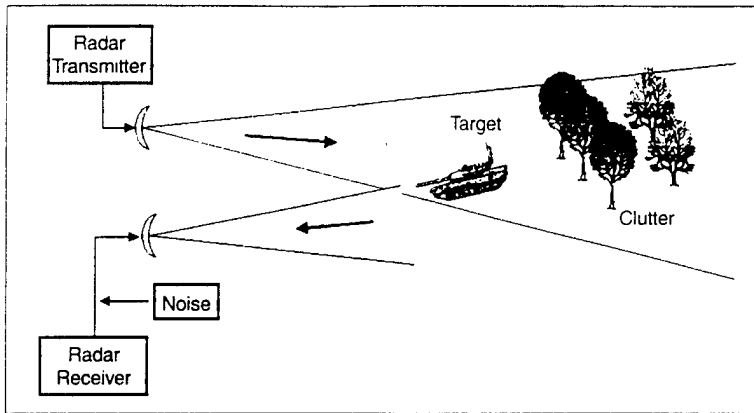
$$s_R(t) \mu \rho s_T(t-\tau) = \rho \exp\{j2\pi f(t-\tau)\}. \quad (1)$$
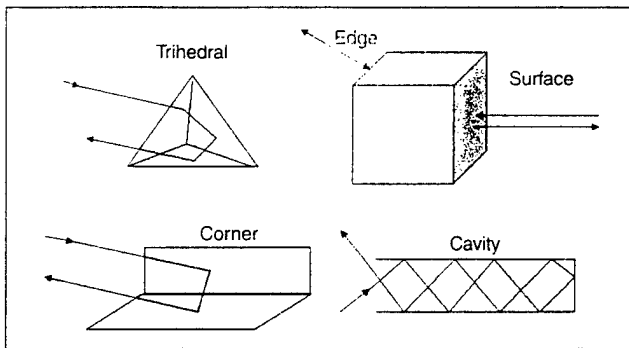
The round-trip travel time is determined by

$$\tau = \frac{2R}{c} \quad (2)$$
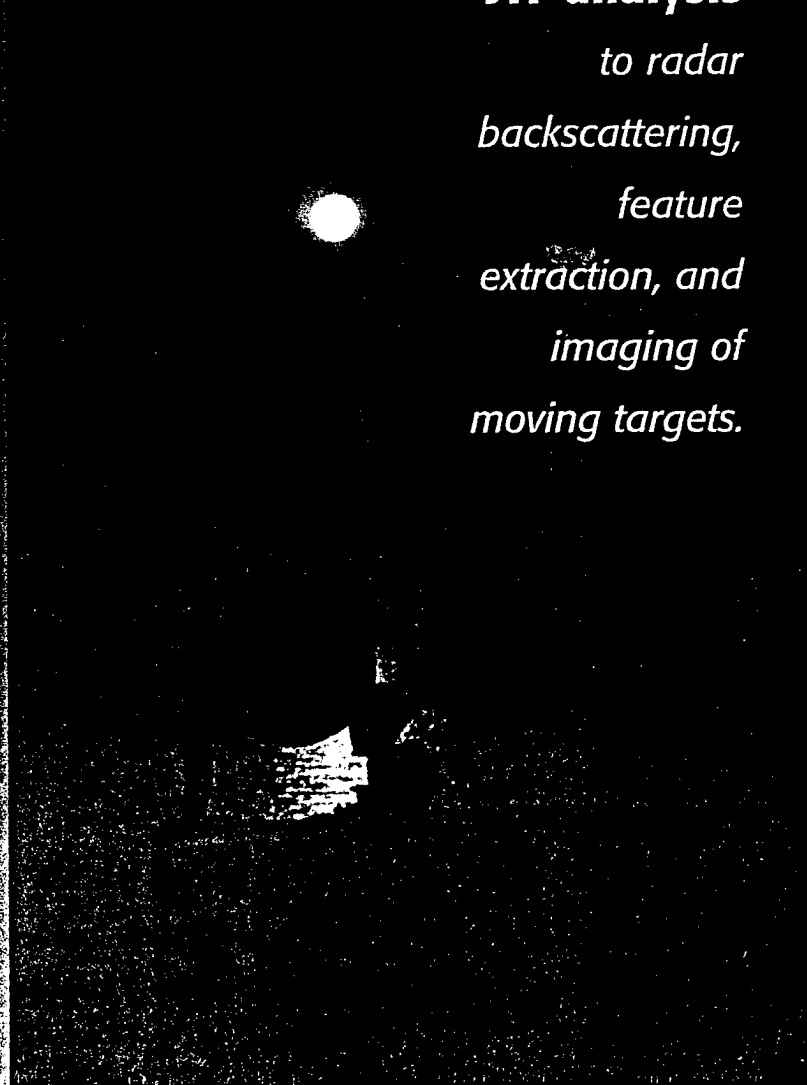
©Lockhead Martin Corporation/Smart Radar

▲ 1. Example of radar operational scenario: transmitter, receiver, target, noise, and clutter.

▲ 2. Examples of manmade targets: surface, edge, corner, trihedral, and cavity.

where R is the range from the radar to the point target and c is the wave propagation velocity.

When the target moves with a velocity v relative to the radar, called the radial velocity, the radar signal must travel an extra longer or shorter distance to reach the target. Therefore, the signal received at time t is reflected from the target at time $(t-\tau(t)/2)$, and the received signal becomes $s_R(t)\mu\rho s_T[t-\tau(t)]$, where the round-trip travel time is a time-varying delay [2],[7].

In addition to the signal reflected by the target, there is also additive noise. The signal-to-noise ratio (SNR) at the radar receiver is determined by the received power reflected from the target, the noise figure, and the bandwidth of the receiver. Improvement in the SNR will increase the probability of target detection and the accuracy of parameter estimation. A radar usually transmits a sequence of pulses or other signal waveforms with a pulse repetition frequency (PRF) usually required by the maximum range of detection. Target information may be examined directly from the radar-range profile, i.e., the distribution of target reflectivity along the radar line of sight to the target, or from its frequency spectrum by applying the Fourier transform [8]-[11].

In general, the radar processes the received signal and extracts information about the target. The range to the target, i.e., the distance from the radar to the target measured along the radar line of sight, is estimated by the time-delay between the transmitted signal and the re-

ceived signal. For a moving target, the measurement of the target's velocity is based on the well-known Doppler effect. If the radar-transmitted signal is at frequency f, the reflected signal from the moving target is subjected to a Doppler frequency shift from its transmitted frequency, $f + f_d$. This frequency shift is induced by relative motion between the radar and the target [2]. In the case where a target has a radial velocity v, the Doppler frequency shift is determined by the radial velocity of the target and the wavelength of the radar transmitted waveform

$$f_d = -2f\frac{v}{c}. \tag{3}$$

Thus, if a target is closing on the radar at a velocity $v = -1000$ (ft/s) $= -304.8$ (m/s), the Doppler frequency shift for X-band radar at 9842 MHz is 20 kHz.

Radar targets, especially man-made targets, usually can be considered as a collection of point scatterers. These scatterers may have a wide variety of reflecting or backscattering behaviors [12], [13]. They can include surfaces, edges, corners, dihedrals, trihedrals, and cavities (Fig. 2). Each type of scatterer has a different backscattering behavior, which can provide a way to recognize the target. For example, when cavities or duct-type structures are present in targets, multiple bounces appear in the radar image as "clouds" extended in the range domain [43]. However, the same mechanism may provide important features that, if properly interpreted, can be important factors in the target recognition process. In the next section, we will further describe radar backscattering and introduce time-frequency analysis applications to radar backscattering and feature extraction.

Range profiles have been examined for target recognition, especially in cases when a radar image cannot be generated due to various reasons, such as short radar dwell time on the target [9]. With high range resolution, the range profile can provide target information about target length and positions of stronger scatterers, such as a radar dish, engine intakes, and other strong scattering centers (Fig. 3). The dimension transverse to the radar line of sight is called the cross range. Because the Doppler shift of a scatterer in a target is proportional to the cross
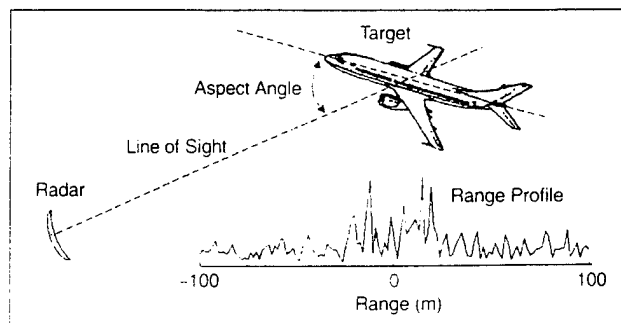

▲ 3. Example of an aircraft's range profile.

range of the scatterer by a scale factor, the projection of the target reflectivity distribution on the cross-range dimension can be obtained from the distribution of Doppler shifts, called the Doppler profile. With high-resolution Doppler profiles, the locations of stronger scatterers and the target's extents in the Doppler dimension can be obtained as illustrated in Fig. 4. By combining range profiles and Doppler profiles, a 2-D radar image may be generated [13]-[16]. The radar image is a spatial distribution of the target's reflectivity mapped onto a range and Doppler plane. The range-Doppler image can be converted to this 2-D image if we have accurate knowledge of the scale factor. This is determined by the rotation rate, the distance of the scatterer from its rotation center, and the wavelength of the transmitted signal [15], [16].

An important factor of the image quality is its resolution. Resolution is the ability to separate closely spaced scatterers in range and in cross range. The minimum distance in the range Δ_r combined with in the cross range or azimuth Δ_{cr} by which two point-scatterers may be separated is the resolution of the image. A rectangle with sides Δ_r and Δ_{cr} is called a resolution cell. Range resolution is determined by the frequency bandwidth passed by the transmitter and receiver. For example, a 500-MHz bandwidth can yield a range resolution of 1 ft. The width of the bandwidth obtained depends on the radar operating frequency. For an X-band radar operated at a 10,000-MHz frequency, a bandwidth of 5% of the radar operation frequency, i.e., 500 MHz, is possible. Generally, higher resolution is more easily achieved in the range domain than in the cross-range domain. To obtain high cross-range resolution without utilizing an impractically large antenna aperture, synthetic aperture processing is widely used. It coherently combines signals obtained from sequences of small apertures at different aspect angles of the target to emulate a result which could be obtained from a large antenna aperture [14], [15].

Coherent processing maintains the relative phases of successive pulses. Thus, the phase from pulse to pulse is preserved and a phase correction can be applied to the re-
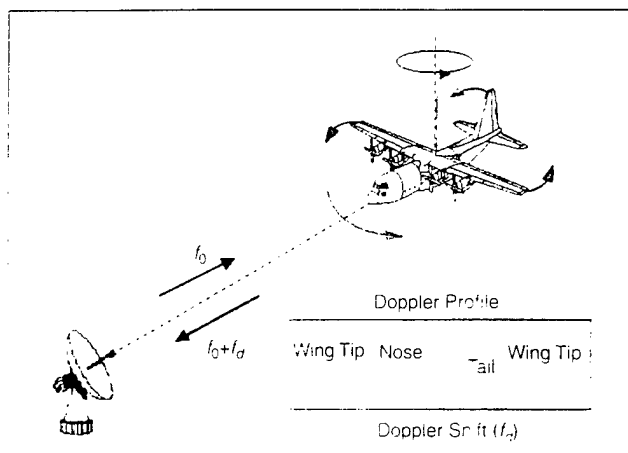
▲ 4. An illustration of the Doppler profile of an aircraft.

To use the Fourier transform properly, it is assumed that the frequency contents of the analyzed signal must be time-invariant.

turns to make them coherent for successive interpulse periods. If radar returns are processed coherently, the processed data retains both the amplitude and the phase information about the target. The amplitude is related to the radar cross section of the target (a measure of the ability to reflect electromagnetic waves) and the phase is related to the radial velocity of the target. The time history series of samples taken at each range forms the basis for radar signal and image processing.

Imaging of moving targets using radar has been a major challenge. Techniques for high-resolution radar imaging are based on synthetic aperture formation. When there is a relative motion between the radar and the target, a synthetic aperture can be formed. Traditionally, synthetic aperture radar (SAR) refers to the situation where the radar is moving [14]-[16], while inverse synthetic aperture radar (ISAR) refers to the situation where the target is moving [13], [15].

To form an image from the radar data, accurate motion compensation is needed. For ISAR, if the translational motion is compensated for by using a reference point on the target such as the center of rotation, then the moving target becomes a rotating target around that center, and forms an equivalently larger circular aperture focused at the center. The target can be considered to be a set of individual point scatterers, each with a radial velocity or Doppler frequency shift to the radar. Thus, the distribution of the radar reflectivity of the target can be measured by the Doppler frequency spectrum at each range estimated by taking the Fourier transform over the observation time interval.

To use the Fourier transform properly, it is assumed that the frequency contents of the analyzed signal must be time-invariant. With this assumption, a long observation time results in high Doppler resolution. However, when the target moves, Doppler frequency shifts are time-varying, and the assumption of time-invariant Doppler frequency shifts is no longer valid. Thus, the Doppler spectrum becomes smeared, degrading the cross-range resolution, and the radar image becomes blurred. There are many methods, some called autofocusing and others called motion-compensation, used in solving the Doppler smearing and image blurring problem [17]-[26]. Most methods are Fourier-based approaches that attempt to flatten Doppler spectra of individual scatterers by using sophisticated preprocessing
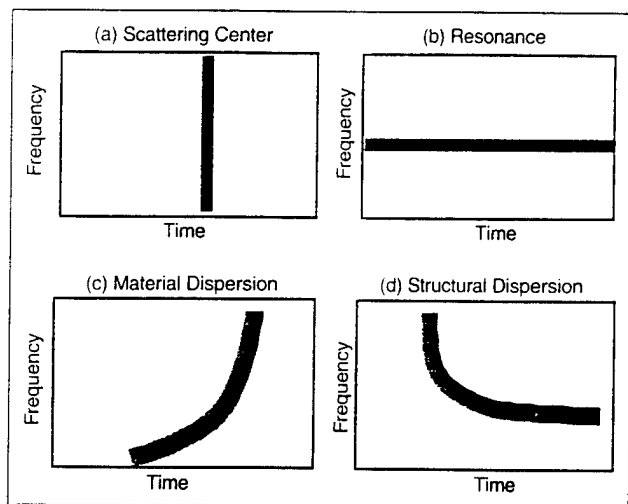
▲ 5. Electromagnetic mechanisms are manifested in the joint time-frequency image as distinct features. (a) Scattering center, (b) resonance, (c) material dispersion, and (d) structural disper-
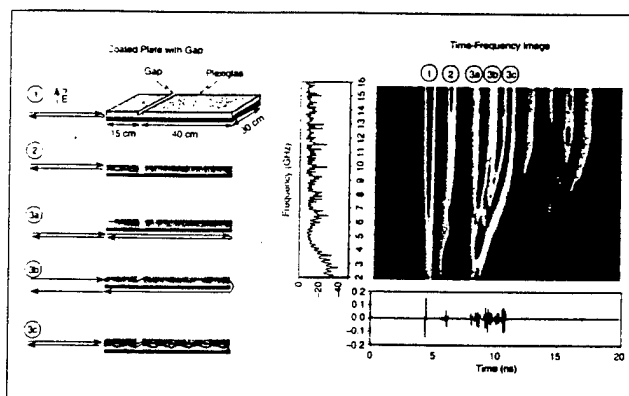

▲ 6. Joint time-frequency (JTF) image of the backscattering data from a coated plate with a gap in the coating. The JTF image is generated by the short-time Fourier transform. Those features which show slanting in the JTF plane are associated with the dispersive surface wave mechanisms in the coating.

approaches. Others use modern spectral analysis to achieve sharper images with shorter data samples [27]-[30]. Sets of radar data are available from http://airborne.nrl.navy.mil/~vchen/tftsa.html. In another section, we introduce an image formation based on time-frequency analysis, which can resolve the image-blurring problem without resorting to sophisticated preprocessing algorithms.

Applications of JTF Analysis to Radar Backscattering

Time-Frequency Analysis of Radar Range Profiles

With the radar operating at a sufficiently high bandwidth (i.e., equivalent to a short pulse), the resulting high-resolution range profile can be interpreted as a mapping of the reflectivity of the target along the radar line of sight. With simple targets, a range profile typically consists of a series of distinct peaks that can be related spatially to the scattering centers on the target. These features are often examined for signature diagnostic and target recognition applications. For real targets, however, the scattering characteristics are usually more complex. For example, the scattering from some components on a target can be strongly dispersive as a function of frequency, and may give rise to extended returns in the range domain. These dispersive scattering phenomena can be difficult to interpret from the time-domain range profile.

JTF methods described in [1] have been used to analyze electromagnetic backscattered data with good success [31]-[42]. The JTF representation of a signal is a 2-D-feature space that facilitates the visualization and interpretation of complex electromagnetic wave phenomenology. In this feature space, discrete time events such as scattering centers, discrete frequency events such as resonances, and dispersive mechanisms due to surface waves and guided modes can all be displayed simultaneously. This can lead to more insight into the complex electro-

magnetic wave propagation and scattering mechanisms than the information available from either time or frequency domain representations alone.

Shown in Fig. 5 are the time-frequency features of some commonly encountered scattering mechanisms. A discrete event in time, for example, could be due to wave scattering from a spatially localized scattering center on a structure. It shows up as a vertical line [Fig. 5(a)] in the image because it occurs at a particular instance, but over all frequencies. A target resonance, e.g., the return from a partially open cavity, is a scattering event that becomes prominent at a particular frequency. It shows up as a horizontal line in the JTF plane [Fig. 5(b)]. Dispersive phenomena, on the other hand, are characterized by slanted curves in the time-frequency image. For instance, surface wave mechanisms due to material coatings are characterized by curves with a positive slope [Fig. 5(c)]. Another type of dispersion arises from waveguide structures. These "structural dispersion" mechanisms are characterized by curves with a negative slope in the time-frequency image [Fig. 5(d)]. All of the above phenomena have been observed in a wide variety of structures, from simulation data on canonical structures to measurement data on complex platforms [31]-[42]. Below, two examples are presented to demonstrate the unique features of electromagnetic scattering mechanisms in the JTF plane.

In the first example, the backscattered data from a dielectric-coated plate with a gap in the coating is considered [35] (Fig. 6). The radar signal is incident edge-on from the left, with the incident electric field polarized in the vertical direction. The radar frequency response has been generated by computer simulation and verified by laboratory measurement. The simulation result is shown along the vertical frequency axis. The time-domain response, or equivalently, the range profile (where range = $c\tau/2$), is obtained by Fourier transforming the 1.7-to-18-GHz data. The resulting range profile is shown along the horizontal time axis. It appears that three distinct pulses are present. However, the second and third pulses are spread out in range.

In order to resolve in finer detail the dispersive scattering mechanisms in this coated plate, the spectrogram of the backscattered signal is generated using the short-time Fourier transform. As can be seen, the scattering mechanisms are much more apparent in the 2-D JTF plane than in either the time or the frequency domain. In particular, it is observed that the third broad pulse in the time domain actually consists of three separate scattering mechanisms (labeled as 3a, 3b, and 3c). As the frequency approaches zero, the propagation delays of mechanisms 3a, 3b, and 3c approach the same value. As the frequency increases, the pulses have different propagation delays, and become clearly separated.

Slanted curves in the time-frequency plane (like mechanisms 2, 3b, and 3c) are characteristic of dispersive behavior. In the case of the coated plate, surface waves excited in the coating give rise to the dispersive mechanisms. At frequencies well above cutoff, the surface wave is tightly bound to the dielectric and the wave velocity approaches the slow dielectric velocity. Near cutoff, the surface wave velocity approaches that of free space and exhibits a shorter propagation delay. Therefore, in the time-frequency plane, the surface wave phenomena show up as slanted curves with a positive slope.

Based on the propagation delay considerations and the above observation, it is possible to pinpoint the five dominant scattering mechanisms. They are shown on the left in Fig. 6, which clearly indicates that mechanisms 2, 3b, and 3c include surface wave propagation. For the polarization under consideration and the frequency range of the data, the TM_0 surface wave mode that has zero cutoff is the only

mode that can propagate in the dielectric (the TM_1 mode has a cutoff frequency of 23.4 GHz). Finally, higher-order scattering mechanisms can be observed during the late-time portion of the data, but they are very weak.

A discrete event in time, for example, could be due to wave scattering from a spatially localized scattering center on a structure.

In the second example, the scattering from a slotted waveguide structure is considered [39]. The geometry is shown in Fig. 8, where a long rectangular waveguide is flush mounted in a conducting ground plane. Two narrow slots are opened on each end of the ground plane. The structure is excited by a horizontally polarized radar signal occurring at an angle of 30° with respect to the vertical. The backscattered data are generated by a computational electromagnetic simulator based on the method of moments. The data are generated from 0.025 to 10 GHz in 25-MHz increments.

The time-frequency representation of the data, obtained using the short-time Fourier transform, is shown on the right in Fig. 7. The two early-time vertical lines correspond with the exterior scattering centers from the slots. The other curves are related to signals coupled into
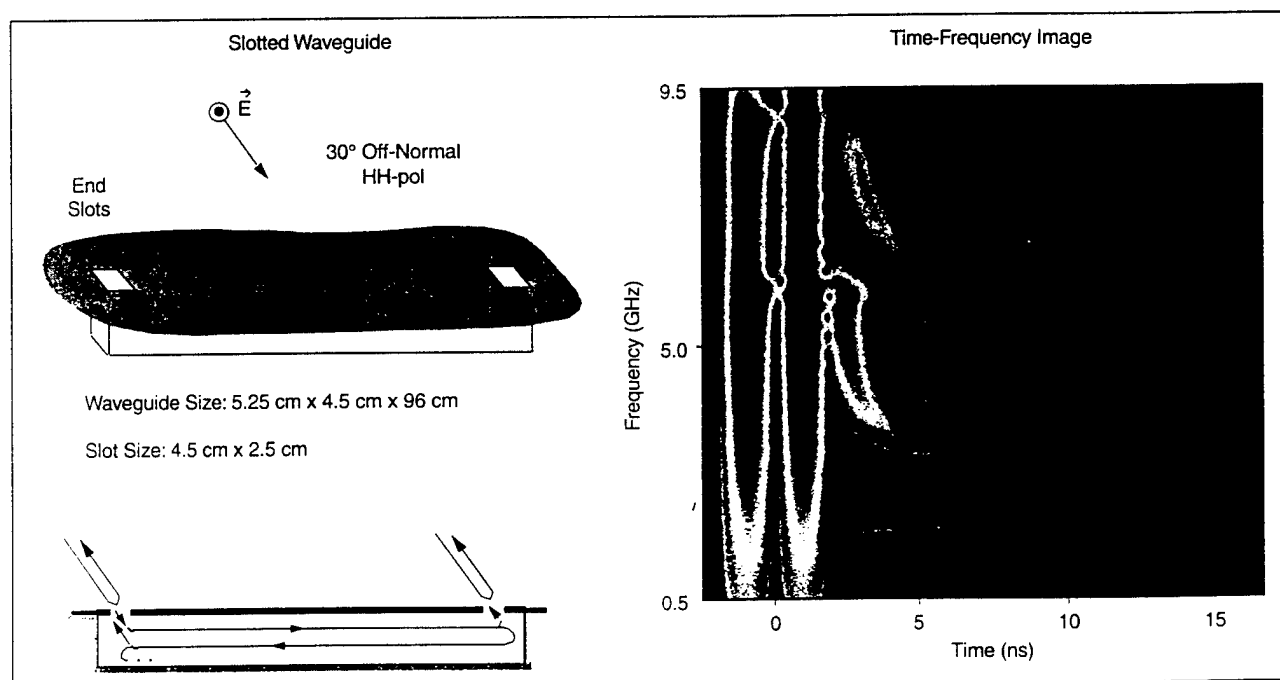
▲ 7. Joint time-frequency image of the backscattering data from a slotted waveguide structure. The data were simulated using a method of moments solver. The JTF image is generated by the short-time Fourier transform. The JTF image shows both the early-time discrete-time returns from the slot exterior and the late-time dispersive mechanisms due to modal propagation inside the waveguide.
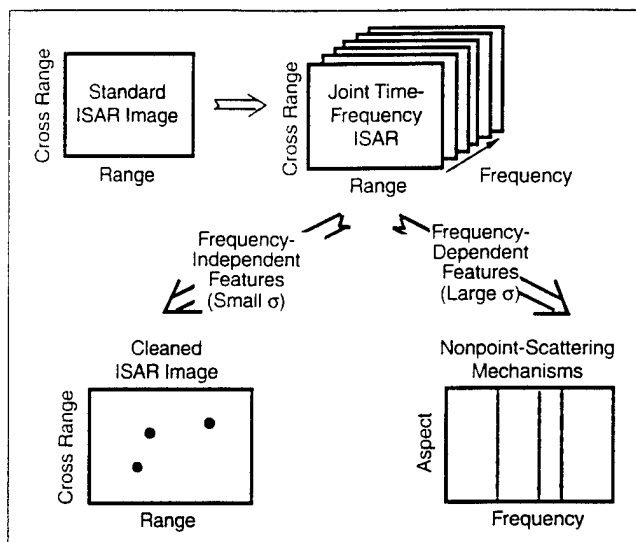
▲ 8. Joint time-frequency processing is applied to the range dimension of the conventional range/cross-range ISAR image to gain an additional frequency dimension. By examining how the resulting images vary as a function of frequency, the frequency-independent features can be separated from the frequency dependent ones and displayed in an appropriate feature space.

the waveguide (Fig. 7, again). When the wave reaches the first slot, some energy is coupled into the waveguide, propagating to the other end as a sum of waveguide modes. The energy carried by these modes begins to reradiate through the other slot after a time given by L/c where L is the length between the two slots. However, this is the time delay only for frequencies well above the modal cutoff for which the modal group velocity approaches c. For frequencies approaching the cutoff frequency of the respective mode, the group velocity tends toward zero and the time delay goes to infinity. Consequently, each modal dispersion behavior is manifested as a time-frequency trajectory with negative slope [as illustrated earlier in Fig. 5(d)]. This behavior can be clearly identified in the spectrogram, where the presence of two modal dispersion curves with cutoffs at 3 and 6 GHz are observed. They correspond to the TE_{10} and TE_{20} modes in the waveguide. Note that the amplitude variation of the signal along these curves is governed by the coupling mechanisms through the slot apertures and is considerably more complex.

Because multiple reflections occur, we also see other dispersion curves with greater delays during the late-time portions of the return. The first one corresponds with the energy that, upon reaching the other end, reflects back and radiates through the slot on the left. The next is the three-bounce mechanism. Note that energy is also coupled into the waveguide through the slot on the right, and through similar mechanisms, generates dispersion curves in the time-frequency plot depending on the number of bounces.

From the above two examples, it can be seen that the JTF representation can aid in the interpretation of com-

plex electromagnetic phenomena. Furthermore, the JTF features can be well understood in terms of the target-scattering physics. For radar applications, the time-frequency representation is particularly effective in identifying scattering mechanisms in targets containing "sub-skinline" structures such as inlet ducts, antenna windows, and material coatings.

Physics-Based Feature Extraction from Radar Imagery

The JTF processing of the one-dimensional range profile described above can be further extended to deal with 2-D radar imaging. ISAR imaging, as discussed earlier, is a robust process for mapping the position and magnitude of the point scatterers on a target from multi-frequency and multi-aspect backscattered data. However, for complex targets containing other scattering phenomena such as resonances and dispersive mechanisms, image artifacts are often encountered in the resulting ISAR image. One important example is the scattering from the engine inlet/exhaust duct on aircraft. It is a dominant contributor to the overall scattering from the target, yet its waveguide-like structure and the associated frequency-dependent scattering mechanisms make it a nonpoint-scattering feature.

When processed and displayed by the conventional ISAR algorithm, the inlet return results in an image feature which is not well-focused, is not related to the spatial location of the scatterer, and can often obscure other important point features on the target. Therefore, it would be useful to automatically remove these artifacts from the ISAR image, leading to a clean ISAR image containing only physically meaningful point scatterers. Furthermore, the inlet features extracted can be better displayed in a more meaningful feature space to identify target resonances and cutoff phenomena.

JTF processing can be applied to ISAR image processing to accomplish the above objective [43]. The conceptual idea behind the JTF ISAR algorithm is to apply JTF processing to the range (or time) axis of the conventional range/cross range ISAR image to gain an additional frequency dimension. The result is a 3D range/cross-range/frequency matrix, with each range/cross-range slice of this matrix representing an ISAR image at a particular frequency (Fig. 8). Consequently, by examining how the ISAR image varies with frequency, we can distinguish the frequency-independent scattering mechanisms from the frequency-dependent ones. In the actual implementation of the JTF ISAR, the choice of the JTF processing engine is critical to preserving range resolution. This is demonstrated below using the adaptive Gaussian representation proposed by Qian and Chen [44].

The signal-adaptive Gaussian representation is a high-resolution time-frequency representation. (A similar algorithm called matching pursuit was developed independently at around the same time by Mallat and

Zhang [45]). The objective of this method is to expand a signal $f(t)$ in terms of Gaussian-modulated exponential basis functions $h_p(t)$ with an adjustable standard deviation σ_p and a time-frequency center (t_p, f_p):

$$f(t) = \sum_{p=1}^{\infty} B_p h_p(t)$$

(4)

where

$$h_p(t) = (\pi \sigma_p^2)^{-0.25} \exp\left[-\frac{(t-t_p)^2}{2\sigma_p^2}\right] \exp(j2\pi f_p t).$$

(5)

Note that the basis function has a dual form in its Fourier transform representation:

$$H_p(f) =$$

$$\left\{\pi\left[\frac{1}{(2\pi\sigma_p)}\right]\right\}^{-0.25} \exp\left\{\frac{(f-f_p)^2}{2\left[\frac{1}{(2\pi\sigma_p)}\right]}\right\} \exp[-j2\pi(f-f_p)t_p]$$

(6)

Therefore, these basis functions have a time-frequency extent given by σ_p and $(1/2\sigma_p)$, respectively. The coefficients B_p are found one at a time by an iterative procedure. One begins at the stage $p = 1$ and chooses the parameters σ_p, t_p and f_p, such that $h_p(t)$ is most "similar" to $f(t)$, that is:

$$|B_p|^2 = \max_{\sigma_p, t_p, f_p} \left| \int f_{p-1}(t) h_p^*(t) dt \right|^2$$

(7)

where $f_0(t) = f(t)$. For $p > 1$, $f_p(t)$ is the remainder after the orthogonal projection of $f_{p-1}(t)$ onto $h_p(t)$ has been removed from the signal:
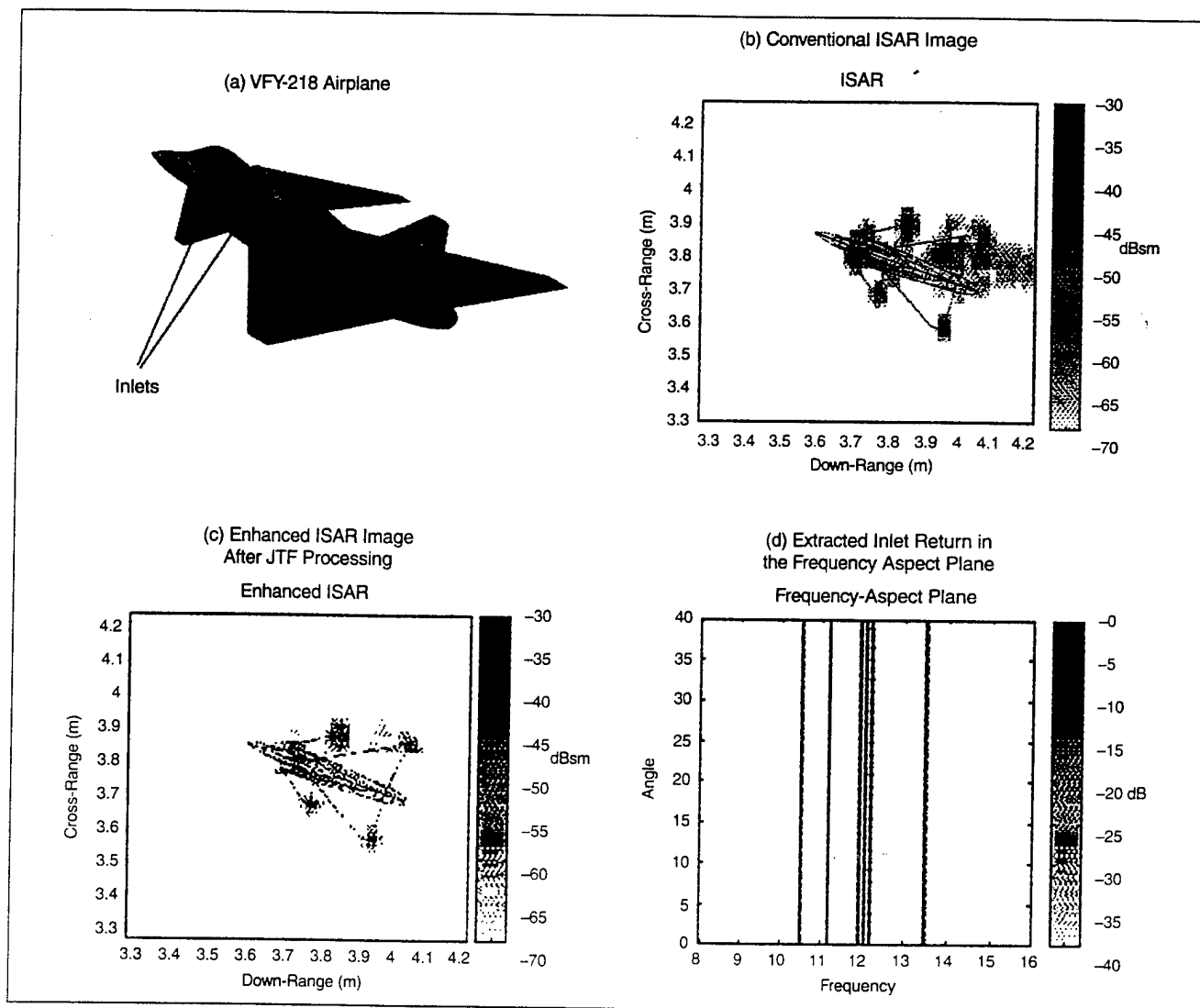
▲ 9. Adaptive JTF ISAR processing using the test range data from a 1:30 scaled model of the VFY-218 airplane. (a) Geometry of the VFY-218 with two deep inlet ducts. (b) Conventional ISAR image for frequency from 8 to 16 GHz, aspect from 0° to 40°. The dispersive cloud over the right wing is due to the return from the left inlet duct. (c) Enhanced ISAR image obtained by removing non-point scattering mechanisms using the AJTFISAR algorithm. The inlet return has been removed from the image. (d) Frequency-aspect display showing the extracted features from the engine return. Prominent resonant frequencies are observed in this feature space.

By replacing the Fourier transform with a high-resolution time-frequency transform, the image blurring caused by the time-varying Doppler frequency shifts can be mitigated without applying sophisticated focusing algorithms.

$$f_p(t) = f_{p-1}(t) - B_p(t)h_p(t). \tag{8}$$

This procedure is repeated to generate as many coefficients as needed to accurately represent the original signal.

The adaptive Gaussian representation has two distinct advantages over conventional time-frequency techniques such as the short-time Fourier transform. First, it is a parametric procedure that results in very high time-frequency resolution. More importantly for our application, the adaptive spectrogram allows us to distinguish the frequency-dependent events from the frequency-independent ones automatically through the extent of the basis functions. From (5), it can be seen that scattering centers, i.e., signals with very narrow lengths in time, will be well represented by basis functions with very small σ_p. Frequency resonances, on the other hand, will be better depicted by large σ_p. Therefore, if we reconstruct the ISAR image using only those Gaussian bases with small variances, a much cleaner image can be obtained showing only the scattering centers. The remaining mechanisms, i.e., those related to the large variance Gaussians, are more meaningful when viewed in a dual frequency-aspect display, where resonances and other frequency-dependent mechanisms can be better identified.

The algorithm is demonstrated by using the chamber measurement data of a 1:30 scale model Lockheed VFY-218 airplane provided by the Electromagnetic Code Consortium [46]. The airplane has two long engine inlet ducts, which are rectangular at the open ends, but merge together into one circular section before reaching a single-compressor face [Fig. 9(a)]. As we can clearly see in the conventional ISAR image for the horizontal polarization at 20° near nose-on, the large cloud outside of the airframe structure is the inlet return [Fig. 9(b)]. Fig. 9(c) shows the enhanced ISAR image of Fig. 9(b), obtained by applying the JTF ISAR algorithm and keeping only the small variance Gaussians. We see that only the scattering center part of the original signal remains in the image as expected. Notice that the strong return due to engine inlet has been removed, but the scattering from the right wing tip remains. Fig. 9(d) shows the frequency-aspect

display of the high variance Gaussians. A number of equispaced vertical lines can be seen between 10.5 and 13.5 GHz. Given the dimensions of the rectangular inlet opening, we estimate that these frequencies correspond approximately to the second cutoff frequency of the waveguide-like inlet. This information may be unique to the particular inlet structure under consideration and may be useful as an additional feature vector in target classification [47]. The processed images for observation angles varying from 0-360° have been made into an MPEG movie that can be downloaded from http://ling0.ece.utexas.edu.

In this section we presented a JTF ISAR algorithm to process data from complex targets containing not only scattering centers, but also other frequency-dependent scattering mechanisms. The adaptive JTF ISAR algorithm allows the enhancement of the ISAR image by eliminating nonpoint-scatterer signals, thus leading to a much cleaner ISAR image. Moreover, the extracted nonpoint-scattering mechanisms can be more appropriately displayed in an alternative feature space to show target resonances and frequency dispersion. This is accomplished without any loss in down-range resolution. In the next section, the JTF processing will be applied to the cross range (or Doppler frequency) instead of the range dimension of the radar image for the purpose of refocusing the image due to complex target motion.

## Applying JTF Analysis to Radar Imaging of Moving Targets

Time-Frequency-Based Radar Image Formation

To achieve high cross-range resolution, SAR uses synthetic array processing that coherently combines signals obtained from sequences of small apertures at different aspect angles, with respect to the target to emulate the result from a large aperture [14], [15]. In radar images, the cross-range resolution is obtained from the Doppler resolution [13], [15]. The differential Doppler shifts of adjacent scatterers of the target can be observed in the radar receiver; therefore, the distribution of the target's reflectivity can be measured by Doppler spectra. The conventional method to retrieve Doppler information is the Fourier transform.

Based on the radar-received signal from a single point scatterer, the received signal from the entire target can be represented as the integration of the returned signals from all scatterers in the target [15]

$$S(f) = \iint \rho(x,y) \exp\left\{-j2\pi f \frac{2r}{c}\right\} dx\, dy \tag{9}$$

where r is the range of a point scatterer in the target. It can be expressed by the range of the target's center of rotation $R(t)$, the rotation angle of the target $\theta(t)$, and the scatterer's location (x,y) in the target inertial coordinate (Fig. 10). Because the range $R(t)$ and the rotation angle $\theta(t)$
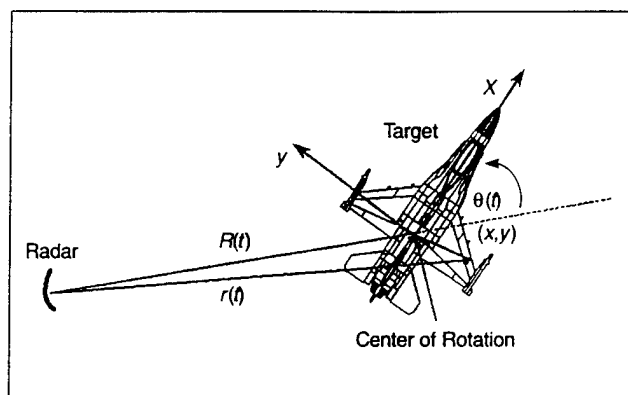
▲ 10. Geometry of radar imaging.

are functions of time, the range of a point scatterer in the target is also a function of time

$$r(t)=R(t)+x\cos\theta(t)-y\sin\theta(t). \qquad (10)$$

Then, the baseband signal in the radar receiver becomes

$$S(f,t)=$$

$$\exp\left\{-j4\pi\frac{R(t)}{c}\right\}\iint\rho(x,y)\exp\{-j2\pi[xf_x(t)-yf_y(t)]\}dxdy \qquad (11)$$

where the frequency components are defined by

$$f_x=\frac{2f}{c}\cos\theta(t) \qquad (12)$$

and

$$f_y=\frac{2f}{c}\sin\theta(t). \qquad (13)$$

From the radar-received signal $S(f,t)$, if the target's range as a function of time t is known exactly over the imaging time duration, then the extraneous phase term $\exp\{-j4fR(t)/c\}$ can be removed by multiplying its conjugate with the received signal, i.e., $G(f_x, f_y) = S(f,t)\exp\{j4fR(t)/c\}$. This is referred to as gross focusing or motion compensation [15], [18]. Then, the target's reflectivity density function can be reconstructed simply by taking the inverse Fourier transform of the motion compensated signal

$$\rho(x,y)=IFT[G(f_x,f_y)]. \qquad (14)$$

In order to apply the Fourier transform properly, scatterers must remain in their range cells during the imaging time, and their Doppler frequency shifts must be constant [17]-[20]. To obtain a focused Fourier radar image, range tracking must be used to pull scatterers back into their range cells and Doppler tracking must be used to correct any time-varying phase change. Thus, a constraint has been imposed on the Doppler frequency spectrum, requiring it to be constant. Then, a clear radar image can be captured (Fig. 11).
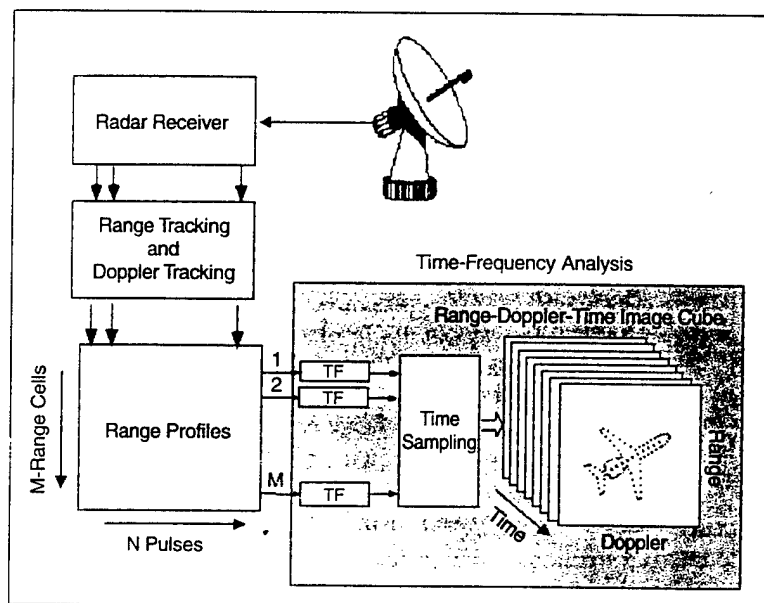
The range tracking and Doppler tracking form the basis of the standard procedure for focusing radar images [13], [15]. If the target is moving smoothly, the standard focusing is good enough to generate a clear image of the target by using the Fourier transform. However, when a target exhibits complex motion, such as rotation and maneuvering, the standard procedure is not sufficient to generate an acceptable image for viewing and analysis. Scatterers can still drift out of their range cells and their Doppler frequency shifts can still be time-varying. Thus, the Doppler spectrum obtained from the Fourier transform will be smeared, and the radar image will be blurred. In this case, more sophisticated procedures for individual scatterers, such as polar reformatting [16], are needed. Thus, each scatterer may remain in its range cell and its Doppler frequency shift may be constant. Then, the Fourier transform can be applied properly to reconstruct a clear image of the target. However, to perform the polar reformatting, the knowledge required of the initial kinematic parameters of the target may not be always available. Some individual scatterers may still drift through their range cells and their Doppler frequency shifts may
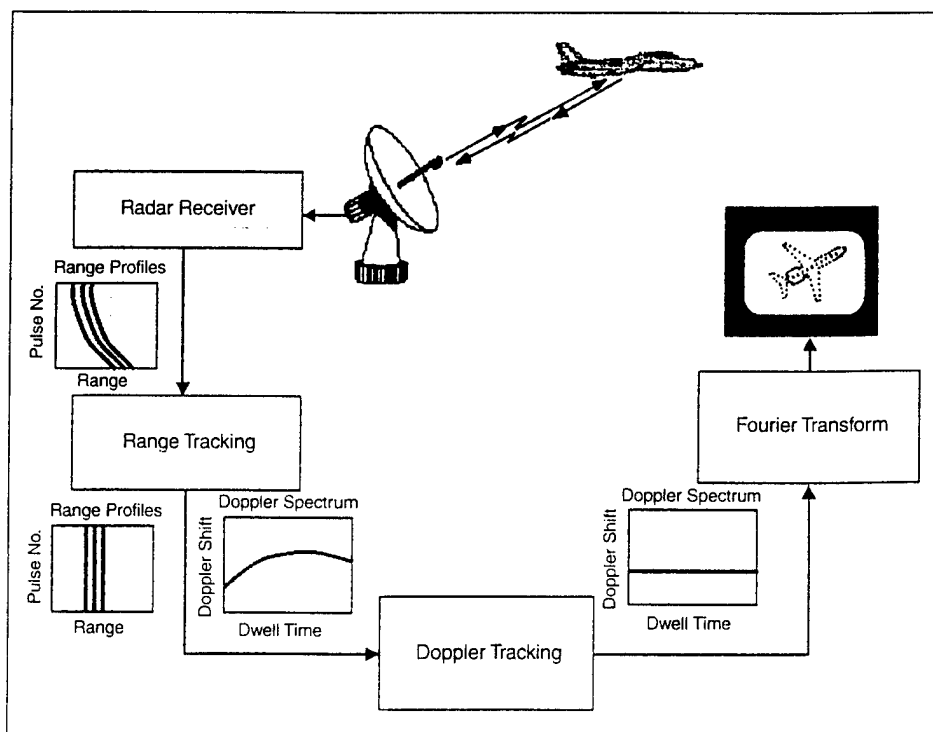
▲ 11. Conventional radar imaging of moving targets with the Fourier transform.
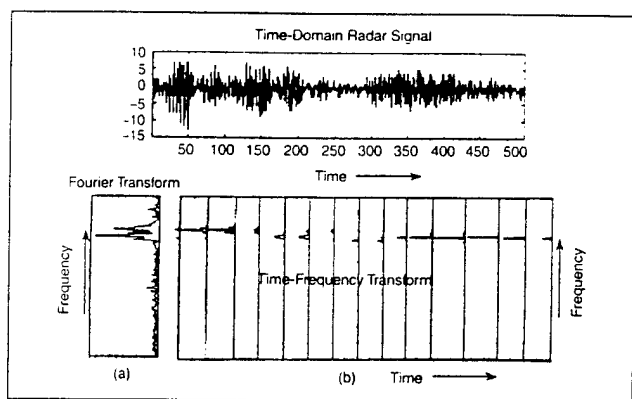
▲ 12. Time-varying spectrum of radar data represented by (a) the Fourier transform and (b) the time-frequency transform.

▲ 13. Time-frequency based radar image formation.
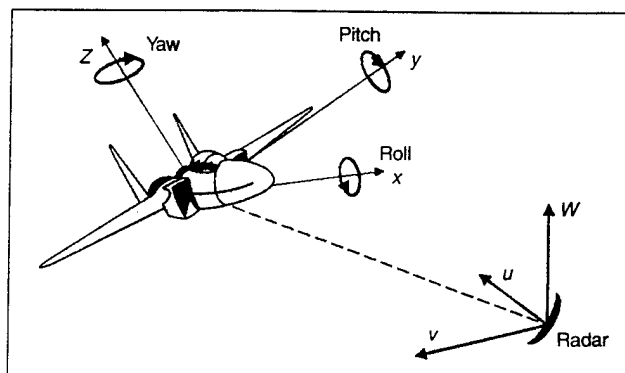
$$f_{d_{trans}} = \frac{2f}{c} v_r \tag{15}$$

and the rotation-induced Doppler shift [51]

$$f_{d_{rot}} = \frac{2f}{c}[x(-\Omega\sin\psi_0 - \Omega^2 t\cos\psi_0) - y(\Omega\cos\psi_0 - \Omega^2 t\sin\psi_0)] \tag{16}$$

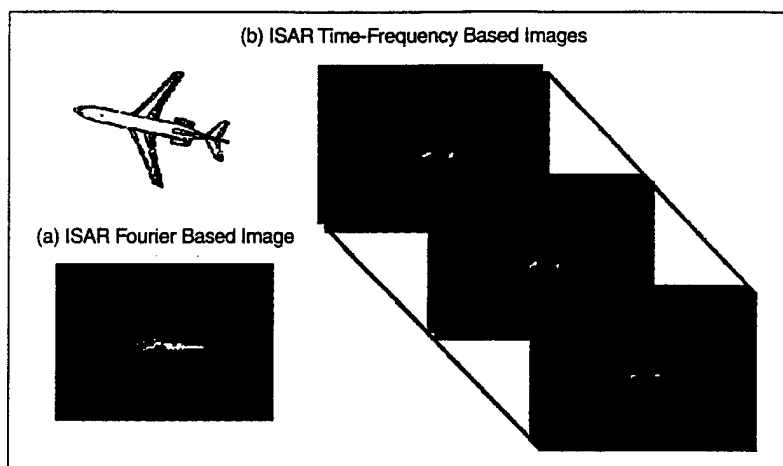where ψ_0 is the initial aspect angle of the target. It is clear that even if the rotation rate Ω and the radial velocity of the target v_r are constant, the rotation-induced Doppler frequency shift $f_{d\,rot}$ is still time-varying. Other sources of time-variation in the Doppler frequency shift may result from uncompensated phase errors due to irregularities in the target's motion, the fluctuation of the target's rotation rate, fluctuation in localizing the rotation center, inaccuracy in tracking the phase history (i.e., a collection of phases of returned signals during imaging time), and other variations of the system and the environment. Because the residual phase errors may vary with time, the Doppler frequency can also vary with time.

The Fourier transform indicates which frequency components are contained in the signal, but it does not tell how frequencies change with time. By representing the time-varying Doppler frequency spectrum with the Fourier transform, the Doppler spectrum becomes smeared as in the example shown in Fig. 12, where the Fourier transform (a) and a time-frequency transform (b) are applied to a radar data. We can see that the Fourier transform of the data is actually the integral of the time-frequency transform of the same data over its duration. This is due to the frequency marginal condition [51].

From the insight into the image blurring, we can see that in order to achieve a clear image, the time-frequency transform should be used in place of the Fourier transform. The time-frequency transform introduced in [1] is an efficient way to resolve the image blurring problem

still be time-varying. Hence the resulting image can still be blurred when the Fourier transform is applied.

However, the restrictions of the Fourier transform can be circumvented if the time-frequency transform described in [1] is used to replace the Fourier transform [48]-[51]. Due to the time-varying behavior of the Doppler frequency shift, an efficient method of solving the problem of the smeared Fourier frequency spectrum and, hence, the blurred image, is to apply a high-resolution time-frequency transform to the Doppler processing. By replacing the Fourier transform with a high-resolution time-frequency transform, the image blurring caused by the time-varying Doppler frequency shifts can be mitigated without applying sophisticated focusing algorithms.

The Doppler frequency spectrum of moving targets is always time-varying. The relationship between the time-varying Doppler spectrum and the target's motion can be described by the translation-induced Doppler shift

▲ 14. Rotation motion represented by roll, pitch and yaw.

(b) ISAR Time-Frequency Based Images

(a) ISAR Fourier Based Image

▲ 14. Rotation motion represented by roll, pitch, and yaw.

caused by the time-varying Doppler's behavior without applying sophisticated focusing algorithms for individual scatterers.

Fig. 13 illustrates the time-frequency-based radar image formation [50], [51]. Standard range tracking and Doppler tracking are necessary prior to performing the time-frequency image formation. The difference between the time-frequency-based image formation and the conventional Fourier-based image formation is that the focusing procedure for individual scatterers is no longer needed in the time-frequency-based image formation and the Fourier transform is replaced by the time-frequency transform followed by time sampling. The Fourier-based imaging approach generates only one image frame from a radar data set $G\{r_m(n)\}$, where $r_m(n)$ is the m-th range profile of M range profiles and $n = 1,2,...,N$. However, the time-frequency-based image formation takes time-frequency transforms at each range cell and generates an $N \times N$ Doppler frequency (or Doppler) and dwell-time (or time) distribution. By combining the M Doppler time distributions at M-range cells, the $M \times N \times N$-range-Doppler-time cube $Q(r_m, f_n, t_n)$ can be formed

$$Q(r_m, f_n, t_n) = TF\{G[r_m(n)]\} \qquad (17)$$

where TF denotes the time-frequency operation with respect to n. At a particular time instant t_i, only one range Doppler image frame $Q(r_m, f_n, t_n = t_i)$ can be extracted from the cube. There are a total of N image frames available, and every one represents a full range-Doppler image at a particular instant. Therefore, by replacing the Fourier transform with the time-frequency transform, a 2-D range-Doppler Fourier image frame becomes a 3D range-Doppler-time image cube. By sampling in time, a time sequence of 2-D range Doppler images can be viewed [49]-[51]. Each individual time-sampled frame from the cube provides not only a clear image with superior resolution, but also time-varying properties from one time to another.

Time-Frequency Analysis for Moving Targets

A moving target always has translational and rotational motions during the imaging time. Assume the radar is located at the origin of the (u,v,w) frame of reference, and a target is located at a distance $R(u,v,w,t)$ from the radar at time t. The inertial coordinate of the target is the (x,y,z) frame. Thus, rotational motions of the target can be described by roll, pitch, and yaw [15], [18]. For an aircraft heading along the x-axis, roll corresponds to a rotation θ_r about the x-axis, pitch corresponds to a rotation θ_p about the y-axis, and yaw corresponds to a rotation θ_y about the z-axis (Fig. 14). If the order of rotations is a roll, followed by a pitch, and finally, a yaw, then the composite roll, pitch, and yaw motions can be represented by a rotation matrix

$$Rot(\theta_r, \theta_p, \theta_y) = Roll_x(\theta_r)Pitch_y(\theta_p)Yaw_z(\theta_y). \qquad (18)$$

According to this rotation matrix, any point scatterer on the target will move from its current location to a new location. When the target is rotating, the Doppler frequency spectrum of the returned signal from the target becomes time-varying, and the reconstructed image will be blurred. For example, if a target has pitch motion only, i.e., $\theta_r = \theta_y = 0$ and $\theta_p = \Omega_p t$, where Ω_p is the pitch rate, the rotation matrix becomes

$$Rot(\theta_r, \theta_p, \theta_y) = \begin{bmatrix} \cos\theta_p & 0 & \sin\theta_p & 0 \\ 0 & 1 & 0 & 0 \\ -\sin\theta_p & 0 & \cos\theta_p & 0 \\ 0 & 0 & 0 & 1 \end{bmatrix}. \qquad (19)$$

For a point scatterer at x,y,z, the Doppler frequency shift induced by the pitch motion becomes

$$f_{d_{pitch}} = \frac{2f_0}{c}\left[(-\Omega_p^2 t)x + \Omega_p z\right] \qquad (20)$$

where we assume the initial pitch angle is zero. Even if the pitch rate Ω_p is a constant, the motion-induced Doppler frequency shift $f_{d_{pitch}}$ is still time-varying. Assume the point scatterer at $x = 5$ m, $z = 0$ and the target rotating with a pitch rate of $\Omega_p = 0.14$ rad/s, from (20), the Doppler bandwidth is approximately 6 Hz. Consequently, if the Doppler resolution is 1 Hz, corresponding to a imaging time of 1 s, the motion-induced Doppler frequency of the scatterer will be smeared over 6 Doppler resolution cells, and the measurement of its true position will be uncertain.

Fig. 15(a) shows the conventional ISAR Fourier image of a target taken by a X-band radar operating at 9000 MHz [52]. Because the target is maneuvering, the Fourier image of the target is still blurred even after applying

From the insight into the image blurring, we can see that in order to achieve a clear image, the time-frequency transform should be used in place of the Fourier transform.

the standard procedure for focusing. By using the time-frequency-based image formation, because each scatterer has its own range and Doppler frequency shift at each time instant, without knowing any target's kinematic parameters and resampling the data, a blurred Fourier image becomes a sequence of clear time-frequency images. Fig. 15(b) shows one of these time-frequency images in which the nose, wing-tips, fuselage, and engines of the aircraft can be seen very clearly. The blurred image due to target maneuvering can be refocused without applying sophisticated autofocusing or motion compensation algorithms.

Summary

The Fourier transform has been widely used in radar signal and image processing. When the radar signals exhibit time- or frequency-varying behavior, an analysis that can represent the intensity or energy distribution of signals in the joint time-frequency domain is most desirable. In this article, we showed that JTF analysis is a useful tool for improving radar signal and image processing for time- and frequency-varying cases. We applied JTF analysis to radar backscattering and feature extraction; we also examined its application to radar imaging of moving targets. Other applications of time-frequency analysis to radar can also be found in [53]-[56].

Most methods of JTF analysis are non-parametric. However, parametric or model-based methods of time-frequency analysis, such as adaptive Gaussian and chirplets, are more suitable for radar signals and images [57]-[59].

Victor Chen is an Electronics Engineer and Staff Consultant at the Radar Analysis Branch of the Radar Division of the Naval Research Laboratory. *Hao Ling* is a Professor in the Department of Electrical and Computer Engineering at the University of Texas at Austin.

Acknowledgments

References

[1] S. Qian and D. Chen, "Joint time-frequency analysis," see this issue pp. 52-67.

[2] J.J. Eaves and E.K. Reedy, Eds., *Principles of Modern Radar*, New York: Van Nostrand Reinhold, 1987.

[3] M.I. Skolnik, *Introduction to Radar Systems*, 2nd edition, New York: McGraw-Hill, 1980.

[4] D.K. Barton, *Modern Radar System Analysis*, Norwood, MA: Artech House, 1988.

[5] D.T. Gjessing, *Target Adaptive Matched Illumination Radar: Principles and Applications*, London: Peter Peregrinus, 1986.

[6] D.K. Barton, "Land and clutter models for radar design and analysis," *Proc. IEEE*, vol. 73, no. 2, pp. 198-204, 1985.

[7] E.J. Kelly and R.P. Wishner, "Matched-filter theory for high-velocity targets," *IEEE Trans. Mil. Electron.*, vol. 9, pp. 56-69, 1965.

[8] S. Hudson and D. Psaltis, "Correlation filters for aircraft identification from radar range profiles," *IEEE Trans. Aerosp. Electron. Syst.*, pp. 741-748, vol. 29, no. 3, 1993.

[9] H.J. Li and S.H. Yang, "Using range profiles as feature vectors to identify aerospace objects," *IEEE Trans. Aerosp. Electron. Syst.*, vol. 41, no. 3, pp. 261-268, 1993.

[10] A. Zyweck and R.E. Bogner, "Radar target classification of commercial aircraft," *IEEE Trans. Aerosp. Electron. Syst.*, vol. 32, no. 2, pp. 598-606, 1996.

[11] V.C. Chen, "Radar range profile analysis with natural frame time-frequency representation," *SPIE Proc. on Wavelet Applications*, vol. 3078, pp.433-448, 1997.

[12] E.F. Knott, "Radar cross section," *Aspects of Modern Radar*, E. Brookner, Ed., Norwood, MA: Artech House, 1988.

[13] A.W. Rihaczek and S.J. Hershkowitz, *Radar Resolution and Complex-Image Analysis*, Boston: Artech House, 1996.

[14] R.O. Harger, *Synthetic Aperture Radar System*, New York: Academic Press, 1970.

[15] D.R. Wehner, *High-Resolution Radar*, 2nd edition, Boston: Artech House, 1994.

[16] W.G. Carrara, R.S. Goodman, and R.M. Majewski, *Spotlight Synthetic Aperture Radar–Signal Processing Algorithms*, Boston: Artech House, 1995.

[17] D.A. Ausherman, A. Kozma, J.L. Walker, H.M. Jones, and E.C. Poggio, "Developments in radar imaging," *IEEE Trans. Aerosp. Electron. Syst.*, vol. 20, no. 4, pp. 363-400, 1984.

[18] M.J. Prickett and C.C. Chen, "Principles of inverse synthetic aperture radar (ISAR) imaging," *Proc. IEEE 1980 EASCON*, pp. 340-345, 1980.

[19] C.C. Chen and H.C. Andrews, "Target motion induced radar imaging," *IEEE Trans. Aerosp. Electron. Syst.*, vol. 16, no. 1, pp. 2-14, 1980.

[20] J. Walker, "Range-Doppler imaging of rotating objects," *IEEE Trans. Aerosp. Electron. Syst.*, vol. 16, no. 1, pp. 23-52, 1980.

[21] D.E. Wahl, P.H. Eichel, D.C. Ghiglia, and C.V. Jakowatz, "Phase gradient autofocus–a robust tool for high-resolution SAR phase correction," *IEEE Trans. Aerosp. Electron. Syst.*, vol. 30, no. 3, pp. 827-834, 1994.

[22] J.C. Kirk, "Motion compensation for synthetic aperture radar," *IEEE Trans. Aerosp. Electron. Syst.*, vol. 11, no. 3, pp.338-348, 1975.

[23] B.D. Steinberg, "Microwave imaging of aircraft," *Proc. IEEE*, vol. 76, no. 12, pp. 1578-1592, 1988.

[24] H. Wu et al., "Translational motion compensation in ISAR image processing," *IEEE Trans. Image Processing*, vol. 14, no. 11, pp. 1561-1571, 1995.

[25] A.B. Baqai and Y. Hua, "Matrix pencil methods for ISAR image reconstruction," *Proc. ICASSP*, pp. 473-476, 1993.

[26] S.A. Werness, W.G. Carrara, L.S. Joyce and D.B. Franczak, "Moving target imaging algorithm for SAR data," *IEEE Trans. Aerosp. Electron. Syst.*, vol. 26, no. 1, pp. 57-67, 1990.

[27] J.W. Odendaal, E. Barnard, and W.I. Pistorius, "Two-dimensional superresolution radar imaging using the MUSIC algorithm," *IEEE Trans. Antennas and Propagat.*, vol. 42, no. 10, pp. 1386-1391, 1994.

[28] I.J. Gupta, "High-resolution radar imaging using 2-D linear prediction," *IEEE Trans. Antenna and Propagat.*, vol. 42, no. 1, pp. 31-37, 1994.

[29] J. Li ands P. Stoica, "An adaptive filtering approach to spectral estimation and SAR imaging," *IEEE Trans. Signal Processing*, vol. 44, no. 6, pp. 1469-1484, 1996.

[30] R. Wu, Z.S. Liu , and J. Li, "Time-varying complex spectral estimation with applications to ISAR imaging," *Proc. 1998 Asilomar Conference on Signals, Systems, and Computers*, Pacific Grove, CA, scheduled for publication.

[31] K.F. Casey, D.G. Dudley and M.R. Portnoff, "Radiation and dispersion effects from frequency-modulated (FM) sources," *Electromagnetics*, vol. 10, pp. 349-376, 1990.

[32] A. Moghaddar and E.K. Walton, "Time-frequency-distribution analysis of scattering from waveguide cavities," *IEEE Trans. Antennas Propagat.*, vol. 41, no. 5, pp. 677-680, 1993.

[33] H. Kim and H. Ling, "Wavelet analysis of radar echo from finite-size targets," *IEEE Trans. Antennas Propagat.*, vol. 41, no. 2, pp. 200-207, 1993.

[34] J. Moore and H. Ling, "Time-frequency analysis of the scattering phenomenology in finite dielectric gratings," *Microwave Optical Tech. Letters*, vol. 6, pp. 597-600, Aug. 1993.

[35] F. Ling, J. Moore, D. Bouche and V. Saavedra, "Time-frequency analysis of backscattered data from a coated strip with a gap," *IEEE Trans. Antennas Propagat.*, vol. 41, no. 8, pp. 1147-1150, 1993.

[36] L. Carin and L.B. Felsen, "Wave-oriented data processing for frequency- and time-domain scattering by nonuniform truncated arrays," *IEEE Antennas and Propagat. Magazine*, vol. 36, pp. 29-43, June 1994.

[37] J.C. Goswami, A.K. Chan and C.K. Chui, "An application of fast integral wavelet transform to waveguide mode identification," *IEEE Trans. Microwave Theory Tech.*, vol. 43, pp. 655-663, Mar. 1995.

[38] J. Moore and H. Ling, "Super-resolved time-frequency analysis of wideband backscattered data," *IEEE Trans. Antennas Propagat.*, vol. 43, no. 6, pp. 623-626, 1995.

[39] L.C. Trintinalia and H. Ling, "Interpretation of scattering phenomenology in slotted waveguide structures via time-frequency processing," *IEEE Trans. Antennas Propagat.*, vol. 43, no. 11, pp. 1253-1261, 1995.

[40] A. Filindras, U.O. Larsen and H. Ling, "Scattering from the EMCC dielectric slabs: simulation and phenomenology interpretation," *J. Electromag. Waves Applications*, vol. 10, pp. 515-535, Apr. 1996.

[41] L. Carin, L.B. Felsen, D.R. Kralj, H.S. Oh, W.C. Lee, and S.U. Pillai, "Wave-oriented signal processing of dispersive time-domain scattering data," *IEEE Trans. Antennas Propagat.*, vol. 45, no. 4, pp. 592-600, 1997.

[42] C. Ozdemir and H. Ling, "Interpretation of scattering phenomenology in dielectric-coated wires via joint time-frequency processing," *IEEE Trans. Antennas Propagat.*, vol. 45, no. 8, pp. 1259-1264, 1997.

[43] L.C. Trintinalia and H. Ling, "Joint time-frequency ISAR using adaptive processing," *IEEE Trans. Antennas Propagat.*, vol. 45, no. 2, pp. 221-227, 1997.

[44] S. Qian and D. Chen, "Signal representation using adaptive normalized Gaussian functions," *J. Signal Processing*, vol. 36, no. 1, pp. 1-11, Mar. 1994.

[45] S.G. Mallat and Z. Zhang, "Matching pursuits with time-frequency dictionaries," *IEEE Trans. Signal Processing*, vol. 41, no. 12, pp. 3397-3415, 1993.

[46] H.T.G. Wang, M.L. Sanders and A. Woo, "Radar cross section measurement data of the VFY 218 configuration," Tech. Rept. NAWCWPNS TM-7621, Naval Air Warfare Center, China Lake, CA, Jan. 1994.

[47] B. Borden, "An observation about radar imaging of re-entrant structures with implications for automatic target recognition," *Inverse Problems*, vol. 13, pp. 1441-1452, 1997.

[48] V.C. Chen, "Radar ambiguity function, time-varying matched filter, and optimum wavelet correlator," *Optical Engineering*, vol. 33, no. 7, pp. 2212-2217, 1994.

[49] V.C. Chen, "Reconstruction of inverse synthetic aperture radar image using adaptive time-frequency wavelet transform," *SPIE Proc. Wavelet Applications*, vol. 2491, pp. 373-386, 1995.

[50] V.C. Chen, "Applications of time-frequency processing to radar imaging," *Optical Engineering*, vol. 36, no. 4, pp. 1152-1161, 1997.

[51] V.C. Chen and S. Qian, "Joint time-frequency transform for radar range-Doppler imaging," *IEEE Trans. Aerosp. Electron. Syst.*, vol. 34, no. 2, pp. 486-499, 1998.

[52] V.C. Chen, "Time-frequency processing for radar imaging," *1998 NRL Review*, pp. 131-133, 1998.

[53] S. Barbarossa and A. Farina, "Detection and imaging of moving objects with synthetic aperture radar – Part 2: Joint time-frequency analysis by Wigner-Ville distribution," *IEE Proc. Radar, Sonar, Navigation*, vol. 139, no. 1, pp. 89-97, 1992.

[54] Y. Wang, H. Ling, and V.C. Chen, "ISAR motion compensation via adaptive joint time-frequency technique," *IEEE Trans. Aerosp. Electron. Syst.*, pp. 670-677, vol. 34, no. 2, 1998.

[55] O.P. Kenny and B. Boashash, "Time-frequency analysis of backscattered signals from diffuse radar targets," *IEEE Proc.-F.* vol. 140, no. 3, pp. 198-208, 1993.

[56] C. Xu, Z. Chai, S. Shu, and M. Zhu, "SAR detection of moving targets using approximate wavelet transform and time-frequency analysis," *Proc. 1997 IEEE Int. Symp. Circuits and Systems*, Hong Kong, pp. 2561-2564, 1997.

[57] S. Mann and S. Haykin, "The chirplet transform: Physical considerations," *IEEE Trans. Signal Processing*, vol. 43, no. 11, pp. 2745-2761, 1995.

[58] D. Mihovilovic and R.N. Bracewell, "Adaptive chirplet representation of signal on time-frequency plane," *Electronics Letters*, vol. 27, no. 13, pp. 1159-1161, 20 June, 1991.

[59] S. Qian, D. Chen, and Q. Yin, "Adaptive chirplet based signal approximation," *ICASSP'98*, pp. 1781-1784, 1998.

ISAR imaging of targets with fast rotating parts using adaptive joint time-frequency processing

Y. Wang[a], H. Ling[a] and V. C. Chen[b]

[a]Department of Electrical and Computer Engineering,
The University of Texas at Austin, Austin, TX 78712-1084

[b]Airborne Branch, Naval Research Laboratory
Washington, DC 20375

ABSTRACT

Based on the adaptive joint time-frequency processing techniques, a new methodology is proposed in this paper to separate the interference due to fast rotating parts from the original ISAR image of the target. The technique entails adaptively searching for the linear chirp bases which best represent the time-frequency behavior of the signal and fully parameterizing the signal with these basis functions. The signal components due to the fast rotating part are considered to be associated with those chirp bases having large displacement and slope parameters, while the signal components due to the target body motion are represented by those chirp bases which have relatively small displacement and slope parameters. By sorting these chirp bases according to their slopes and displacements, the scattering due to the fast rotating part can be separated from that due to the target body. Consequently, the image artifacts overlapping with the original image of the target can be well removed and a clean ISAR image can be produced. Successful applications of the algorithm to numerically simulated and measurement data show the robustness of the algorithm.

Keywords: ISAR imaging, Doppler smearing, fast rotating parts, adaptive joint time-frequency processing

1. INTRODUCTION

It is well known that when rotating components exist on a target such as gimbaled antennas or propeller blades, image artifacts are introduced in the Doppler dimension of the inverse synthetic aperture radar (ISAR) image[1,2,3]. The reason is those parts are often rotating at a speed much faster than the target itself and the Doppler frequencies involved by them are often much higher than the radar pulse repetition rate. Therefore serious aliasing can happen and result in smearing through all the cross range dimension of the image. These smeared features oftentimes overshadow the target geometrical features and hinder the proper interpretation of the ISAR image. To enhance such an image, the most often used approach is to simply estimate the size of the target in the cross range dimension, keep the signal components inside the target dimension and discard all the other unwanted components outside the confined region. By this approach one can get rid of most of the Doppler smearing if the actual size of the target is known. However, in most of the real world ISAR applications, the target is unknown and it is difficult to give a close estimation of the target size. An over estimation of the target size must be used to assure most of the target features are kept in the image, while it may result in poor elimination of the Doppler smearing. Besides, even if the size of the target is accurately known, those Doppler smearing overlapping with target features can never be eliminated by this gating technique, since they are within the geometrical dimension of the target. To overcome this difficulty, a technique is presented in this paper to remove such Doppler smearing and produce a clear ISAR image of the target based on the adaptive joint time-frequency processing.

The original concept of adaptive joint time-frequency processing was proposed in the signal processing society[4,5] and applied to ISAR image processing in the joint time-frequency space for resonant scattering mechanism extraction[6,7] and target motion compensation[8,9]. Comparing to the regular processing in either the time or the frequency domain, more insights into the underlying physical mechanisms can be gained in the joint time-frequency plane because it takes the advantage of the instantaneous frequency behaviors of the signal. The technique entails adaptively searching for the linear

chirp bases which best represent the time-frequency behavior of the signal. This is accomplished by projecting the signal onto all possible chirp bases and finding the one with the maximum projection value. After the optimal basis is found, the signal component associated with this basis is subtracted from the original signal. By iterating this search procedure, the signal can be fully parameterized with a set of chirp basis functions. Since the Doppler frequency due to the rotating component is both higher and more rapidly varying (in dwell time) than that from the target body, the signal components due to the fast rotating part are associated with those chirp bases having large displacement and slope parameters. On the other hand, those chirp bases which have relatively small displacement and slope parameters represent the signal components due to the target body motion. By sorting these chirp bases according to their slopes and displacements, the scattering due to the fast rotating part can be separated from that due to the target body. Consequently a cleaned ISAR image of the target body can be reconstructed by using only those bases associated with the body motion. Furthermore, if the pulse repetition rate (PRF) of the radar is high enough, an image of the rotating part can also be constructed by removing the body interference. We shall present the results of applying this algorithm to simulated data from the radar scattering prediction code Xpatch.

2. ADAPTIVE JOINT TIME-FREQUENCY PROCESSING

ISAR imaging is a simple and robust process for mapping the position and magnitude of the target scattering features based on a point scatterer assumption of the target. With this assumption, the target consists of a group of point scatterers. Therefore the radar scattering signal collected versus frequency and observation angle can be described as:

$$E(f, \theta) = \sum_{i=1}^{N} O(x_i, y_i) e^{-2jkx_i \cos\theta - 2jky_i \sin\theta} \tag{1}$$

where $O(x_i, y_i)$ is the amplitude of the ith scattering center, k is the free space wave number. In real radar measurements for targets in flight, the looking angle is usually unknown but scaled according to the observation dwell time. If the target is rotating with respect to the radar, the signal can be written as:

$$E(f, t_D) = \sum_{i=1}^{N} O(x_i, y_i) e^{-2jkx_i \cos(\Omega t_D) - 2jky_i \sin(\Omega t_D)} \tag{2}$$

where Ω is the angular rotation velocity of the target. Note that if the sinusoid functions are simplified under the small observation angle approximation, the range and cross range information can be obtained by Fourier transforming the signal from the frequency and dwell time domain [1]. However, when fast rotating parts exist on the target, eq.(2) doesn't hold any more and has to be rewritten to include the scattering from the parts that are rotating at a different velocity. We limit the discussion to the case when only one rotation speed exists for those parts other than the target motion and replace (2) by the following:

$$E(f, t_D) = \sum_{i=1}^{N_b} O(x_i, y_i) e^{-2jkx_i \cos(\Omega_b t_D) - 2jky_i \sin(\Omega_b t_D)} +$$
$$\sum_{i=N_b+1}^{N} O(x_i, y_i) e^{-2jkx_i \cos(\Omega_p t_D) - 2jky_i \sin(\Omega_p t_D)} \tag{3}$$

where N_b is assumed to be the number of all the scatterers in the target body, Ω_b and Ω_p are respectively the angular velocities of the target body and the fast rotating parts. Usually Ω_p is much greater than Ω_b. In order to image the target, the observation time is chosen to allow the target to be observed for a small range of angles. While the first term in (3) can still be projected to the image of the target via the Fourier transform, the second term may result in serious Doppler smearing in cross range domain and overshadow the target features since the small angle approximation does not hold any more. For this reason, the signal have to be separated for different motion mechanisms before the regular Fourier processing can be applied.

We shall utilize the adaptive joint time-frequency processing technique to achieve this goal. The algorithm implemented here is very similar to that in our earlier work [8]. The criterion to tell the two components of the signal in (3) is according to their

different Doppler frequencies versus dwell time characteristics. For the component due to target body scattering, the Doppler frequency is:

$$f_D^b = 2K_c\Omega_b[y\cos(\Omega_b t_D) + x\sin(\Omega_b t_D)] \cong 2K_c\Omega_b(y + x\Omega_b t_D) \tag{4}$$

which is generally a linear function of dwell time with very small slope and displacement parameters because Ω_b is very small and the small angle approximation can be applied. On the other hand, the Doppler frequency due to the fast rotating parts is basically a sinusoid function of dwell time as:

$$f_D^p = 2K_c\Omega_p[y\cos(\Omega_p t_D) + x\sin(\Omega_p t_D)] \tag{5}$$

Note that both the amplitude and frequency of this sinusoid are scaled by Ω_p. This means the Doppler frequency can either be very large or fast varying versus dwell time. Thus the signal can also be characterized by the linear chirp bases in dwell time-Doppler frequency plane but with either large displacement parameters or large slope parameters. Consequently, if the signal can be fully parameterized by these bases, the component due to the fast rotating parts can be easily separated from the component due to target body motion by sorting them into different categories according to their parameters. This concept is depicted in Fig.1 to state the different time-frequency behaviors of the signal components due to the steady scattering centers on the target body and the fast rotating parts. To carry out the parameterization and sorting process, we utilize the adaptive joint time-frequency processing technique to be described as follows.
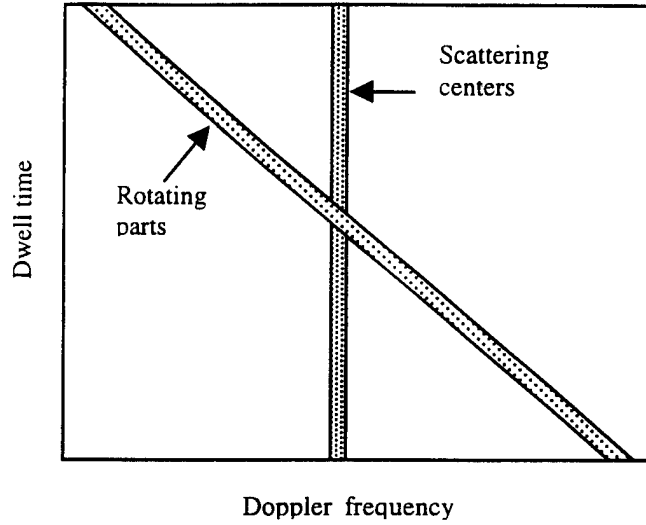

Fig.1. The time-frequency characteristics of the components due to scattering centers and rotating parts.

First, the chirp basis functions with linear characteristics in the (dwell time)-(Doppler frequency) plane are constructed with only linear and quadratic phase terms:

$$h_p(t_D) = \exp[-j2\pi(f_0 t_D + \tfrac{1}{2}f_1 t_D^2)] \tag{6}$$

where the linear phase coefficient f_0 is the displacement parameter in the time-frequency plane and the quadratic phase coefficient f_1 is the slope parameter. We shall process the Doppler signal for each range cell independently instead of for each frequency, since the Doppler smearing due to the rotating parts is well isolated in a finite number of range cells. Thus we search the chirp basis function which best represents the time-frequency behavior of the signal for each range cell by maximize the projection value of the signal to the basis:

$$\left|B_p\right|^2 = \max_{f_0, f_1, \cdots} \left|\int R_p(x, t_D) h_p^*(t_D) dt\right|^2 \tag{7}$$

where $R(x, t_D)$ is the range profile which is the 1-D Fourier transform of the original signal $E(f, t_D)$ from the frequency domain to the range domain. The search for the first order coefficient can be accomplished by using the FFT algorithm. Then only a one-dimensional search is required to find f_1. This procedure is equivalent to picking out the strongest chirp component of the signal in the time-frequency plane with the resolution of the full Doppler bandwidth. The index p denotes the signal is in the pth stage of the iterative procedure since this process will be repeated for the residue signal which is:

$$R_{p+1}(x, t_D) = R_p(x, t_D) - B_p \cdot h_p(t_D) \tag{8}$$

Therefore, this searching-extraction process will be iterated until the energy of the residue signal is smaller than a preset threshold. At this stage, the signal has been fully parameterized as a sum of all these bases. The signal component due to the target body scattering can thus be reconstructed by summing all the bases with small displacement and small slope parameters. In this manner, a clean ISAR image of the target body can be obtained via the standard Fourier processing.

3. NUMERICAL SIMULATION AND EXAMPLES
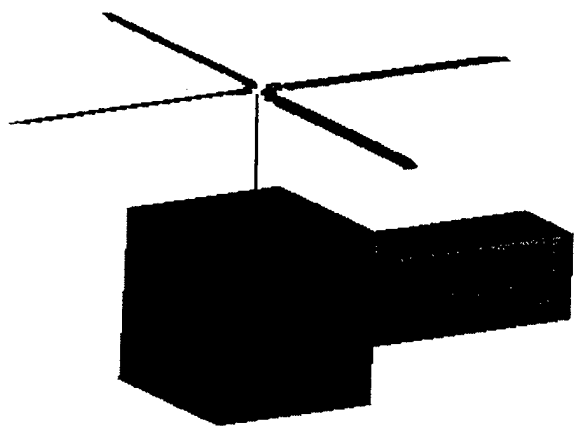
Fig.2. The geometry of the helicopter model.
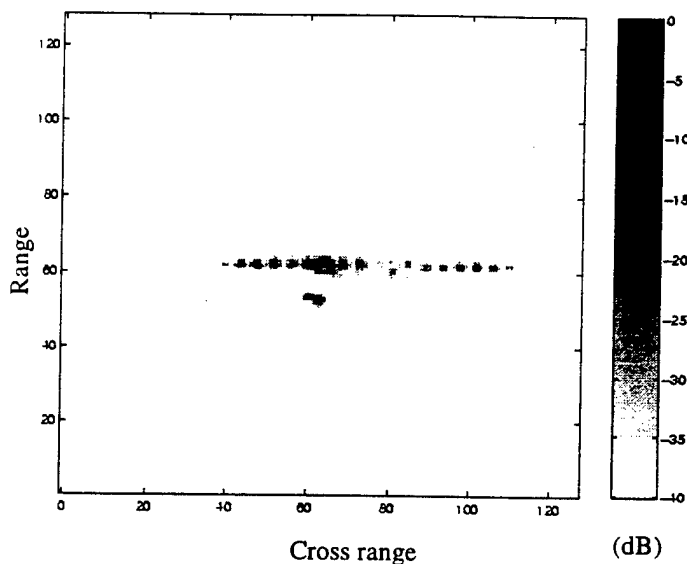
Fig.3. The primitive ISAR image obtained directly via the Fourier transform.

To verify the algorithm and better explain the advantage of the algorithm, we have simulated the radar scattering from a helicopter model using an electromagnetic prediction code Xpatch which is based on the shooting and bouncing ray technique [10] and tested our algorithm using the simulation data. The geometry of the helicopter model is plotted in Fig.2. There are four blades on the rotor. The length of the blade is 10 feet. The target body is simply made by connecting two conducting boxes, which are respectively 6.56×6.56×6.56 feet and 9.84×3.28×3.28 feet. In the Xpatch simulation, the radar scattering is observed for 128 frequency points from 1.75 GHz to 2.25 GHz and 128 points in target aspect from 158 degrees to 170 degrees, but from 0 degree to 360 degrees for the blade aspect. The elevation aspect angle of the target is 20 degrees. Under this parameters, if the rotation velocity of the target body is 12 rpm, the blade will be spinning at a speed 30 times of it, which is 360 rpm. The standard ISAR image of the target is obtained via a 2-D Fourier transform as shown in
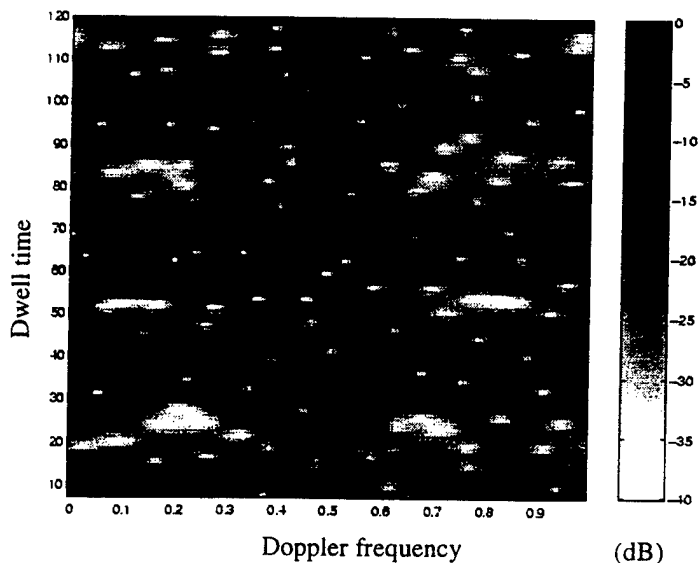

Fig.4. The dwell time-Doppler frequency spectrogram of the signal at the range cell 60.

Fig.3. The target body scattering features are confined to a small extent around the center of the cross range, while the scattering components due to the fast rotating blades behave like strong Doppler smearing lines running across the whole cross range domain and overlapping with the scattering features of the target body. To observe the (dwell time)-(Doppler frequency) behaviors of the signal with Doppler smearing, we choose the range cell 60 and use the short time Fourier transform to display the time frequency spectrogram in Fig. 4. Although the resolution is bad due to the short time Fourier transform, we can still see there are two kinds of time-frequency behaviors going on in Fig.4. One is those components around the zero Doppler frequency (the center), which behave like straight lines with very little slope. It represents the scattering from the scattering centers on the target body. The other time-frequency mechanism is those lines going through the entire Doppler frequency domain. Instead of the sinusoid like time-frequency behavior mentioned in the last section, these lines are the results of serious aliasing effect in the Doppler frequency Domain. The aliasing occurs whenever the highest Doppler frequency induced by the fast rotating parts is greater than the radar pulse repetition rate (PRF), which causes serious aliasing in Doppler frequency domain. Even though the sinusoid behavior can no longer be seen, the linear chirp description of the time-frequency behavior due to the rotating parts is still effective. The chirp basis functions, however, have to be defined with very large slope parameters to well represent the aliasing effect.

Fig.5. The ISAR image obtained by gating out the Doppler component outside the estimated target region.

As far as the ISAR image in Fig.3 is concerned, the standard way to process it is to estimate the target dimension and the corresponding Doppler frequency extent, and then gate out the unwanted Doppler frequency components. For this example, we choose a Doppler frequency window which allows about twice of the target dimension and zoom-in on this region. The resulting image is plotted as Fig.5. Note that little is done to eliminate the Doppler smearing that overlaps with the target features. Now the adaptive joint time-frequency processing is applied to the original signal. First we Fourier transform the original frequency-aspect data to the range-aspect domain. Then for each range cell, the signal is projected to all possible bases until the optimal chirp basis is found and extracted. The procedure is repeated until the residue energy is less than 2% of the energy of the strongest range cell. Usually, it takes less than 200 terms to parameterize the signal with the residue energy less than such a threshold. It has been noted that in the search the slope parameters of the bases should be large enough to represent the dramatic phase variation of the

Fig.6. The ISAR image after applying the adaptive joint time-frequency processing to remove the Doppler smearing.

Doppler signals due to the fast rotating parts. After the parameterization is done, the basis functions are divided into two categories according to their slope and displacement parameters. Here we choose an appropriate small number as the threshold of slope. The threshold of displacement is chosen the same as in the standard approach. Only those bases with both the slope and the displacement lower than the thresholds are kept as the components due to the scattering from the target
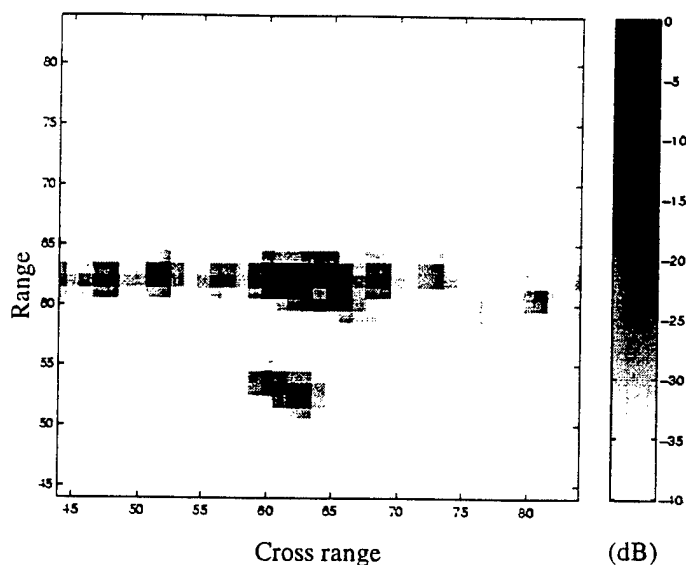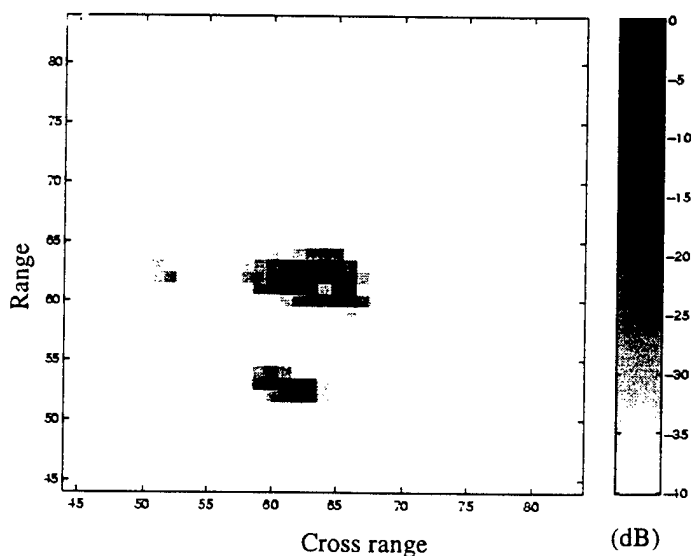
body. Summing up these bases and Fourier transforming it to the image domain, a clean ISAR image is obtained in Fig.6. We observe that most of the Doppler smearing is eliminated. For a better assessment of the Doppler smearing removal, the ISAR image simulated for the target without the rotating blades is also generated in Fig.7. From the comparison, it is seen that the algorithm has successfully kept almost all the scattering features due to the target body, but has removed most of the Doppler smearing interference due to the rotating parts from the image.

4. IMAGE RECONSTRUCTION FOR THE ROTATING PARTS

In the above adaptive joint time-frequency processing, the scattering component due to the rotating parts can also be isolated in the process. It consists of the bases with either the slope parameters or the displacement parameters larger than the thresholds. If the signal is seriously aliased, it is difficult to gather any useful information on the rotating parts. Nevertheless, if the PRF of the radar is high enough to avoid aliasing, we should be able to generate an image for the rotating parts as well. However, just as in the case of the Doppler signal from the rotating parts causing artifacts in the image of the target body, the scattering of the target body can also cause artifacts in the image of the blades. For example, we simulate the radar scattering of the same target again using Xpatch for the same frequency sampling but 128 observation angles from 0 degree to 12 degrees for the blades. In this range, the body rotates only 0.4 degrees. Although the blades can be imaged clearly, the poor resolution for the body compresses the body image into zero cross range as shown in Fig.8.

In conjunction with the information provided by the parameterization, it is also possible to suppress this body interference. Note that the scattering component due to the target body is parameterized as a sum of chirp basis functions versus dwell time. The parameterization model expression is still effective even for the shorter observation period. The scattered fields due to the target body can thus be interpolated to the dense sampling used to observe the blades and be subtracted from the total scattering fields. The ISAR image of the blades with the body interference suppressed is obtained as Fig.9. Comparing the results with the ISAR image simulated with the blades only in Fig.10, the body line interference is much weaker but not completely eliminated. The reason could be the effects due to the multiple scattering mechanism simulated by Xpatch, in which the total scattered fields can no longer be written as the sum of the scattered fields due to the target body and due to the blades.
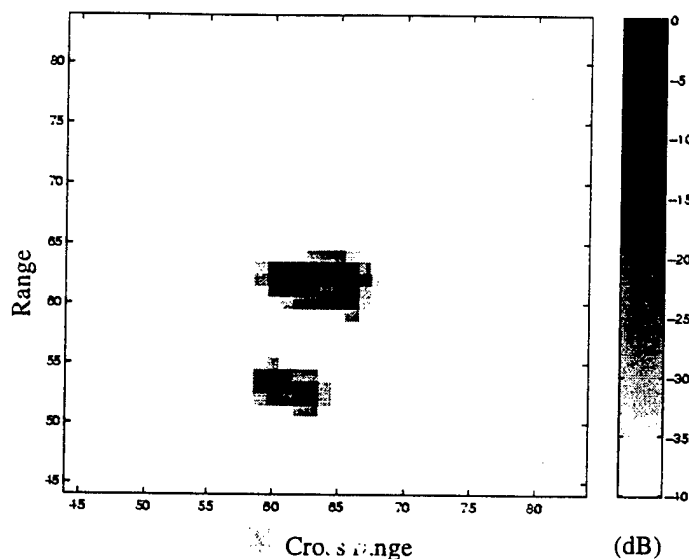

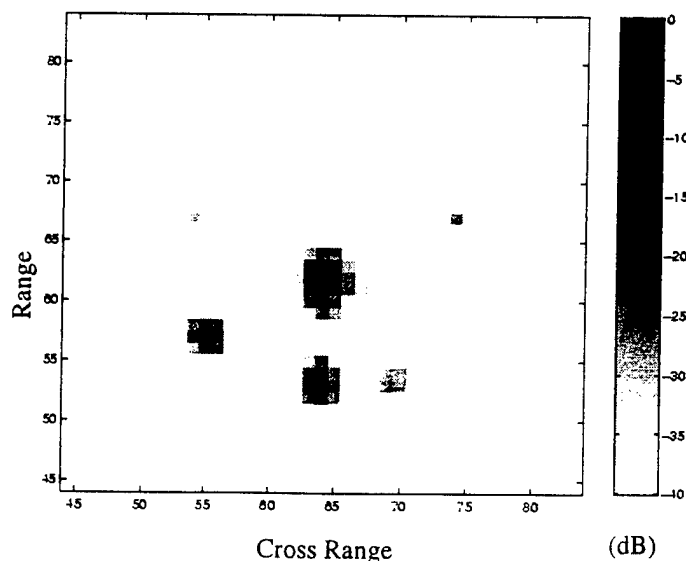Fig.7. The ISAR image of the target body simulated without the rotating blades.

Fig.8. The ISAR image of the blades with the body interference.

5. SUMMARY

In this paper we have applied adaptive joint time-frequency ideas to separate two different scattering mechanisms respectively due to the target body and the fast rotating parts on the target. This is accomplished by taking the advantage of their different (dwell time)-(Doppler frequency) behaviors. After adaptively searching for the linear chirp bases which best represent the time-frequency behavior of the signal and fully parameterizing the signal with these basis functions, we can sort these bases into the signal component due to the fast rotating parts and the component due to target body motion according to their slope and displacement parameters. The Doppler smearing interference caused by the fast rotating parts can be removed from the original ISAR image by keeping only those bases associated with target body scattering. The algorithm has been tested for numerical simulated radar scattering data for a helicopter model. The ISAR image obtained by removing the Doppler smearing from the original image agrees well with the image simulated for the target without the rotating blades on. Furthermore, the algorithm has also been extended to image the fast rotating blades with body interference removed for radar with high PRF. This algorithm has been applied to the measurement data for real targets. These results will be presented in the talk.
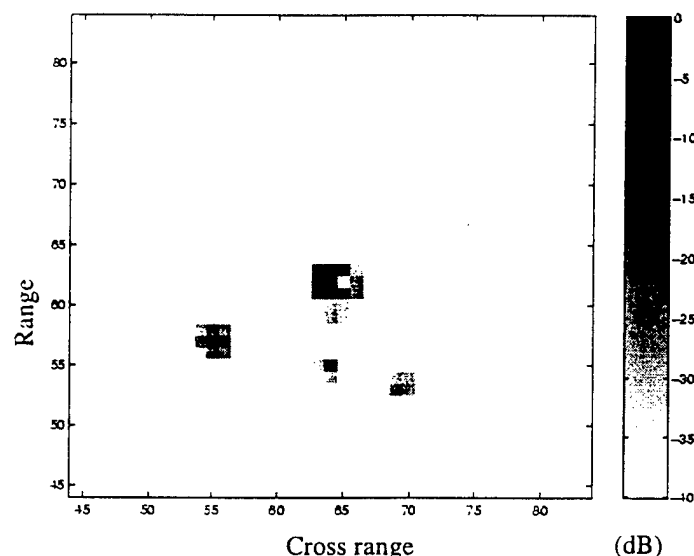
ACKNOWLEDGMENTS

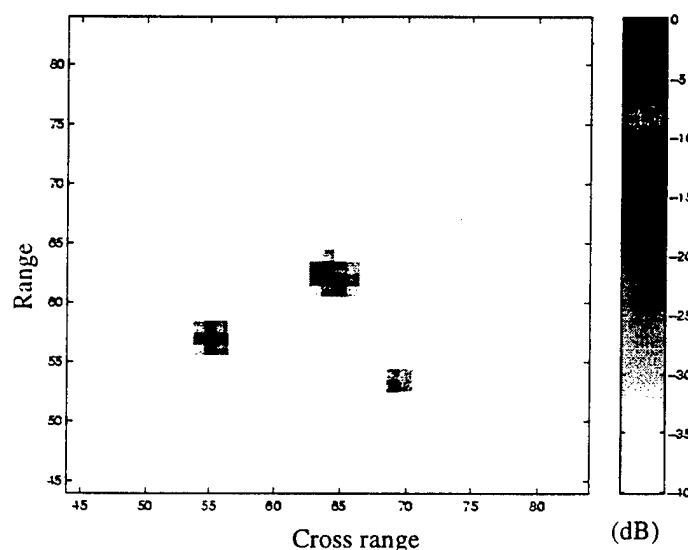Fig.9. The ISAR image of the blades with the body interference removed.

Fig.10. The ISAR image simulated with the blades only.

REFERENCES

1. D. L. Mensa, *High Resolution Radar Imaging*. Artech House, Dedham, MA, 1981.
2. C. C. Chen and H. C. Andrews, "Target motion induced radar imaging", *IEEE Trans. Aerospace Electron. Syst.*, vol. 16, pp. 2-14, Jan, 1980.
3. A. Ausherman, A. Kozma, J. L. Waker, H. M. Jones and E. C. Poggio, "Developments in radar imaging", *IEEE Trans. Aerospace Electron. Syst.*, vol. 20, pp. 363-400, April 1984.

4. S. Qian and D. Chen, "Signal representation using adaptive normalized Gaussian functions," *Signal Processing*, vol. 36, no. 1, pp. 1-11, Mar. 1994.
5. S. G. Mallat and Z. Zhang, "Matching pursuits with time-frequency dictionaries," *IEEE Trans. Signal Processing*, vol. 41, pp. 3397-3415, Dec. 1993.
6. L. C. Trintinalia, and H. Ling, "Joint time-frequency ISAR using adaptive processing," *IEEE Trans. Antennas and Propagat.*, vol. AP-45, pp. 221-227, Feb. 1997.
7. L. C. Trintinalia and H. Ling, "Extraction of waveguide scattering features using joint time-frequency ISAR," *IEEE Microwave Guided Wave Lett.*, vol. 6, pp. 10-12, Jan. 1996.
8. Y. Wang, H. Ling and V. C. Chen, "ISAR motion compensation via adaptive joint time-frequency techniques," to appear in *IEEE Trans. Aeros. and Electron. Sys.*, Oct. 1998.
9. H. Ling, Y. Wang, and V. C. Chen, "ISAR image formation and feature extraction using adaptive joint time-frequency processing," *SPIE AeroSense'97*, 424-432, Orlando, FL, Apr. 1997.
10. R. Bhalla and H. Ling, "A fast algorithm for simulating doppler spectra of targets with rotating parts using the shooting and bouncing ray technique," submitted to *IEEE Trans. Antennas and Propagat.*, July 1997.
11. V. C. Chen, "Reconstruction of inverse synthetic aperture images using adaptive time-frequency wavelet transforms," *SPIE Proc. on Wavelet Application*, vol. 2491, pp. 373-386, 1995.
12. S. Qian and D. Chen, "Decomposition of the Wigner-Ville distribution and time-frequency distribution series," *IEEE Trans. Signal Process.*, vol. 42, pp. 2836-2842, Oct. 1994.
13. J. C. Wood and D. T. Barry, "Radon transformation of time-frequency distributions for analysis of multicomponent," *IEEE Trans. Signal Process.*, vol. 42, pp. 3166-3177, Nov. 1994.

Joint time-frequency analysis of electromagnetic backscattered data

Hao Ling

Department of Electrical and Computer Engineering
The University of Texas at Austin
Austin, TX 78712-1084

ABSTRACT

The application of joint time-frequency techniques for the analysis of electromagnetic backscattered data is reviewed. In the joint time-frequency feature space, discrete time events such as scattering centers, discrete frequency events such as target resonances, and dispersive mechanisms due to surface waves and guided modes can be simultaneously displayed. We discuss the various joint time-frequency representations including the short-time Fourier transform, wavelet transform, Wigner-Ville distribution, windowed super-resolution algorithms and the adaptive spectrogram. Emphasis is placed on how these algorithms can be used to represent with good resolution the scattering phenomenology in electromagnetic data. We highlight an application of joint time-frequency processing for radar image enhancement and feature extraction. It is shown that by applying joint time-frequency processing to the conventional inverse synthetic aperture radar (ISAR) imagery, it is possible to remove non-point scattering features in the image, leading to a cleaned image containing only physically meaningful point scatterers. The extracted frequency-dependent mechanisms can be displayed in an alternative feature space to facilitate target identification.

Keywords: joint time-frequency analysis, electromagnetic scattering, feature extraction, radar imaging

1. INTRODUCTION

The usefulness of the joint time-frequency analysis of signals has long been recognized in the signal processing arenas.[1,2] Recently, joint time-frequency methods have also been applied to electromagnetic data with good success. The joint time-frequency representation of a signal is a two-dimensional phase space that facilitates the visualization and interpretation of complex electromagnetic wave phenomenology. In this feature space, discrete time events such as scattering centers, discrete frequency events such as resonances, and dispersive mechanisms due to surface waves and guided modes can be simultaneously displayed. This can oftentimes lead to more insights into the complex electromagnetic wave propagation and scattering mechanisms than what is available in the traditional time or frequency domain alone. The objectives of this paper are to provide an overview of the various joint time-frequency techniques and to show how they can be applied to extract meaningful phenomenology-based features from electromagnetic data. We will discuss various time-frequency representations of signals including the short-time Fourier transform, wavelet transform, Wigner-Ville distribution, windowed super-resolution algorithms and the adaptive spectrogram. Emphasis will be placed on how electromagnetic phenomenology is manifested in the joint time-frequency plane and how these features can be interpreted and extracted. We will highlight an application of joint time-frequency processing for radar image enhancement and feature extraction.

The standard tool in generating the joint time-frequency representation of a signal is the short-time Fourier transform (STFT). First introduced by Gabor in 1946, it is basically a sliding window Fourier transform in time. First, let us define the Fourier transform of a signal f(t):

$$F(\omega) = \int_{-\infty}^{\infty} f(t)\, e^{-j\omega t}\, dt \tag{1}$$

By taking the Fourier transform of the windowed time data as the window is moved in time, a two-dimensional time-frequency image, or the spectrogram, is generated:

$$\text{STFT } (\tau, \Omega) = \int f(t) \ g(t\text{-}\tau) \ e^{-j\Omega t} \ dt \tag{2}$$

Equation (2) is very similar to the Fourier transform defined in (1), except for the presence of a frequency window function g(t). The definition of the STFT can also be expressed in the time domain by manipulating (3a), with the result:

$$\text{STFT } (\tau, \Omega) = \frac{1}{2\pi} \ e^{-j\Omega \tau} \int F(\omega) \ G(\Omega\text{-}\omega) \ e^{j\tau\omega} \ d\omega \tag{3}$$

Here G(ω) is the inverse Fourier transform of g(t). The dual relationship between (2) and (3) is apparent, i.e., the time-frequency representation can be obtained through either a moving window in time or a moving window in frequency. In addition, we make the following observations: (i) Time signals with duration shorter than the duration of the window will tend to get smeared out, i.e., the resolution in the time domain is limited by the width of the window g(t). Similarly the resolution in the frequency domain is limited by the width of the frequency window G(ω). (ii) The window width in time and the window width in frequency are inversely proportional to each other by the uncertainty principle. Therefore, good resolution in time (small time window) necessarily implies poor resolution in frequency (large frequency window). (iii) The window width in each domain remains fixed as it is translated. This results in a fixed resolution across the entire time-frequency plane.
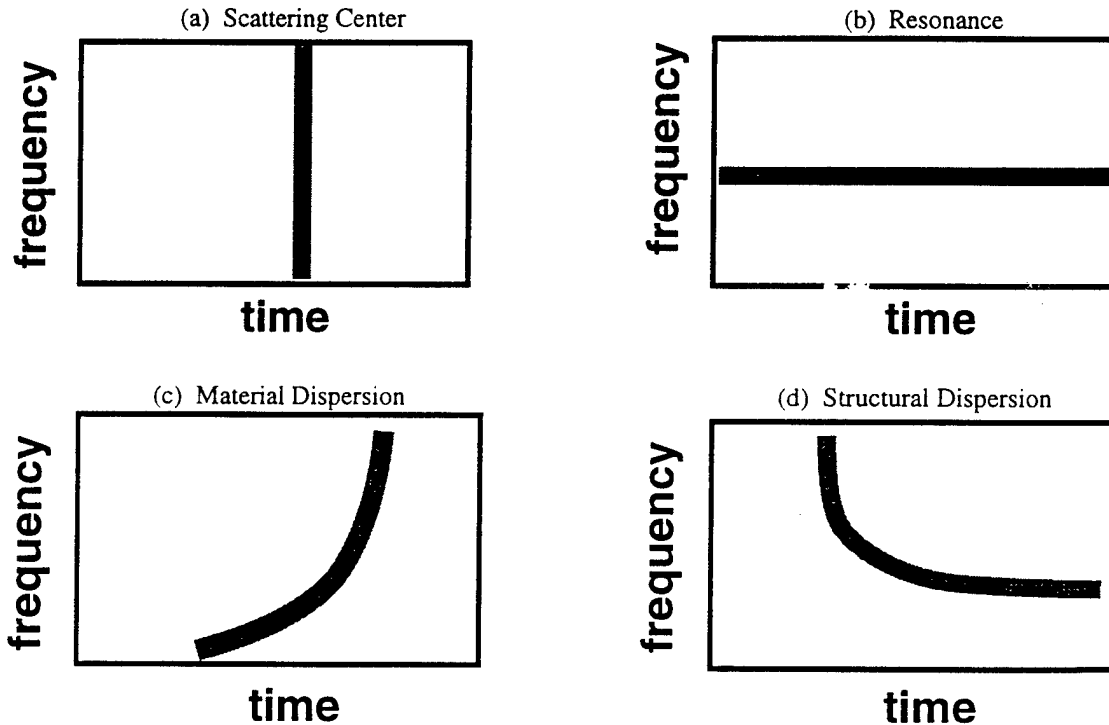

Fig. 1.   Electromagnetic mechanisms are manifested in the joint time-frequency image as distinct features.

The spectrogram provides information on the frequency content of the signal at different time instances. In electromagnetic applications, the joint time-frequency image can be used to simultaneously display the different wave phenomenology due to discrete events of time, discrete events of frequency and dispersive mechanisms.[3,4] Shown in Fig. 1 are the time-frequency features of some common mechanisms. A discrete event of time, for example, could be due to wave scattering from a spatially localized "scattering center" on a structure. It shows up as a vertical line (Fig. 1(a)) in the image since it occurs at a particular time instance but over all frequencies. A resonance, which is a discrete event of frequency, shows up as a horizontal line (Fig. 1(b)). Dispersive phenomena, on the other hand, are characterized by slanted curves in the time-frequency image. For example, surface wave mechanisms due to material coatings are characterized by curves with a positive slope in the time-frequency image (Fig. 1(c)). As the frequency is increased, the surface wave becomes more tightly bound to the material layer, and consequently, propagates at a slower velocity and results in a longer time delay. Another type of dispersion is due to waveguide structures. These "structural dispersion" mechanisms are characterized by curves with

a negative slope in the time-frequency image (Fig. 1(d)). This can be explained by the fact that as the frequency is lowered, one approaches the cutoff frequency of a waveguide mode and the propagation delay associated with this mechanism approaches infinity. As we shall see in this paper, all of the above mentioned phenomena have been observed in a wide variety of structures, from simulation data on canonical structures to measurement data on complex platforms. For radar applications, for instance, the time-frequency representation is particularly effective for identifying scattering mechanisms in targets containing "sub-skinline" structures such as inlet ducts, antenna windows and material coatings.

2. JOINT TIME-FREQUENCY ALGORITHMS AND SCATTERING PHENOMENOLOGY

The insights gained in the time-frequency plane come at the price of resolution. As we have already discussed, the time-frequency image generated by the STFT is limited in resolution by the extent of the sliding window function. Smaller time window results in better time resolution, but leads to worse frequency resolution, and vice versa. To overcome the resolution limit of the STFT, a wealth of alternative time-frequency representations have been developed in the signal processing community. Below, we shall introduce four classes of algorithms which have been utilized to analyze electromagnetic data, namely, continuous wavelet transform, Wigner-Ville distribution, windowed superresolution algorithms and adaptive techniques. While this list is by no means complete, these four classes of algorithms provide a flavor of the different approaches to the resolution issue.

2.1 Continuous Wavelet Transform. Contrary to the fixed resolution of the STFT, the wavelet transform can be defined to achieve variable resolution in one domain (either time or frequency) and multi-resolution in the other domain. We will now introduce the continuous wavelet transform (CWT), or the so-called scalogram, of a frequency signal $F(\omega)$:

$$CWT\ (\tau,\Omega) = \frac{1}{2\pi}\int F(\omega)\ \tau^{1/2}\ H(\tau\ (\omega-\Omega)\ )\ \ d\omega \qquad (4)$$

$H(\omega)$ is usually termed the "mother wavelet" in wavelet theory. Essentially, (4) can be interpreted as a decomposition of the frequency signal $F(\omega)$ into a family of shifted and dilated wavelets $H(\tau(\omega-\Omega))$. The wavelet basis function $H(\tau(\omega-\Omega))$ has variable width according to τ at each frequency Ω. $H(\tau(\omega-\Omega))$ is wide for small τ and narrow for large τ. By shifting $H(\omega)$ with a fixed scale parameter τ, the $1/\tau$-scale mechanisms in the frequency response $F(\omega)$ can be extracted and localized. Alternatively, by dilating $H(\omega)$ at a fixed Ω, all of the multi-scale events of $F(\omega)$ at Ω can be analyzed according to the scale parameter τ. This is the so-called "multi-resolution" property of the wavelet transform and is an advantage over the STFT for analyzing multi-scale signals. Like the STFT, the wavelet transform can also be carried out on the inverse Fourier transform $f(t)$ of the original frequency signal $F(\omega)$:

$$CWT\ (\tau,\Omega) = \int f(t)\ \tau^{-1/2}\ h\ (-t\ /\ \tau)\ e^{-j\Omega t}\ \ dt \qquad (5)$$

where $h(t)$ is the Fourier transform of $H(\omega)$. Since (4) is essentially the Fourier transform of $[f(t)\tau^{-1/2}h(-t/\tau)]$, it is the preferred numerical implementation of the wavelet transform through the use of the fast Fourier transform algorithm for each value of τ. By comparing Equations (2) and (5), we note that $h(t)$ is similar to the window function in the STFT. However, $h(t)$ must satisfy the "admissibility condition" in wavelet theory, viz., $h(t=0) = 0$. To satisfy this condition, $h(t)$ is usually chosen to be a shifted window function with its center at t_0. By changing τ, this window function is shifted by τt_0 and the width of the window is dilated by the scale factor τ. The ratio between the window width and the window center (or the Q-factor of the window function) remains fixed for all times. This is in contrast to the STFT where the window width does not change as it is being shifted.

It is worthwhile to point out here that the definition of the wavelet transform presented above in its time and frequency forms is exactly the complement of its usual definition used in time-series signal analysis. For electromagnetic applications, it has been found that the property of the wavelet transform we are usually interested in is its multi-resolution capability in the frequency domain and its variable resolution capability in the time domain. The multi-resolution capability is ideally suited for analyzing frequency-domain electromagnetic data which consist of both discrete time events (of large extent in frequency) and discrete frequency events (of small extent in frequency).

As an example, the time-frequency representation of the backscattering data from an open-ended waveguide duct is considered.[5] The duct is an open-ended circular waveguide with a diameter of 1.75 in. A flat conducting termination exists 2 ft. inside the waveguide (Fig. 2(a)). To generate the backscattering data, the radar cross section of this target is first computed in the frequency domain. The time-domain response is then obtained by Fourier transforming the band-limited

frequency data (from 2 to 18 GHz). Fig. 2(b) shows the spectrogram of the backscattering data for the H-polarization at 45° off-normal incidence using the STFT. In performing the STFT, a 2-GHz Kaiser-Bessel window in the frequency domain is used. Also plotted along the two axes are the time-domain and the frequency-domain responses. It is apparent that the scattering features are much better resolved in the time-frequency domain than in either the time or the frequency domain alone. Both the non-dispersive rim diffraction and the mode spectra due to multiple propagating modes in the circular waveguide can be clearly identified. The mode spectra are in fact dispersion curves of the waveguide modes since the phase velocity of each mode is proportional to the travel time.
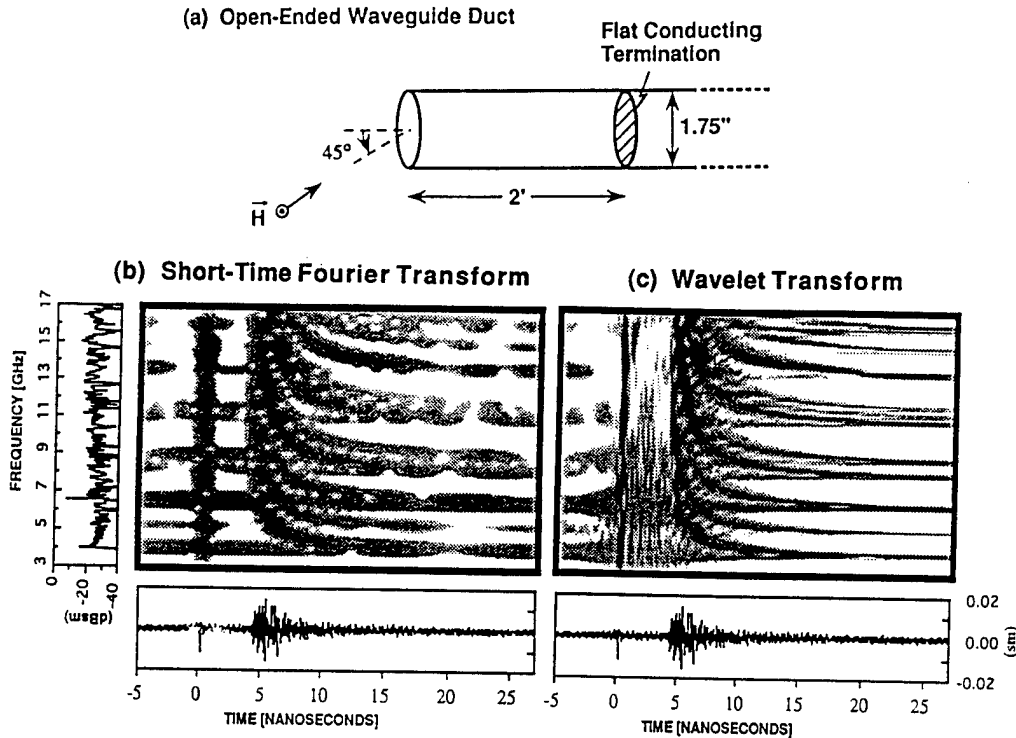

Fig. 2. Joint time-frequency images of the backscattered data from an open-ended waveguide duct obtained via STFT and continuous wavelet transform.

Due to the fixed resolution of the STFT, the scattering features in Fig. 2(a) are smeared out in the time-frequency plane. This problem is overcome by using the wavelet transform which provides a much better representation of the scattering features in the time-frequency plane, as shown in Fig. 2(c). The wavelet transform is implemented using (5) with the aid of the FFT. The function h(t) is chosen to be a two-sided Kaiser-Bessel window with a Q-factor of 0.3. The t=0 reference of h(t) is located midway between the time events from the rim diffraction and interior contribution (at τ=2.05 ns). The variable time resolution of the wavelet transform allows sharper time resolution to be achieved during the early-time response and sharper frequency resolution (coarser time resolution) to be achieved during the late-time response. Thus, wavelet transform provides good resolution in identifying the scattering centers and resolving the resonant phenomena of the target while adequately describing the dispersive scattering mechanisms in the intermediate-time region.

2.2 Wigner-Ville Distribution and Time-Frequency Distribution Series. While the STFT and the wavelet transform are based on linear transformations, another class of time-frequency distributions can be obtained from the quadratic, or power spectrum, point of view. The most basic of these is called the Wigner-Ville distribution (WVD), first developed in quantum mechanics. The WVD of a signal f(t) is defined as:

$$WVD\,(\tau,\Omega) = \int f(\tau + \frac{t}{2})\; f^*(\tau - \frac{t}{2})\; e^{-j\Omega t}\; dt \tag{6}$$

The WVD distribution is always real and gives information on how the power spectrum of the signal changes as a function of time. Although the WVD gives nearly the best resolution among all the time-frequency techniques, its main drawback comes from cross-term interference problem. Simply put, the WVD of the sum of two signals is not the sum of their

WVD's. Therefore, if a signal contains more than one component in the joint time-frequency plane, its WVD will contain cross terms which occur halfway between each pair of the auto terms. The magnitude of these oscillatory cross terms can be twice as large as the auto terms and yet they do not have any physical meaning. This drawback severely limits the usefulness of the WVD in its original form. A number of techniques can be used to alleviate this problem. We shall introduce one recently proposed by Qian and Chen.[6] They suggested that if the WVD can be decomposed into a sum of localized and symmetric functions, it may be possible to suppress cross-term interference by selecting only the low order harmonics. This is accomplished by first decomposing the original signal into the Gabor expansion:

$$f(t) = \sum_m \sum_n C_{m,n} \, h_{m,n}(t) \tag{7}$$

where

$$h_{m,n}(t) = (\pi\sigma^2)^{-0.25} \exp\left\{ \frac{(t - mT)^2}{2\sigma^2} + jn\Lambda t \right\} \tag{8}$$

are time-shifted and frequency-modulated Gaussian basis functions. In the above expression, m and T are respectively the time sampling index and time sampling interval, while n and Λ are the sampling index and sampling interval in frequency. By taking the WVD of both sides of (7), it becomes:

$$WVD\,(\tau,\Omega) = \sum_{mn} \sum_{m'n'} C_{m,n} \, C^*_{m',n'} \, WVD_{h,h'}(\tau,\Omega) \tag{9}$$

where $WVD_{h,h'}$ denotes the WVD between any pair of basis functions and is available in closed form. Next, the above expression can be regrouped based on the "interaction distance"

$$D = |\, m - m'\,| + |\, n - n'\,| \tag{10}$$

between the pairs of bases (m, n) and (m', n'). This results in what is termed the "time-frequency distribution series" (TFDS, also called the Gabor spectrogram):

$$WVD\,(\tau,\Omega) \quad = \sum_{mn} |\, C_{m,n} \,|^2 \, WVD_{h,h'}(\tau,\Omega) \qquad (D=0 \text{ terms}) \tag{11}$$

$$+ \sum_{mn} \sum_{m'n'} C_{m,n} \, C^*_{m',n'} \, WVD_{h,h'}(\tau,\Omega) \qquad (D=1 \text{ terms})$$

$$+ \sum_{mn} \sum_{m'n'} C_{m,n} \, C^*_{m',n'} \, WVD_{h,h'}(\tau,\Omega) \qquad (D=2 \text{ terms})$$

$$+ \ldots \ldots$$

Clearly, if we take all the terms in the series (D=∞), the right hand side of (11) converges to the WVD of the original signal. This yields the best resolution but is plagued by cross-term interference. At the other extreme, if we take only the self-interaction terms in the series (D=0), the resulting right-hand side is equivalent to the STFT of the signal using a Gaussian window function. It has no cross-term interference problem but has the worst resolution. Therefore, as the order D increases, we gain in resolution but pay a price in cross-term interference. It is often possible to balance the resolution against cross-term interference by adjusting the order D. The optimal value for D was reported to be around 2 to 4.

As an example, we consider the scattering from a dielectric coated wire. The coated wire is a 12" section of a coaxial cable (RG-41/U with a=0.037" and b=0.095") with its outer conductor removed. The dielectric material is Teflon

with permittivity $\varepsilon_r = 2.1$. The scattering data are collected by both numerical simulation and by chamber measurement. The spectrograms for the case of 60° incidence from broadside is shown in Fig. 3(a). we observe a slight tilting of the vertical lines in the spectrograms, especially in the late-time returns. This signifies the presence of dispersive phenomena which are due to the surface wave mechanism in the dielectric coating known as the Goubau mode. At frequencies well above DC, this mode is tightly bound to the dielectric and the group velocity of the wave approaches the slow dielectric velocity. As the frequency approaches DC, the wave velocity approaches that of free space and exhibits a shorter propagation delay. Therefore, in the time-frequency plane, the Goubau mode phenomena show up as slanted curves with a positive slope. The TFDS and the WVD results are also given in Figs. 3(b) and 3(c), respectively. As we can see from Figs. 3(c), the WVD of the data is so contaminated by cross-term interference it is essentially useless. The TFDS results shown in Fig. 3(b) is a good compromise between resolution and cross-term interference. The returns that can not be distinguished from each other in the spectrogram are now easily identified in the joint time-frequency plane by using the TFDS of order 2.

Conductor Radius: 0.037"

Dielectric Wire Radius: 0.095"

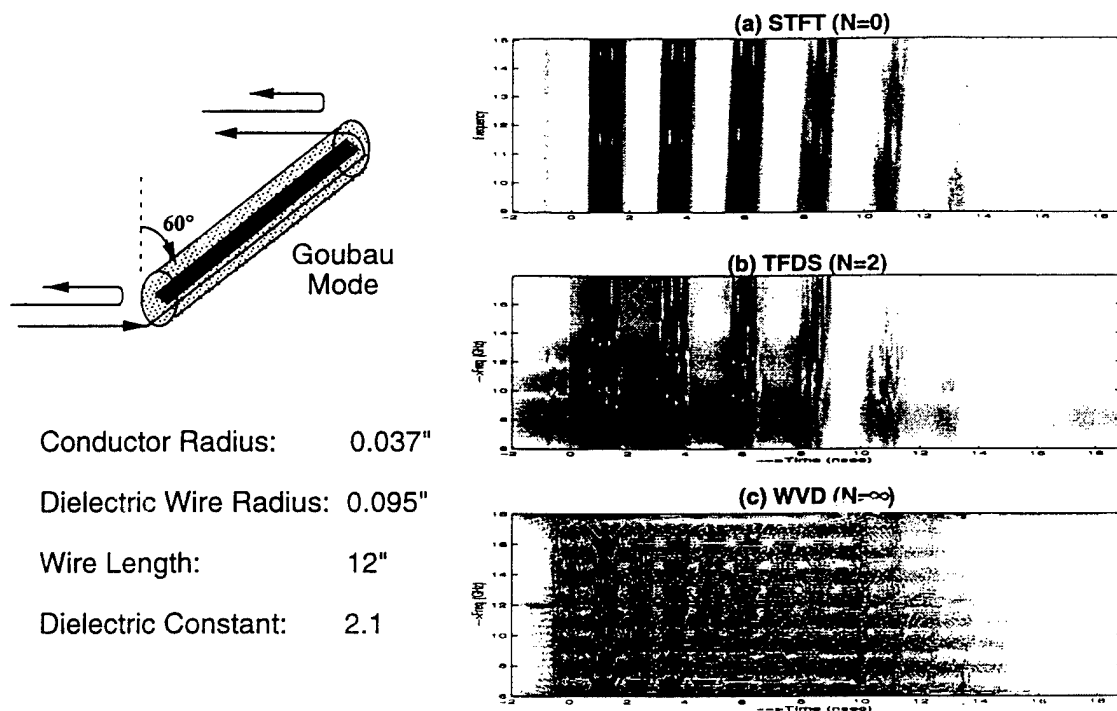Wire Length: 12"

Dielectric Constant: 2.1

Fig. 3. Joint time-frequency representations of the backscattered data from a dielectric-coated wire obtained via STFT, time-frequency distribution series with N=2, and Wigner-Ville distribution.

2.3 Windowed Superresolution Algorithms. In either the STFT or the wavelet transform, the resolution in the time-frequency display is limited by the extent of the sliding window function as opposed to the full bandwidth of the signal. The processing of the data within each time or frequency window using a super-resolution technique such as ESPRIT, MUSIC or matrix-pencil algorithm therefore appears quite attractive.[8,9] Super-resolved parameterization retains the advantage of simultaneous time-frequency display while overcoming the resolution issue. However, additional processing is needed to fully parameterize the data, especially when dispersive mechanisms are present. Furthermore, the robustness of the algorithms to noise needs to be carefully considered. We will describe a simple windowed superresolution procedure based on Prony's method for achieving parameter estimation of both scattering centers and natural resonances in the time-frequency plane.

In the windowed time-frequency super-resolution procedure, Prony's extraction is first applied in the frequency domain to locate discrete time events. Prony's method will fit the raw data to the following model:

$$F(\omega) = \sum_{m=1}^{M} A_m e^{-j\omega t_m} \tag{12}$$

where the t_m's are the unknown locations of the discrete time events, the A_m's are the unknown complex strengths of these events, and M is the number of them to be found. It is clear that applying Prony's method to the entire frequency data will

yield a poor fit if the raw data contains discrete frequency events such as resonances. To circumvent this problem, we repeated apply Prony's method to many small windows of the raw data. Prony's method will be successful for most of the window locations and will fail only when a window coincides with a resonant peak. By repeatedly sliding the window along in frequency and re-applying Prony's method to the raw data, we are able to identify as true locations those values of t_m which most frequently occur. A weighted least squares fit of the values of A_m for each discrete time event is used to construct a smooth functional form of A_m. An important benefit of this global functional form, $A_m(\omega)$, is that it allows us to go back and interpolate A_m at those frequencies where Prony's method originally failed.

Provided that the discrete time events have been properly located and accounted for, the remaining data will consist solely of a series of resonant peaks after the frequency domain extraction. To extract the natural resonance information, this remaining data is inverse Fourier transformed to the time domain. The sliding window Prony's procedure is then applied in the time domain to fit the complex-valued data to a model which is the dual of (12):

$$f(t) = \sum_{n=1}^{N} B_n \, e^{-j\omega_n t} \tag{13}$$

in which the ω_n's are the unknown resonance frequencies, and the B_n's are their corresponding strengths. By tracking the behavior of each B_n with respect to time, other parameters associated with the resonance, such as attenuation factor (α_n) and turn-on time (τ_n) are extracted:

$$f(t) = \sum_{n=1}^{N} b_n \, e^{+j\omega_n(t-\tau_n)} \, e^{-\alpha_n(t-\tau_n)} \, u(t-\tau_n) \tag{14}$$

in which the b_n's are strengths of the resonances at turn-on and $u(t-\tau_n)$ is the unit step function.
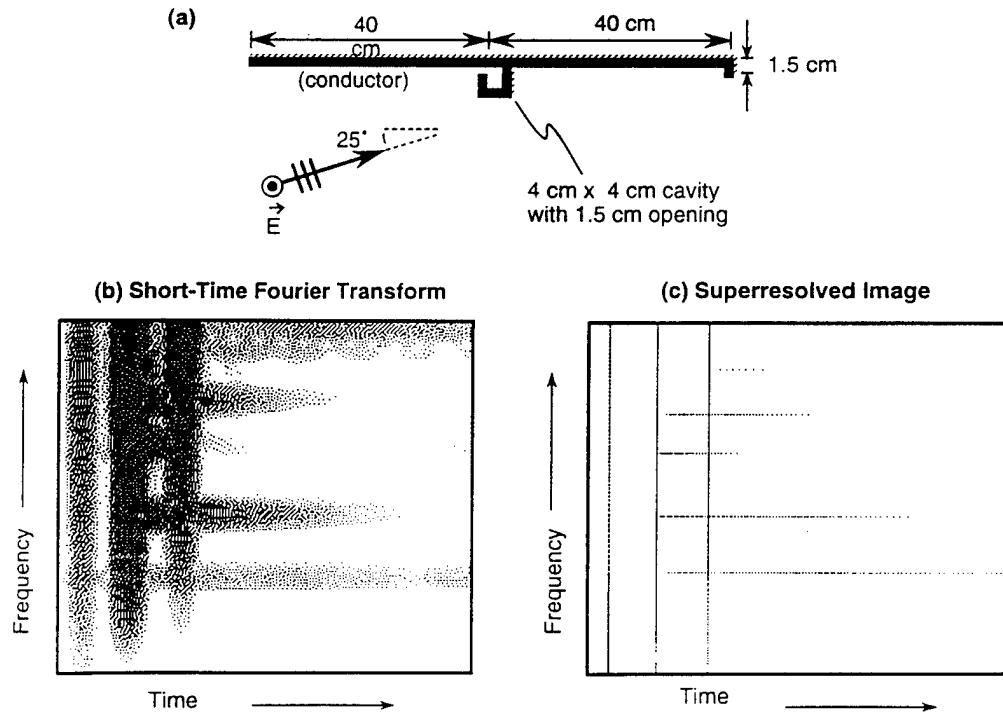

Fig. 4. Time-frequency images of the backscattered data from a conducting strip with an open cavity obtained via STFT and windowed superresolution algorithm.

As an example, let us consider a perfectly conducting strip containing a small open cavity located in the middle of the strip shown in Fig. 4(a). Backscattering data from 50 MHz to 18 GHz were simulated using a method of moments solution for the E-polarized incidence at 25° from edge-on. Shown in Fig. 4(b) is the spectrogram of the scattered data obtained via the STFT with a 1-GHz frequency window. The three vertical lines correspond to the scattering centers from the left edge, the cavity exterior and the right fin, and the five visible horizontal lines correspond to the cavity resonances. It is possible to extract qualitative information such as the approximate frequency behaviors of the individual scattering centers and the resonance Q's from the STFT image. However, due to the large number of features contained in the backscattered data, the image is blurry, making it difficult to resolve fine details. Fig. 4(c) shows a time-frequency plot of the parameterized backscattered data. Because we have completely parameterized the data via a super-resolution technique, the sharpness of the image is not constrained by the well-known Fourier limit as is the case for the STFT image. Our image can be of nearly infinite sharpness, so we have chosen for each mechanism to appear as either a horizontal or vertical line exactly one pixel in width. The intensities of the three vertical lines show that the three scattering centers are of differing strengths and have different frequency behaviors. The high-Q resonances can be seen to be of much longer duration than the low-Q resonances.

2.4 Adaptive Gaussian Representation. While the use of wavelet is a step towards variable resolution in the time-frequency plane, it is rather rigid in its particular form of the time-frequency grid. Flexible resolution in the time-frequency plane to accommodate components of the signal with different resolution is therefore highly desirable. Recently, a signal representation scheme that uses adaptive normalized Gaussian functions was introduced.[10] (A similar algorithm called matching pursuit was developed independently at around the same time by Mallat and Zhang[11]). Unlike the STFT and wavelet decomposition, the time and frequency resolution as well as the time-frequency centers are adjusted to best match the signal. The objective of this method is to expand a signal $f(t)$ in terms of normalized Gaussian functions $h_p(t)$ with an adjustable standard deviation σ_p and a time-frequency center (t_p, f_p):

$$f(t) = \sum_{p=1}^{\infty} B_p \, h_p(t) \tag{15}$$

where

$$h_p(t) = (\pi \sigma_p^2)^{-0.25} \exp\left[-\frac{(t-t_p)^2}{2\sigma_p^2}\right] \exp(j \, 2\pi f_p t) \tag{16}$$

Note that the modulated Gaussian basis has a dual form in its Fourier transform representation:

$$H_p(f) = \left[\pi (1/2\pi\sigma_p)^2\right]^{-0.25} \exp\left[-\frac{(f-f_p)^2}{2(1/2\pi\sigma_p)^2}\right] \exp(-j \, 2\pi(f-f_p) t_p) \tag{17}$$

Therefore, these basis functions have a time-frequency extent given by, respectively, σ_p and $(1/2\pi\sigma_p)$. The coefficients B_p are found one at a time by an iterative procedure. One begins at the stage $p=1$ and chooses the parameters σ_p, t_p and f_p such that $h_p(t)$ is most "similar" to $f(t)$, that is:

$$|B_p|^2 = \max_{\sigma_p, t_p, f_p} \left| \int f_{p-1}(t) \, h_p^*(t) \, dt \right|^2 \tag{18}$$

where $f_0(t) = f(t)$. For $p > 1$, $f_p(t)$ is the remainder after the orthogonal projection of $f_{p-1}(t)$ onto $h_p(t)$ has been removed from the signal:

$$f_p(t) = f_{p-1}(t) - B_p(t) h_p(t) \tag{19}$$

This procedure is iterated to generate as many coefficients as needed to accurately represent the original signal.

Several comments can be made about the adaptive Gaussian representation. First, it can be shown that the norm of the residue monotonically decreases and converges to zero, therefore adding a new term in the series does not affect the previously selected parameters. Second, because this representation is adaptive, it will generally be concentrated in a very small subspace. As a result, we can use a finite summation of the terms in (15) to approximate the signal, with a residual error as small as one wishes. Also, since random noise in general is distributed uniformly in the entire space, this subspace representation actually increases the signal-to-noise ratio. Finally, the major difficulty in implementing this algorithm is the determination of the optimal elementary function at each stage. One implementation strategy is to start with a large σ_p and scan the data in frequency and time for a peak. Then we divide σ_p by two and find the new peak. We continue this procedure until the standard deviation is small enough and then select the highest peak and extract the residual using (19). It should be pointed out that the fast Fourier transform is used during the search procedure to obtain the coefficients for all the frequency centers at once, speeding up the search that would otherwise be very time consuming.

The result of applying the adaptive Gaussian extraction can be effectively displayed in the time-frequency plane using the so-called adaptive spectrogram (ADS):

$$ADS\,(t,\,f)\ =\ 2\ \sum_p\ \left|B_p\right|^2\ \exp\!\left[-\ \frac{(t-t_p)^2}{\sigma_p^2}\ -\ (2\pi)^2\,\sigma_p^2\,(f-f_p)^2\ \right] \tag{20}$$

This representation was obtained by calculating the Wigner-Ville distribution of (15) and then deleting the cross terms. It can be shown that the energy contained in the ADS is identical to the energy contained in the signal. So it can be considered as a signal energy distribution in the time-frequency domain. It is also non-negative, cross-term interference free, and of high resolution.
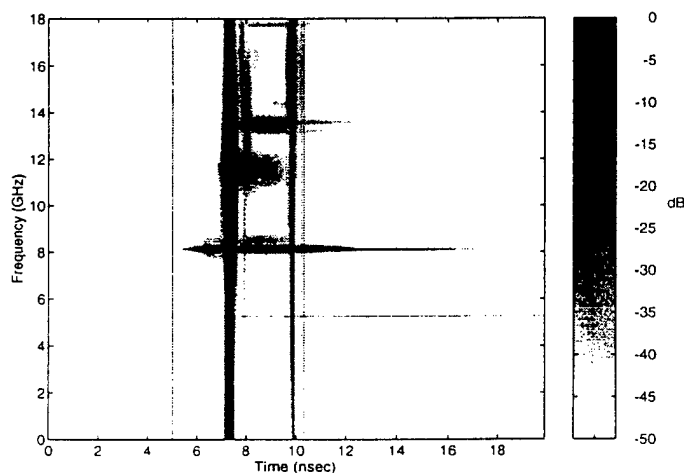

Fig. 5. Adaptive spectrogram of the backscattered data from a conducting strip
with an open cavity (see Fig. 4(a)).

To show an example of the adaptive spectrogram, we used the same structure used in Fig. 4(a). We applied the algorithm described above and obtained an approximation of the signal using 50 terms in expression (1) with a residual energy of 0.1%. The ADS obtained is shown in Fig. 5. We can clearly see and locate with high resolution the three scattering centers and the resonances. We notice that the high-Q resonances appear as very thin horizontal lines, while the low-Q resonances appear as thicker lines as expected. We can even see that the second and the third scattering center corresponding respectively to the cavity exterior and the right fin are in reality multiple scattering centers.

3. AN APPLICATION - RADAR IMAGE ENHANCEMENT AND FEATURE EXTRACTION

We will now describe an applications of joint time-frequency processing to electromagnetic backscattered data in the area of radar imaging.[12] Inverse synthetic aperture radar (ISAR) imaging has long been used by the microwave radar community for object diagnostic and target identification applications. ISAR is a simple and very robust process for mapping the position

and magnitude of the point scatterers on an object from multi-frequency, multi-aspect scattered field data. However, complex targets often contain other scattering phenomena such as resonances and dispersive mechanisms, which do not behave like point scatterers. One important example is the scattering from the engine inlet/exhaust duct on aircraft. It is a dominant contributor to the overall scattering from the target, yet its waveguide-like structure and the associated frequency-dependent scattering mechanisms make it a non-point scattering feature. When processed and displayed by the conventional ISAR algorithm, the inlet return results in an image feature which (i) is not well-focused, (ii) is not related to the spatial location of the scatterer, and (iii) can often obscure other important point features on the target. Therefore, it would be useful to develop an algorithm to automatically remove these features from the ISAR image, thus leading to a cleaned ISAR image containing only physically meaningful point scatterers. The extracted inlet features, when displayed in a more meaningful feature space, can be used to identify target resonances and cutoff phenomena.

In this section, we present a new processing technique, the joint time-frequency ISAR, that combines the idea of standard ISAR with the joint time-frequency technique to accomplish the above objective. The conceptual idea behind the joint time-frequency ISAR algorithm is to apply joint time-frequency processing to the range (or time) axis of the conventional (range)-(cross range) ISAR image to gain an additional frequency dimension. The result is a three-dimensional (range)-(cross range)-(frequency) matrix, with each (range)-(cross range) slice of this matrix representing an ISAR image at a particular frequency. Consequently, by examining how the ISAR image varies with frequency, we can distinguish the frequency-independent scattering mechanisms from the frequency-dependent ones. In the actual implementation of the joint time-frequency ISAR, the choice of the joint time-frequency processing engine is critical. Our choice is the adaptive spectrogram described in Section 2.4.
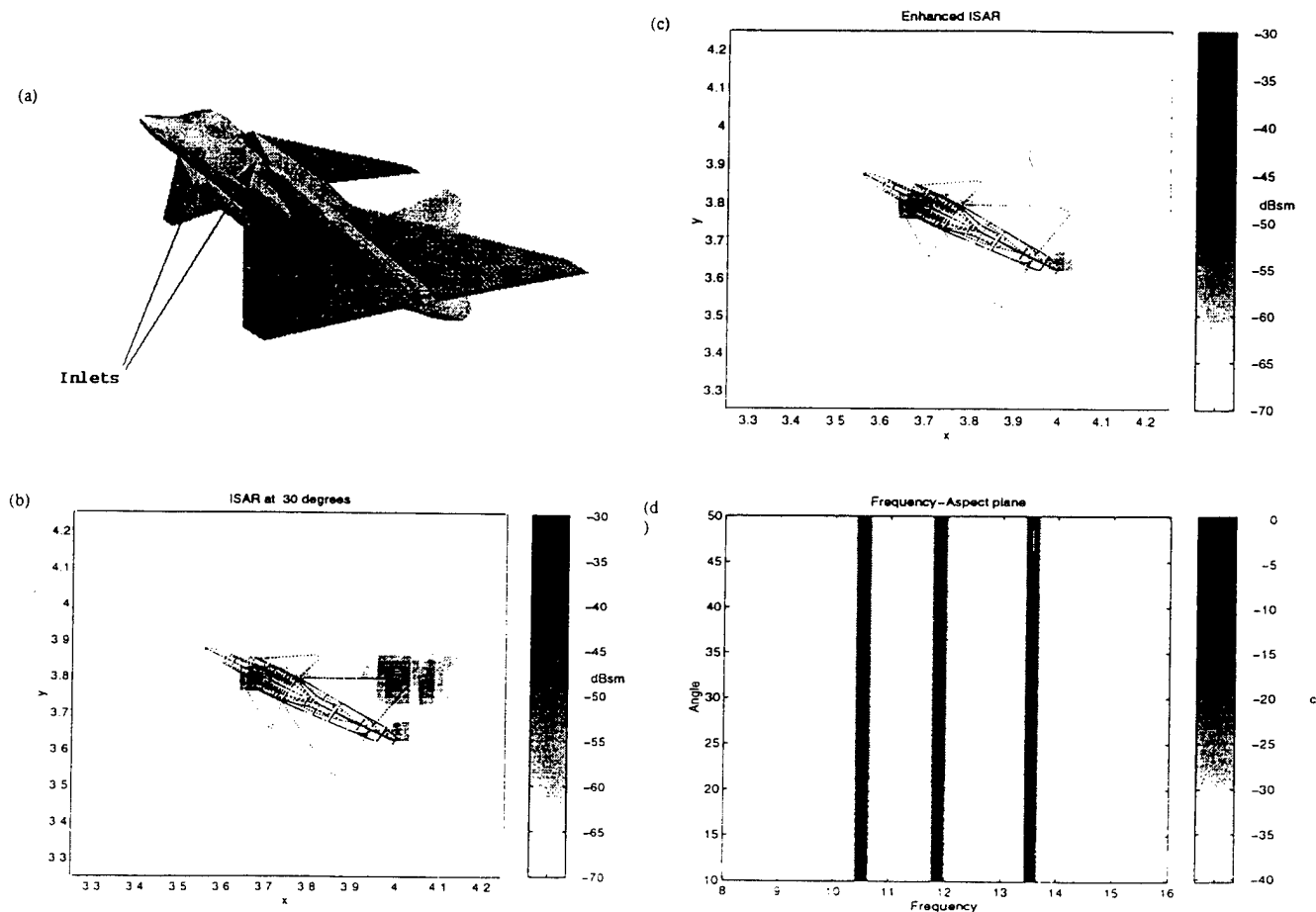

Fig. 6. (a) The VFY-218 model. (b) Its standard ISAR image obtained for f = 8-16 GHz and a 40-degree angular window centered at 30 degrees from nose-on. (c) Enhanced ISAR image and frequency-aspect display obtained by applying the Adaptive Gaussian Representation to the ISAR image in Fig. 6(b). The inlet cloud has been removed in the original ISAR image. (d) The extracted resonant features of the inlet are shown in the frequency-aspect plane.

The adaptive spectrogram has two distinct advantages over conventional time-frequency techniques such as the short-time Fourier transform. First, it is a parameterization procedure that results in very high time-frequency resolution. More importantly for our application, the adaptive spectrogram allows us to automatically distinguish the frequency-dependent events from the frequency-independent ones through the extent of the basis functions. From expression (16) it can be seen that scattering centers, i.e., signals with very narrow length in time, will be well represented by basis functions with very small σ_p. Frequency resonances, on the other hand, will be better depicted by large σ_p. Therefore, if we reconstruct the ISAR image using only those Gaussian bases with small variances, a much cleaner image can be obtained showing only the scattering centers. The remaining mechanisms, i.e., those related to the large variance Gaussians, are more meaningful to view in a dual frequency-aspect display, where resonances and other frequency-dependent mechanisms can be better identified.

The algorithm is demonstrated using the chamber measurement data of a 1:30 scale model Lockheed VFY-218 airplane provided by the EMCC (Electromagnetic Code Consortium).[12] The airplane has two long engine inlet ducts, as show in Fig. 6(a), which are rectangular at the open ends but merge together into one circular section before reaching a single-compressor face. As we can clearly see in the conventional ISAR image of Fig. 6(b) for the vertical polarization at 20° near nose-on, the large cloud outside of the airframe structure is the inlet return. Fig. 6(c) shows the enhanced ISAR image of Fig. 6(b), obtained by applying the above joint time-frequency ISAR algorithm and keeping only the small variance Gaussians. We see that only the scattering center part of the original signal remains in the image, as expected. Notice that the strong return due to engine inlet has been removed, but the scattering from the tail fin remains. Fig. 6(d) shows the frequency-aspect display of the high variance Gaussians. A number of equispaced vertical lines can be seen between 10.5 and 13.5 GHz. Given the dimension of the rectangular inlet opening, we estimate that these frequencies correspond approximately to the second cutoff frequency of the waveguide-like inlet. We have also run our algorithm on the simulated scattering data, generated using a numerical Maxwell's solver, for a plate-waveguide configuration to verify this claim. The frequency resonances displayed indeed correspond very closely to the theoretical cutoff frequencies of the waveguide.

In this section we presented a joint time-frequency ISAR algorithm to process data from complex targets containing not only scattering centers but also other frequency-dependent scattering mechanisms. The adaptive joint time-frequency ISAR algorithm allows the enhancement of the ISAR image by eliminating non-point scatterer signals, thus leading to a much cleaner ISAR image. It also provides information on the extracted frequency-dependent mechanisms such as resonances and frequency dispersions. This is accomplished without any loss in resolution.

ACKNOWLEDGMENTS

REFERENCES

1. L. Cohen, *Time-Frequency Analysis*, Prentice Hall, Englewood Cliffs, NJ, 1995.

2. S. Qian and D. Chen, *Introduction to Joint Time-Frequency Analysis - Methods and Applications*. Prentice Hall, Englewood Cliffs, NJ, 1996.

3. K. F. Casey, D. G. Dudley and M. R. Portnoff, "Radiation and dispersion effects from frequency-modulated (FM) sources," *Electromagnetics*, vol. 10, pp. 349-376, 1990.

4. A. Moghaddar and E. K. Walton, "Time-frequency-distribution analysis of scattering from waveguide cavities," *IEEE Trans. Antennas Propagat.*, vol. AP-41, pp. 677-680, May 1993.

5. H. Kim and H. Ling, "Wavelet analysis of radar echo from finite-size targets," *IEEE Trans. Antennas Propagat.*, vol. AP-41, pp. 200-207, Feb. 1993.

6. S. Qian, and D. Chen, "Decomposition of the Wigner-Ville distribution and time-frequency distribution series," *IEEE Trans. Signal Processing*, vol. 42, pp. 2836-2842, Oct. 1994.

7. C. Ozdemir and H. Ling, "Interpretation of scattering phenomenology in dielectric-coated wires via joint time-frequency processing," *IEEE Trans. Antennas Propagat.*, vol. AP-45, pp. 1259-1264, Aug. 1997.

8. L. Carin, L.B. Felsen, D. R. Kralj, H. S. Oh, W. C. Lee and S. U. Pillai, "Wave-oriented signal processing of dispersive time-domain scattering data," *IEEE Trans. Antennas Propagat.*, vol. AP-45, pp. 592-600, Apr. 1997.

9. J. Moore and H. Ling, "Super-resolved time-frequency analysis of wideband backscattered data," *IEEE Trans. Antennas Propagat.*, vol. AP-43, pp. 623-626, June 1995.

10. S. Qian and D. Chen, "Signal representation using adaptive normalized Gaussian functions," *Signal Processing*, vol. 36, no. 1, pp. 1-11, Mar. 1994.

11. S. G. Mallat and Z. Zhang, "Matching pursuits with time-frequency dictionaries," *IEEE Trans. Signal Processing*, vol. 41, pp. 3397-3415, Dec. 1993.

12. L. C. Trintinalia and H. Ling, "Joint time-frequency ISAR using adaptive processing," *IEEE Trans. Antennas Propagat.*, vol. AP-45, pp. 221-227, Feb. 1997.

13. H. T. G. Wang, M. L. Sanders and A. Woo, "Radar cross section measurement data of the VFY 218 configuration," Tech. Rept. NAWCWPNS TM-7621, Naval Air Warfare Center, China Lake, CA, Jan. 1994.

Application of adaptive joint time-frequency processing to ISAR image enhancement and Doppler feature extraction for targets with rotating parts

Y. Wang[a], H. Ling[a] and V. C. Chen[b]

[a]Department of Electrical and Computer Engineering,
The University of Texas at Austin, Austin, TX 78712-1084

[b]Airborne Branch, Naval Research Laboratory
Washington, DC 20375

ABSTRACT

A new methodology based on adaptive joint time-frequency processing is proposed to separate the interference due to fast rotating parts from the original ISAR image of the target. The technique entails adaptively searching for the linear chirp bases which best represent the time-frequency behavior of the signal and fully parameterizing the signal with these basis functions. The signal components due to the fast rotating part are considered to be associated with those chirp bases having large displacement and slope parameters, while the signal components due to the target body motion are represented by those chirp bases having relatively small displacement and slope parameters. By sorting these chirp bases according to their slopes and displacements, the scattering due to the fast rotating part can be separated from that due to the target body. Consequently, the image artifacts overlapping with the original image of the target can be removed and a clean ISAR image can be produced. Furthermore, useful rotation rate information contained in the Doppler signal can be extracted. Successful applications of the algorithm to numerically simulated and measurement data show the robustness of the algorithm.

Keywords: ISAR imaging, Doppler smearing, fast rotating parts, adaptive joint time-frequency processing

1. INTRODUCTION

It is well known that when rotating components exist on a target such as gimbaled antennas or propeller blades, image artifacts are introduced in the Doppler dimension of the inverse synthetic aperture radar (ISAR) image[1, 2, 3]. The reason is that those parts are often rotating at a speed much faster than the target itself and the Doppler frequencies generated by them are much higher than the radar pulse repetition rate. Therefore serious aliasing can result in smearing through all the cross range dimension of the image. These smeared features oftentimes overshadow the target geometrical features and hinder the proper interpretation of the ISAR image. To enhance such an image, the most often used approach is to simply estimate the size of the target in the cross range dimension, keep the signal components inside the target dimension and discard all the other unwanted components outside the confined region. This approach can remove most of the Doppler smearing if the actual size of the target is known. However, in most of the real world ISAR applications, the target is unknown and it is difficult to give a close estimation of the target size. An over estimation of the target size must be used to assure that most of the target features are kept in the image, thus resulting in poor elimination of the Doppler smearing. Furthermore, even if the size of the target is accurately known, those Doppler smearing overlapping with the target features can never be eliminated by this gating technique, since they are within the geometrical dimension of the target.

Instead of treating the Doppler signal induced by the rotating parts as noise in the image, it can also be considered as a type of radar signature, since it includes some unique information of the target. For example, jet engine modulation (JEM) of radar return has already been used for target identification purposes [4]. In reference 4, the autocorrelation sequence of the time domain signal has been used for period detection of engine blades. However, we found that when the target body return is strong and overlaps with the rotating part return in the Doppler frequency spectrum, the period detection algorithm is no

longer robust, due to the interference caused by the target body. Therefore, to separate the radar return induced by the rotating parts from that induced by the target body, a new technique is proposed here based on the adaptive joint time-frequency (AJTF) processing. It shall be shown that two different signal components can be well separated via this approach, from which we are able to produce a clear ISAR image of the target and at the same time achieve robust Doppler information extraction.

The original concept of adaptive joint time-frequency processing was proposed in the signal processing community [5, 6]. It has been applied to ISAR image processing in the joint time-frequency space for resonant scattering mechanism extraction [7, 8] and target motion compensation [9, 10]. Compared to the standard processing techniques in either the time or the frequency domain, more insights into the underlying physical mechanisms can be gained in the joint time-frequency plane since the instantaneous frequency behaviors of the signal are available. Our approach in the present application entails adaptively searching for the linear chirp bases which best represent the time-frequency behavior of the signal. This is accomplished by projecting the signal onto all possible chirp bases and finding the one with the maximum projection value. After the optimal basis is found, the signal component associated with this basis is subtracted from the original signal. By iterating this search procedure, the signal can be fully parameterized with a set of chirp basis functions. Since the Doppler frequency due to the rotating component is both higher and more rapidly varying (in dwell time) than that from the target body, the signal components due to the fast rotating part are assumed to be associated with those chirp bases having large displacement and slope parameters. On the other hand, those chirp bases which have relatively small displacement and slope parameters are assumed to represent the signal components due to the target body motion. By sorting these chirp bases according to their slopes and displacements, the scattering due to the fast rotating part can be separated from that due to the target body. Consequently a cleaned ISAR image of the target body can be reconstructed by using only those bases associated with the body motion, while robust Doppler information extraction can be achieved by applying the period detection algorithm to the component associated with rotating parts only. We shall present the results of applying this algorithm to both simulated data from the radar scattering prediction code Xpatch and some real measurement results.

2. ADAPTIVE JOINT TIME-FREQUENCY PROCESSING

ISAR imaging is a simple and robust process for mapping the position and magnitude of the target scattering features based on a point-scatterer assumption of the target. With this assumption, the target consists of a group of point scatterers. Therefore the radar scattering signal collected versus frequency and observation angle can be described as:

$$E(f,\theta) = \sum_{i=1}^{N} O(x_i, y_i) e^{-2jkx_i \cos\theta - 2jky_i \sin\theta} \tag{1}$$

where $O(x_i, y_i)$ is the amplitude of the ith scattering center, k is the free space wave number. In real radar measurements for targets in flight, the look angle is usually unknown but scales according to the observation dwell time. If the target is rotating at a constant rate with respect to the radar, the signal can be written as:

$$E(f, t_D) = \sum_{i=1}^{N} O(x_i, y_i) e^{-2jkx_i \cos(\Omega t_D) - 2jky_i \sin(\Omega t_D)} \tag{2}$$

where Ω is the angular rotation velocity of the target. Note that if the sinusoid functions are simplified under the small observation angle approximation, the range and cross range information can be obtained by Fourier transforming the signal from the frequency and dwell time domain [1]. However, when fast rotating parts exist on the target, eq.(2) no longer hold any more and has to be rewritten to include the scattering from the parts that are rotating at a different velocity. We limit the discussion to the case when only one rotation speed exists for those parts other than the target motion and replace (2) by the following:

$$E(f,t_D) = \sum_{i=1}^{N_b} O(x_i, y_i) e^{-2jkx_i \cos(\Omega_b t_D) - 2jky_i \sin(\Omega_b t_D)} +$$

$$\sum_{i=N_b+1}^{N} O(x_i, y_i) e^{-2jkx_i \cos(\Omega_p t_D) - 2jky_i \sin(\Omega_p t_D)} \qquad (3)$$

where N_b is assumed to be the number of all the scatterers in the target body, Ω_b and Ω_p are respectively the angular velocities of the target body and the fast rotating parts. Usually Ω_p is much greater than Ω_b. In order to image the target, the observation time is chosen to allow the target to be observed for a small range of angles. While the first term in (3) can still be projected to the image of the target via the Fourier transform, the second term results in serious Doppler smearing in the cross range domain and can overshadow the target features. For this reason, the signal should be separated for different motion mechanisms before the regular Fourier processing can be applied.

We shall utilize the adaptive joint time-frequency processing technique to achieve this goal. The algorithm implemented here is very similar to that in our earlier work [8]. The criterion to distinguish the two components of the signal in (3) is according to their different Doppler frequencies versus dwell time characteristics. For the component due to target body scattering, the Doppler frequency is:

$$f_D^b = 2K_c \Omega_b [y\cos(\Omega_b t_D) + x\sin(\Omega_b t_D)] \cong 2K_c \Omega_b (y + x\Omega_b t_D) \qquad (4)$$

It is generally a linear function of dwell time with very small slope and displacement parameters since Ω_b is very small and the small angle approximation can be applied. On the other hand, the Doppler frequency due to the fast rotating parts is basically a sinusoid function of dwell time:

$$f_D^p = 2K_c \Omega_p [y\cos(\Omega_p t_D) + x\sin(\Omega_p t_D)] \qquad (5)$$

Note that both the amplitude and frequency of this sinusoid are scaled by Ω_p. This means the Doppler frequency can either be very large or fast varying versus dwell time. Thus the signal can also be characterized by the linear chirp bases in dwell time-Doppler frequency plane but with either large displacement parameters or large slope parameters. Consequently, if the signal can be fully parameterized by these bases, the component due to the fast rotating parts can be easily separated from the component due to target body motion by sorting them into different categories according to their parameters. This concept is depicted in Fig.1 which displays the different time-frequency behaviors of the signal components due to the steady scattering centers on the target body and the fast rotating parts. To carry out the parameterization and sorting process, we utilize the adaptive joint time-frequency processing technique to be described next.
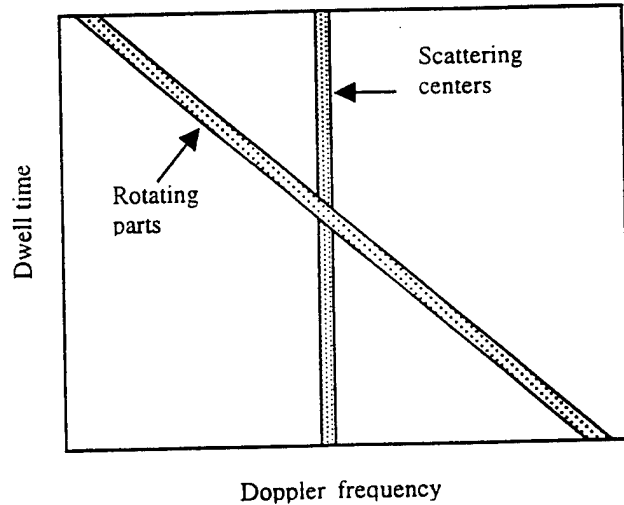
First, the chirp basis functions with linear characteristics in the (dwell time)-(Doppler frequency) plane are constructed with linear and quadratic phase terms:

Fig.1. The time-frequency characteristics of the components due to scattering centers and rotating parts.

$$h_p(t_D) = \exp[-j2\pi(f_0 t_D + \tfrac{1}{2} f_1 t_D^2)] \qquad (6)$$

where the linear phase coefficient f_0 is the displacement parameter in the time-frequency plane and the quadratic phase coefficient f_1 is the slope parameter. We shall process the Doppler signal for each range cell independently instead of for each frequency, since the Doppler smearing due to the rotating parts is often well localized in a finite number of range cells. We

search the chirp basis function which best represents the time-frequency behavior of the signal for each range cell by maximize the projection value of the signal onto the basis:

$$\left| B_p \right|^2 = \max_{f_0, f_1, \dots} \left| \int R_p(x, t_D) h_p^*(t_D) dt \right|^2 \tag{7}$$

where $R(x, t_D)$ is the range profile set obtained by 1-D Fourier transforming the original signal $E(f, t_D)$ from the frequency domain to the range domain. The search for the first-order coefficient can be accomplished by using the FFT algorithm. Then only a one-dimensional search is required to find f_1. This procedure is equivalent to picking out the strongest chirp component of the signal in the time-frequency plane with the resolution of the full Doppler bandwidth. The index p denotes that the signal is at the pth stage of the iterative procedure. This process is repeated for the residue signal which is:

$$R_{p+1}(x, t_D) = R_p(x, t_D) - B_p \cdot h_p(t_D) \tag{8}$$

This search-extract process will be iterated until the energy of the residue signal is smaller than a preset threshold. At this stage, the signal has been fully parameterized as a sum of all these bases. The signal component due to the target body scattering can thus be reconstructed by summing all the bases with small displacement and small slope parameters. In this manner, a clean ISAR image of the target body can be obtained via the standard Fourier processing.

3. NUMERICAL SIMULATION AND EXAMPLES

To test the algorithm, we have simulated the radar scattering from a helicopter model using an electromagnetic prediction code Xpatch which is based on the shooting and bouncing ray technique [11]. The geometry of the helicopter model is shown in Fig.2. There are four blades on the rotor. The length of the blade is 10 feet. The target body is simply made by connecting two conducting boxes, which are respectively 6.56×6.56×6.56 feet and 9.84×3.28×3.28 feet. In the Xpatch simulation, the radar scattering is observed for 128 frequency points from 1.75 GHz to 2.25 GHz, and 128 points in target aspect from 158 degrees to 170 degrees. The elevation angle of the target is 20 degrees. Furthermore, the blade position is articulated between 0 and 360 degrees during the 128 angular looks. The parameters used assume that if the rotation velocity of the target body is 12 rpm, the blade will be spinning at a speed of 30 times that, which is 360 rpm. The standard ISAR image of the target
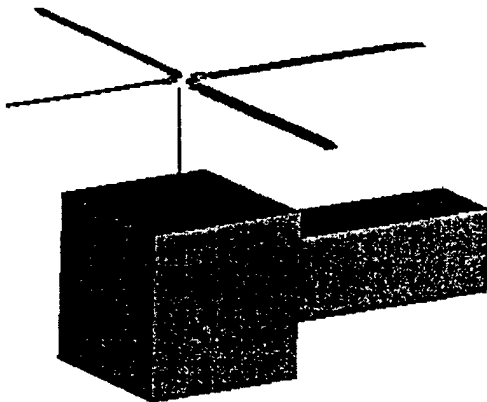

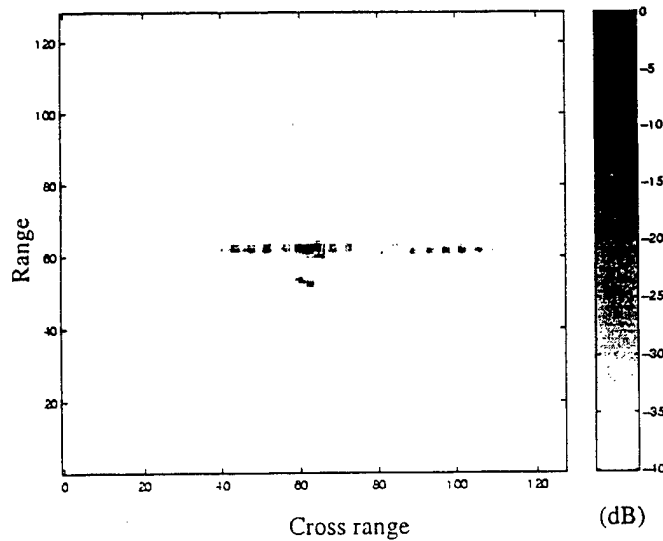Fig.2. Geometry of the helicopter CAD model.

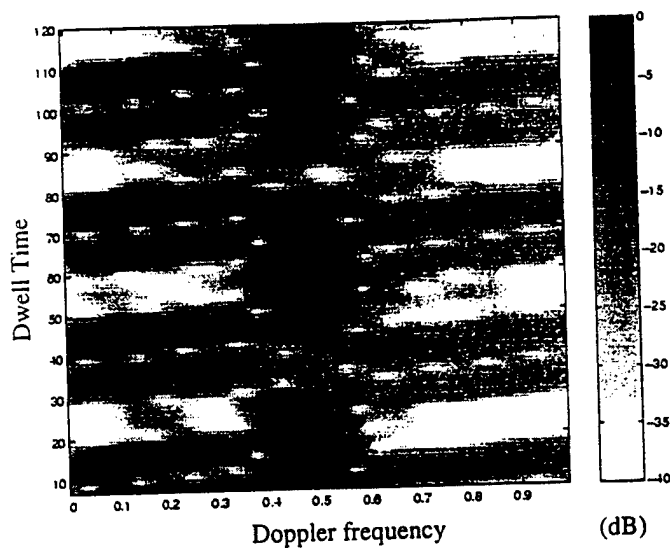Fig.3. Original ISAR image obtained directly via the Fourier transform.

Fig.4. The (dwell time) - (Doppler frequency) spectrogram of the signal at the range cell 53.

Fig.5. The ISAR image obtained by gating out the Doppler component outside the estimated target region.

is obtained via a 2-D Fourier transform as shown in Fig.3. The target body scattering features are confined to a small extent around the center of the cross range, while the scattering components due to the fast rotating blades exhibit strong Doppler smearing lines running across the whole cross range domain and overlapping with the scattering features of the target body. To observe the (dwell time)-(Doppler frequency) behaviors of the signal with Doppler smearing, we choose the range cell 60 and use the short time Fourier transform to display the time-frequency spectrogram in Fig. 4. Although the resolution is poor due to the short-time Fourier transform, we can see there are two kinds of time-frequency behaviors in Fig.4. One component is located around the zero Doppler frequency (the center), which behaves like vertical straight lines with very little slope. It represents the scattering from the scattering centers on the target body. The other time-frequency mechanism is those lines going through the entire Doppler frequency domain. Instead of the sinusoid like time-frequency behavior mentioned in the last section, these lines are the results of serious aliasing effect in the Doppler frequency domain. The aliasing occurs whenever the highest Doppler frequency induced by the fast rotating parts is greater than the radar pulse repetition rate (PRF). Even

Fig.6. The ISAR image after applying the adaptive joint time-frequency processing to remove the Doppler smearing.

though the sinusoid behavior can no longer be seen, the linear chirp description of the time-frequency behavior due to the rotating parts is still effective. The chirp basis functions, however, have to be defined with very large slope parameters to well represent the aliasing effect.
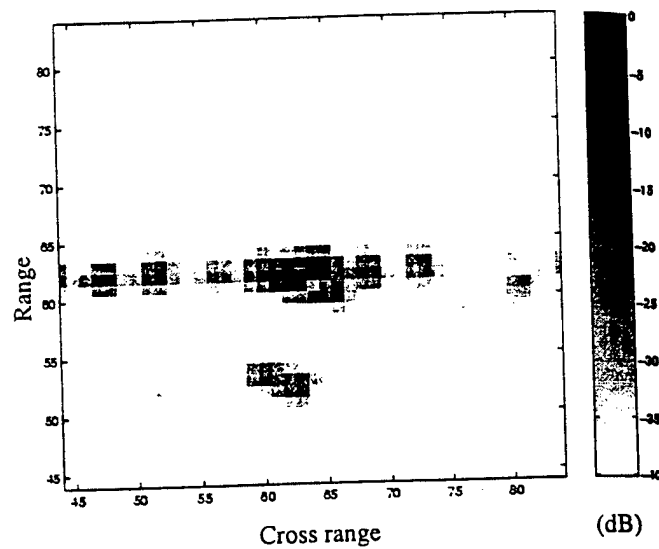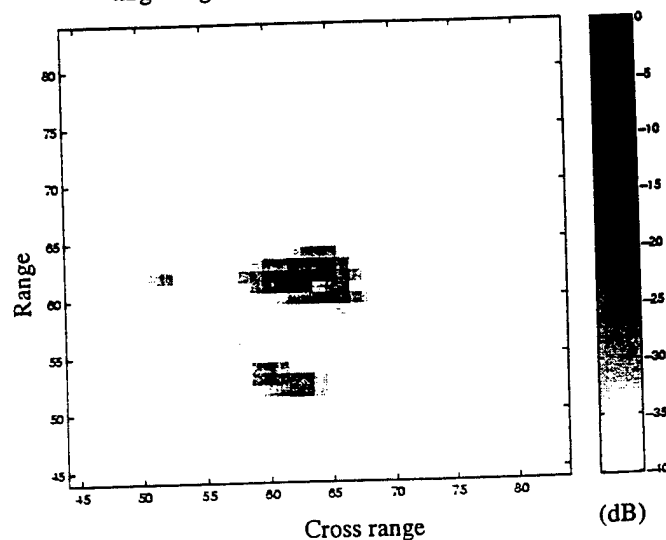
The standard way to remove the Doppler artifact in the ISAR image shown in Fig.3 is to estimate the target dimension and the corresponding Doppler frequency extent, and then gate out the unwanted Doppler frequency components. For this example, we choose a Doppler frequency window which allows about twice of the target dimension and zoom-in on this region. The resulting image is plotted as Fig.5. Note that little is done to eliminate the Doppler smearing that overlaps with the target features. Now the adaptive joint time-frequency processing is applied to the original signal. First we Fourier

transform the original frequency-aspect data to the range-aspect domain. Then for each range cell, the signal is projected to all possible bases until the optimal chirp basis is found and extracted. The procedure is repeated until the residue energy is less than 2% of the energy of the strongest range cell. Usually, it takes less than 200 terms to parameterize the signal with the residue energy less than such a threshold. It has been noted that in the search the slope parameters of the bases should be large enough to represent the dramatic phase variation of the Doppler signals due to the fast rotating parts. After the parameterization is done, the basis functions are divided into two categories according to their slope and displacement parameters. Here we choose an appropriate small number as the threshold of slope. The threshold of displacement is chosen the same as in the standard approach. Only those bases with both the slope and the displacement lower than the thresholds are kept as the components due to the scattering from the target body. Summing up these bases and Fourier transforming it to the image domain, we arrive at a clean ISAR image Fig.6. We observe that most of the Doppler

Fig.7. The ISAR image of the target body simulated without the rotating blades.

smearing is eliminated. To better assess the effectiveness of removing the Doppler smearing, the ISAR image is also simulated for the target without the rotating blades and is shown in Fig.7. From the comparison, it is seen that the algorithm has successfully kept almost all the scattering features due to the target body, but has removed most of the Doppler smearing interference due to the rotating parts from the image. We have also tested the algorithm on measured ISAR data with good success.
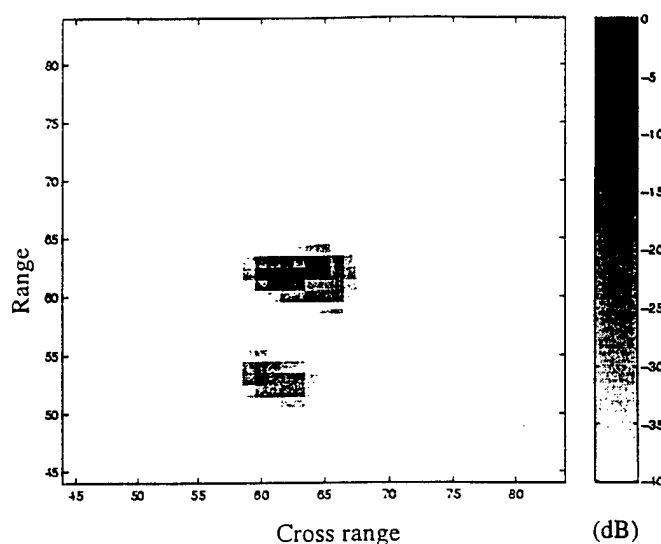
4. DOPPLER INFORMATION EXTRACTION

In the above AJTF processing, the scattering component due to the rotating parts can also be isolated in the process. It consists of the bases with either the slope parameters or the displacement parameters larger than the thresholds. Because the radar PRF is too low to capture the Doppler frequency induced by the fast rotation, the signal is seriously aliased. However, the periodicity of the signal envelope due to the periodic motion of the blades is still available. Usually the observation time period is long enough to observe several periods of the signal envelope. Therefore, a period detection algorithm can be developed to extract the rotation rate of the rotating parts.

The period t_p can be detected by observing the amplitude peaks in the autocorrelation function versus dwell time, which is :

$$f(x,\tau) = \left| \int R_p(x,t_D) \bullet R_p(x,t_D - \tau)dt_D \right| \qquad (9)$$

The peaks will occur at $\tau = n \bullet t_p$, provided the signal is purely from the rotating parts, where n =0, 1, 2, ... For multiple blade rotor, t_p is equal to the ratio of the rotation period and the number of blades. Note the prerequisite of the algorithm is the periodicity of the signal envelope, which means the signal should be due only to the rotating parts to achieve a robust detection. Any signal interference from the target body will degrade the performance of the algorithm. Thus AJTF processing is used here as an effective tool to remove the body interference. To show the advantage of the adaptive joint time-frequency

processing, we applied the algorithm to a set of real measurement result. The measurement is from a helicopter. The autocorrelation function of the original signal versus dwell time is plot in Fig.8. We can barely see any feature from this figure. After the simple gating technique is used to filter out the body component from the original signal, we begin to see some weak peaks in the autocorrelation function plotted in Fig.9, in which it is still hard to determine the period time t_p. The problem of the gating technique is that it not only removed the component due to the target body, but also removed some useful signal component due to rotating blades. The adaptive joint time-frequency processing, on the other hand, keeps the signal component due to rotating blades while removes the component due to the target body. The result is plotted in Fig.10. As it can be seen, multiple sharp peaks occurs at a fixed time interval t_p. This interval is measured to be 0.056 seconds. Therefore, the extracted information indicate that the rotation rate times the number of the blades for this target is equal to 17.7 rps.
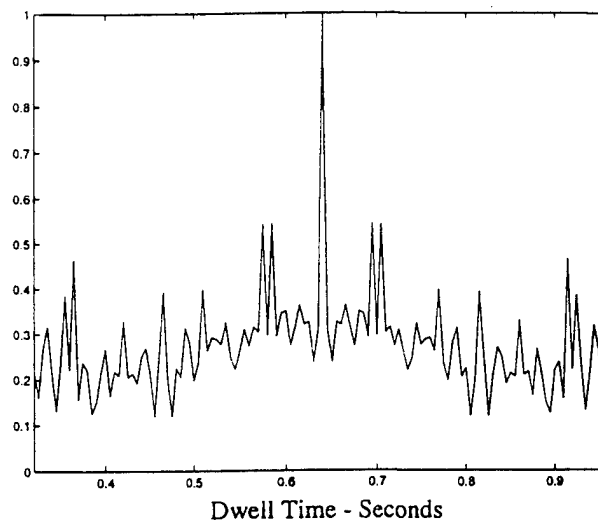
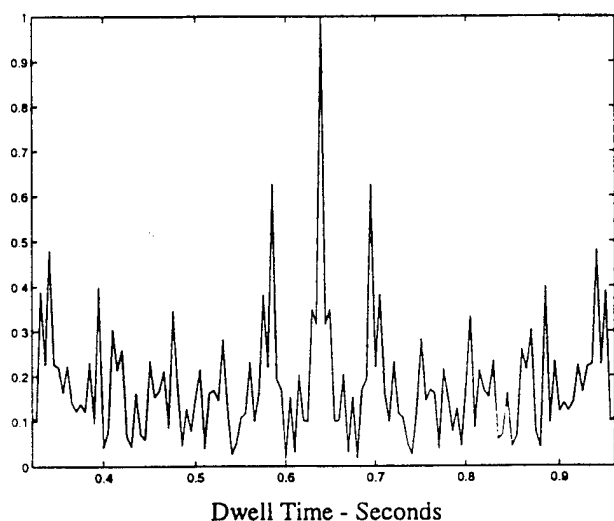Fig.8. The autocorrelation function versus dwell time of the original signal.

Fig.9. The autocorrelation function versus dwell time of the signal with body component gated out.
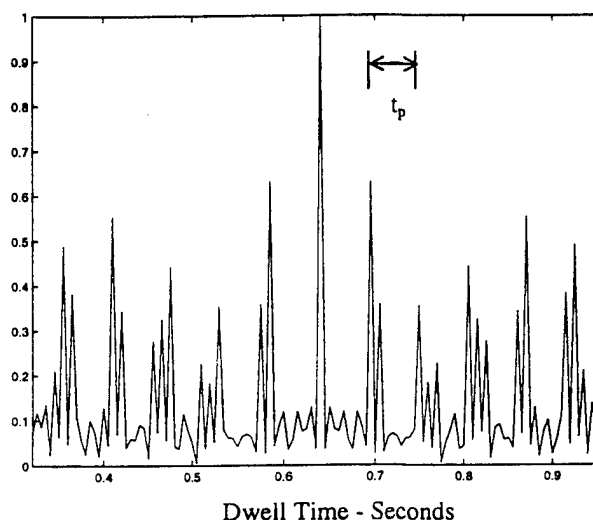

Fig.10. The autocorrelation function versus dwell time of the signal processed by the AJTF technique.

5. SUMMARY

In this paper we have applied the adaptive joint time-frequency concept to separate two different scattering mechanisms, one due to the target body and one due to the fast rotating parts on the target. This is accomplished by taking advantage of their different (dwell time)-(Doppler frequency) behaviors. After adaptively searching for the linear chirp bases which best represent the time-frequency behavior of the signal and fully parameterizing the signal with these basis functions, we can sort these bases into the signal component due to the fast rotating parts and the component due to target body motion according to their slope and displacement parameters. The Doppler smearing interference caused by the fast rotating parts can be removed from the original ISAR image by keeping only those bases associated with target body scattering. The algorithm has been tested for numerical simulated radar scattering data for a helicopter model. The ISAR image obtained by removing the Doppler smearing from the original image agrees well with the image simulated for the target without the rotating blades on. Furthermore, the algorithm has also been applied to eliminate the body interference and extract useful information about the

blade rotation rate from the Doppler signal measured from a helicopter. Comparison with the simple gating technique shows the effectiveness of this algorithm.

ACKNOWLEDGMENTS

REFERENCES

1. D. L. Mensa, *High Resolution Radar Imaging*. Artech House, Dedham, MA, 1981.
2. C. C. Chen and H. C. Andrews, "Target motion induced radar imaging", *IEEE Trans. Aerospace Electron. Syst.*, vol. 16, pp. 2-14, Jan, 1980.
3. A. Ausherman, A. Kozma, J. L. Waker, H. M. Jones and E. C. Poggio, "Developments in radar imaging", *IEEE Trans. Aerospace Electron. Syst.*, vol. 20, pp. 363-400, April 1984.
4. M. R. Bell and R. A. Grubbs, "JEM Modeling and Measurement for Radar Target Identification", *IEEE Trans. Aerospace Electron. Syst.*, vol. 29, pp. 73-87, Jan. 1993.
5. S. Qian and D. Chen, "Signal representation using adaptive normalized Gaussian functions," *Signal Processing*, vol. 36, no. 1, pp. 1-11, Mar. 1994.
6. S. G. Mallat and Z. Zhang, "Matching pursuits with time-frequency dictionaries," *IEEE Trans. Signal Processing*, vol. 41, pp. 3397-3415, Dec. 1993.
7. L. C. Trintinalia and H. Ling, "Extraction of waveguide scattering features using joint time-frequency ISAR," *IEEE Microwave Guided Wave Lett.*, vol. 6, pp. 10-12, Jan. 1996.
8. L. C. Trintinalia, and H. Ling, "Joint time-frequency ISAR using adaptive processing," *IEEE Trans. Antennas Propagat.*, vol. AP-45, pp. 221-227, Feb. 1997.
9. H. Ling, Y. Wang, and V. C. Chen, "ISAR image formation and feature extraction using adaptive joint time-frequency processing," *SPIE AeroSense'97*, 424-432, Orlando, FL, Apr. 1997.
10. Y. Wang, H. Ling and V. C. Chen, "ISAR motion compensation via adaptive joint time-frequency techniques," *IEEE Trans. Aerospace. Electron. Sys.*, vol.34, No.2, pp.670-677, Apr. 1998.
11. R. Bhalla and H. Ling, "A fast algorithm for simulating doppler spectra of targets with rotating parts using the shooting and bouncing ray technique," accepted for publication in *IEEE Trans. Antennas Propagat.*, May 1998.
12. V. C. Chen and S. Qian, "Joint time-frequency transform for radar range-Doppler Imaging," *IEEE Trans. Aeros. Electron. Sys.*, vol.34, No.2, pp.486-499, Apr. 1998.
13. S. Qian and D. Chen, "Decomposition of the Wigner-Ville distribution and time-frequency distribution series," *IEEE Trans. Signal Process.*, vol. 42, pp. 2836-2842, Oct. 1994.
14. J. C. Wood and D. T. Barry, "Radon transformation of time-frequency distributions for analysis of multicomponent," *IEEE Trans. Signal Process.*, vol. 42, pp. 3166-3177, Nov. 1994.

ISAR Image Formation of TIRA Data Using Adaptive Joint Time-Frequency Processing

Hao Ling, Yuanxun Wang, Junfei Li, Rajan Bhalla

Department of Electrical and Computer Engineering
The University of Texas at Austin
Austin, TX 78712-1084
U.S.A.

Summary

We present results of applying adaptive joint time-frequency (AJTF) processing to generate focused ISAR images from the TIRA radar data taken in Germany in November 1997. Our algorithm utilizes the AJTF technique to perform Doppler frequency tracking. By using a search and projection technique in the joint (dwell time)-(Doppler frequency) plane, the prominent point scatterers are automatically selected and tracked. The higher-order translation and rotation motions are then extracted and compensated for in the data to form a focused image of the target. The motion compensated images are compared against the reference images generated by using the motion information available in the instrumented ARDS data. Furthermore, comparison is also made with the simulated ISAR images of the air target from the radar signature prediction code Xpatch. These results provide an assessment of the current capabilities in using high-resolution ISAR imagery for non-cooperative target recognition.

1. Introduction

Inverse synthetic aperture radar (ISAR) imaging is a promising method currently being investigated for non-cooperative target identification (NCTI). The basic framework of ISAR-based NCTI involves the collection of multiple frequency, multiple look data from an unknown moving target. The collected data are processed using motion compensation algorithms to form a focused range-Doppler image of the target. The formed image is then compared against an existing database consisting of either pre-collected measurement or pre-computed synthetic imageries. Some important questions that must be considered in ISAR-based NCTI include: (i) how well can motion compensation processing be carried out to form a focused image of the unknown target, and (ii) what is the quality of the synthetic image predicted using electromagnetic calculations in comparison to the measured data. In this paper, we attempt to address these two issues using the TIRA radar data taken in Germany. Three sets of images are generated. First, we form the motion compensated imagery using an algorithm we have developed previously [1]. It is based on a search and projection technique in the joint (dwell time)-(Doppler frequency) plane to select and track the prominent point scatterers. The higher-order translation and rotation motions are then extracted and compensated for in the data to form a focused image of the target. Second, we form the truth image by using the ARDS (Advanced Range Data System) motion data obtained from GPS sensors installed on-board the air targets. We derive the range and look angle of the target relative to the ground radar based on the ARDS data set. We then utilize this information with interpolation and FFT-processing to obtain a reference image of the target. Third, we generate the synthetic image by using a CAD model of the target and the radar prediction code Xpatch [2]. Xpatch is based on the shooting and bouncing ray technique [3] and accounts for the multiply reflected returns from a target. The three methods of generating the images are detailed in Sections 2, 3 and 4. We then present some quantitative comparisons between these images and draw some conclusions in Sections 5 and 6.

2. Motion Compensated Image

To form a focused image from the raw TIRA data, we first carry out a coarse alignment of the data in the range dimension, followed by fine motion compensation in the cross range dimension. 128 pulses are used to form the image at each look angel. During the coarse alignment, we correlate the range profiles among pulse numbers. The resulting range shifts between pulses are then fitted to a low-order polynomial to derive a more accurate target range function versus pulse number. This function is used to align the range profiles. Next, fine motion compensation is carried out using an adaptive joint time-frequency algorithm [1]. First, we select the range cell

containing the brightest scatterer. Due to translation motion, the Doppler frequency versus dwell time behavior of the point scatterers within this range cell is not constant in the joint time-frequency plane (see Fig. 1). To find the motion parameters, we project the response within the -range cell to basis functions of the form

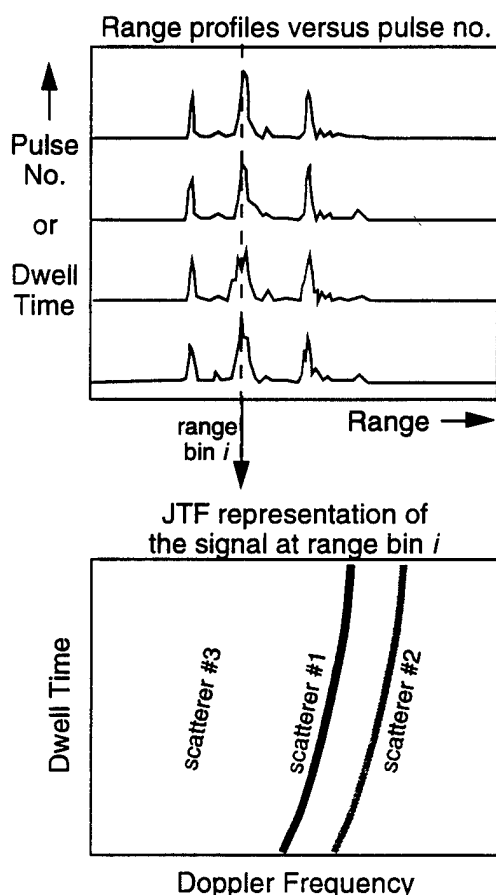$$h(t) = \exp\left[-j2\pi(ft + \tfrac{1}{2}f't^2 + \tfrac{1}{3}f''t^3 + \ldots)\right]$$

Range profiles versus pulse no.

Fig. 1. Fine motion compensation is carried out by extracting the Doppler frequency versus dwell time behavior of the strong point scatterer in the signal.

where t denotes dwell time (or pulse number). By varying f, f' and f'' and searching for the maximum projection value, the basis function which best resembles the joint (dwell time)-(Doppler frequency) behavior of the strongest point scatterer in the range cell can be found. For TIRA data, we use polynomials up to the third order in the phase function of the basis. The search of the first order coefficient f can be accomplished by using an FFT algorithm, while a brute-force search is needed to find the higher order coefficients f' and f''. Since the higher order phase terms in the basis correspond to phase errors cause by the motion, we can multiply the conjugate of this basis function to the original signal to eliminate the translation motion from it. This algorithm can also be extended to

multiple range cells to correct for higher order rotation motions, although we did not find them to be significant. Shown in Figs. 3(a), 4(a) and 5(a) are the motion compensated images from the TIRA data at three different look angles processed using the above motion compensation algorithm.

3. Reference Image Based on ARDS Motion Data

Several targets within the TIRA data set carried on-board GPS sensors to record the position and motion of the aircraft. The data were processed and written in the ARDS file. We form images based on the ARDS data set and use them as a reference to evaluate the quality of the motion compensated images described in the last section. The ARDS data set provides sensor-derived range and orientation information (yaw, pitch and roll) of the target. We use the range information to carry out range alignment after first synchronizing the GPS time and the radar collection time. The range data are then fitted to a low-order polynomial in the same manner as the coarse motion compensation procedure. The resulting range
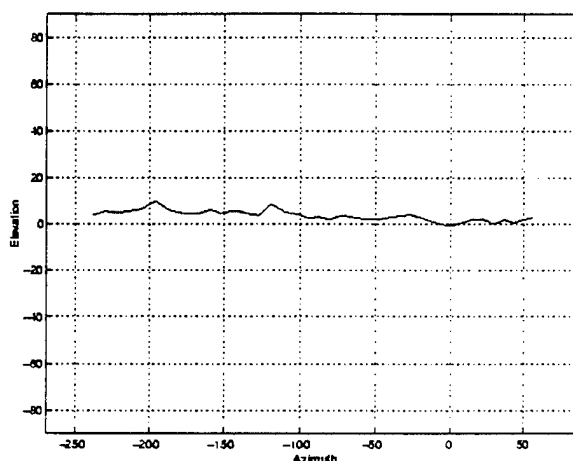

Fig. 2. Elevation and azimuth look angels on a TIRA target during its flight.

function is used to align the range profiles over pulse numbers. To carry out Doppler alignment, the target orientation (yaw, pitch and roll) is first transformed into the radar look angle on target in terms of elevation and azimuth. Fig. 2 shows the elevation and azimuth look angles on a target during the dwell history of 11.7 minutes. It can be seen that in this case the elevation angle is near zero during the entire flight. Given the relative constant elevation angle over the entire data collection time, we perform Doppler focusing by assuming only azimuth variation. Since the imaging plane is the zero-elevation plane under this condition, the expected 2D ISAR images will be the top view of the aircraft. The azimuth versus dwell time information is

first fitted to a low-order polynomial and the resulting function is used to reformat the data from uniform sampling in dwell time to uniform sampling in azimuth angle. FFT processing is then applied to form the image. Figs. 3(b), 4(b) and 5(b) show the reference images derived from the ARDS motion data for the same target at the same looks as those shown in Figs. 3(a), 4(a) and 5(a). 128 pulses are used to form the images.

4. Synthetic Image from Xpatch Simulation

We simulate the synthetic imagery based on a CAD model of the target and using the radar simulation code Xpatch [2]. The CAD model consists of a facetized version of the target. In the Xpatch simulation, geometrical optics rays are shot from the incident look angle and all the multiple reflections are tracked until the rays exit the target. The image is formed by updating the ISAR image plane one ray at a time using its ray-spread function. A fast FFT-based algorithm is next used to accelerate the ray update time. This fast image formation algorithm is based on a single ray trace and is orders of magnitude faster than the conventional multi-frequency, multi-aspect ray calculation. It has been found from validation studies that this method leads to a more focused image than the conventional frequency-aspect approach. However, the key image features are fairly well predicted by this algorithm. The detailed description of the algorithm can be found in [4] and [5]. The typical simulation time per image (carried out at a ray density of 10 rays/wavelength) for a faceted aircraft model at Ku band is approximately 30 minutes on an SGI O2 workstation. The simulation time is dominated by the ray tracing operation. The single diffraction contribution from edges can also be computed in the same manner using Xpatch. However, we did not include it in our calculations. Figs. 3(c), 4(c) and 5(c) show the results of the Xpatch simulation for the same target at the same set look angles as the measured images. Both the down range and cross range resolutions in the simulation are adjusted to correspond to the measured data.

5. Image Comparisons

We have processed the images of a TIRA target over its flight duration of 11.7 minutes. Three sets of representative examples are shown here. Figs. 3(a), (b) and (c) are the images of the target at azimuth=146° (0° being nose-on) generated using, respectively, motion compensation, ARDS sensor information and Xpatch simulation. The dynamic range of the displayed images is 55 dB. Figs. 4(a), (b) and (c) are the images of the target at azimuth=-56° obtained by the three methods. Figs. 5(a), (b) and (c) are the images of the target at azimuth=30°. The look angle information was deciphered from the ARDS data. We make the following observations:

(1) The motion compensated images and the ARDS-derived reference images appear to be in good agreement over most angles. Surprisingly, the motion compensated images are better focused than the reference images. We attribute this to the finite accuracy of the GPS sensors, which is estimated to be about 6 cm. Since this inaccuracy amounts to several wavelengths at Ku band, we believe the motion data did not provide sufficient accuracy for forming a well-focused image. On the other hand, we found that the performance of our motion compensation algorithm depends on the availability of a clear point scatterer in the selected range cell. A general criterion should be further developed to automatically select the range cell that contains a strong, well-isolated point scatterer. Shown in Fig. 6(a) is the correlation coefficient between the two sets of images over 40 looks that almost cover the entire azimuth scan on the target. The correlation coefficient is normalized between zero and one and is computed based on the image intensity with a power transform of 0.5. We observe that the correlation coefficient is on the order of 0.9 over the azimuth sweep.

(2) The Xpatch simulation and the ARDS-derived reference images show fairly good agreement in the prominent target features. As expected, the Xpatch images are more focused and do not exhibit the diffused characteristics of the measurement data. This observation is consistent with other data sets we have studied in the past. We also observe that in the frontal look region of the aircraft, the measured images contain strong jet engine modulation (JEM) lines as shown in Fig. 5. This effect is not predicted in the Xpatch simulation. Fig. 6(b) shows the correlation coefficient between the two sets of images as a function of azimuth angle. The correlation between the synthetic data and the measured reference data is on the order of 0.4 to 0.5. Near the frontal region (±50°), the correlation is lower due to JEM effects in the measured data. We have recently developed a methodology to predict JEM lines using Xpatch [6]. However, this effect is strongly dependent on the engine spin rate relative to the radar pulse repetition frequency and an accurate prediction is difficult.

6. Conclusions

We have reported some preliminary results from processing the TIRA measurement data. We have applied the adaptive joint time-frequency motion compensation to form ISAR imageries of TIRA targets. The results compared favorably with the reference images formed using the ARDS motion data. It was found that the quality of the reference image is slightly inferior to the motion compensated image due to the accuracy limit of the GPS sensors. While the motion compensation algorithm performed quite adequately in this instance, the target under consideration did not exhibit significant higher-order rotation motion. Faster maneuvering targets may pose more of a challenge to the motion compensation

algorithm. Also, we have arbitrarily chosen 128 pulses to form the images. We will investigate the use of longer dwell time in the image formation process to achieve better cross range resolution and extract absolute cross range scaling.

We have also generated the synthetic images of the target and compared the synthetic results to the reference images from the TIRA data. It was found that a fairly good agreement was achieved using Xpatch in predicting the prominent target features. A higher-fidelity CAD model should further improve the quality of the synthetic data. Within the frontal sector of the target, strong JEM lines in the measured images significantly corrupted the geometrical features on the target. We are pursuing algorithms for removing such artifacts from the measured data to unmask the geometrical features of the target [7].

Acknowledgment

References

[1] Y. Wang, H. Ling and V. C. Chen, "ISAR motion compensation via adaptive joint time-frequency technique," *IEEE Trans. Aerospace Electronic Sys.*, vol. AES-34, pp. 670-677, Apr. 1998.

[2] D. J. Andersh, M. Hazlett, S. W. Lee, D. D. Reeves, D. P. Sullivan and Y. Chu, "*Xpatch*: A high frequency electromagnetic-scattering prediction code and environment for complex three-dimensional objects," *IEEE Antennas Propagat. Mag.*, vol. 36, pp. 65-69, Feb. 1994.

[3] H. Ling, R. Chou and S. W. Lee, "Shooting and bouncing rays: calculating the RCS of an arbitrarily shaped cavity," *IEEE Trans. Antennas Propagat.*, vol. AP-37, pp. 194-205, Feb. 1989.

[4] R. Bhalla and H. Ling, "Image-domain ray-tube integration formula for the shooting and bouncing ray technique," *Radio Science*, vol. 30, pp. 1435-1446, Sept.-Oct. 1995.

[5] R. Bhalla and H. Ling, "A fast algorithm for signature prediction and image formation using the shooting and bouncing ray technique," *IEEE Trans. Antennas Propagat.*, vol. AP-43, pp. 727-731, July 1995.

[6] R. Bhalla and H. Ling, "A fast algorithm for simulating Doppler spectra of targets with rotating parts using the shooting and bouncing ray technique," *IEEE Trans. Antennas Propagat.*, vol. AP-46, pp. 1389-1391, Sept. 1998.

[7] Y. Wang, H. Ling and V. C. Chen, "Application of adaptive joint time-frequency processing to ISAR image enhancement and Doppler feature extraction for targets with rotating parts," SPIE 43rd Annual Meeting, Radar Processing, Technology, and Applications, pp. 156-163, San Diego, CA, July 1998.
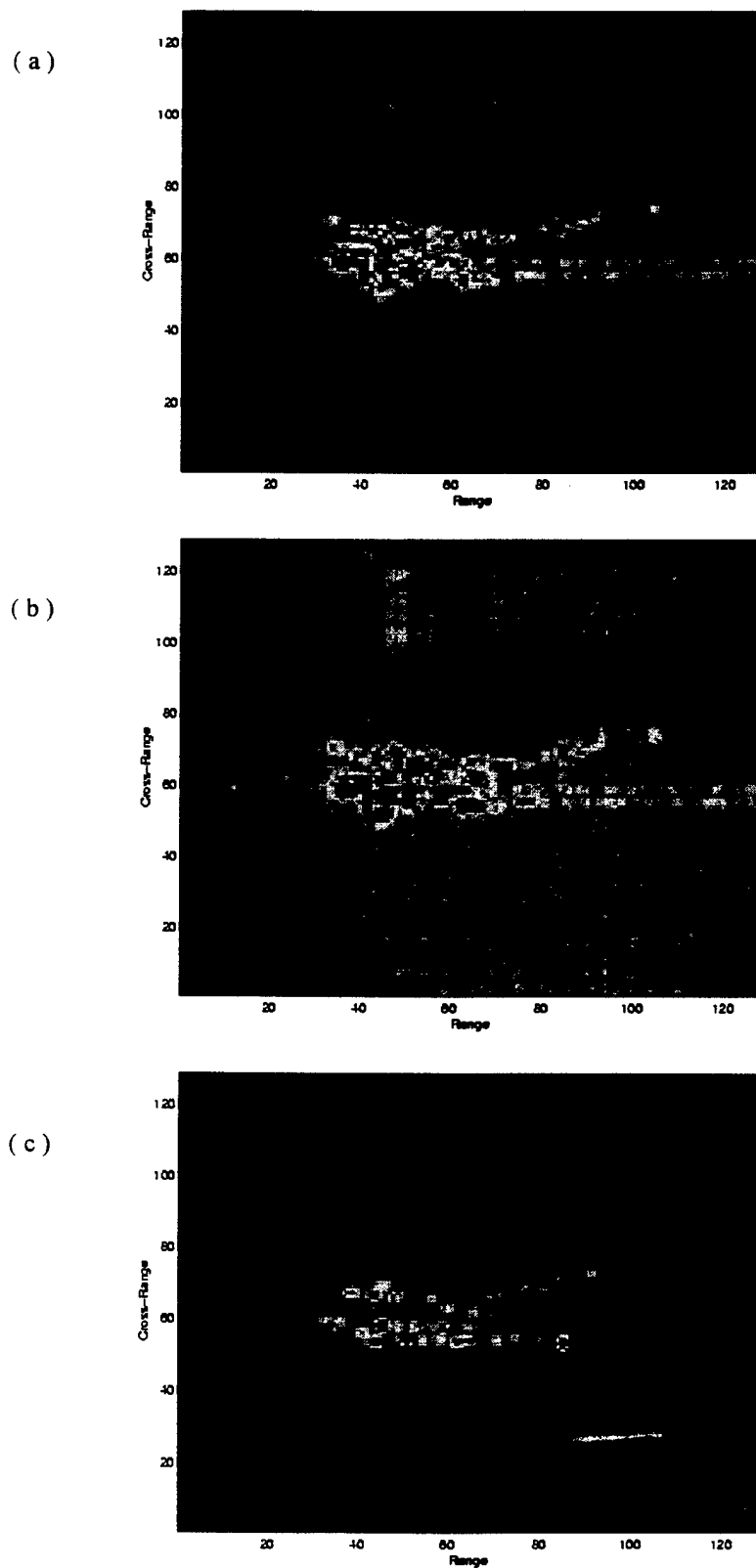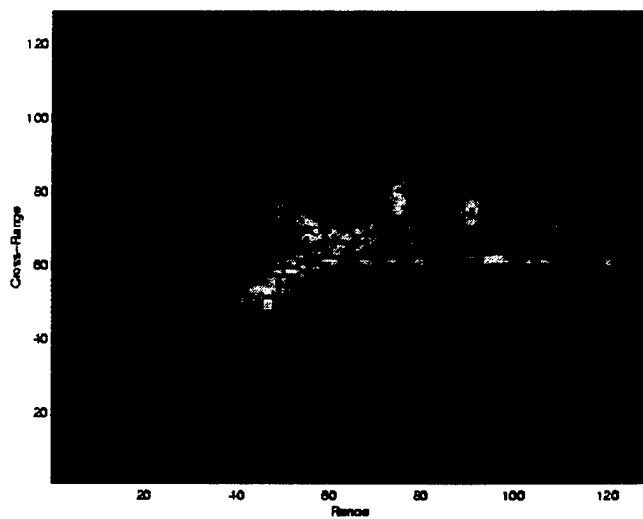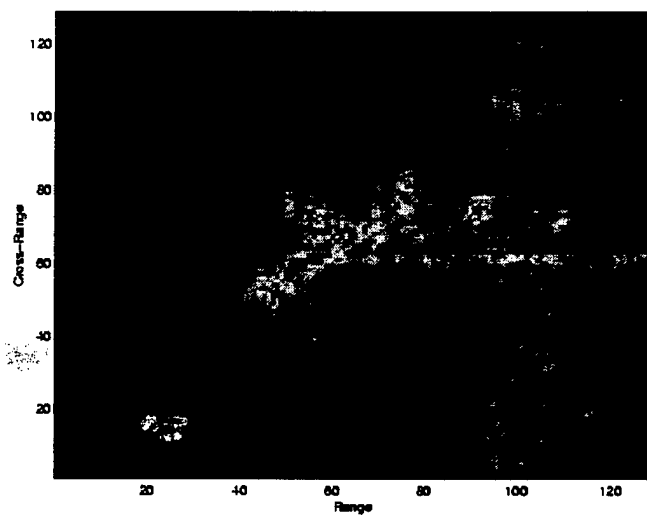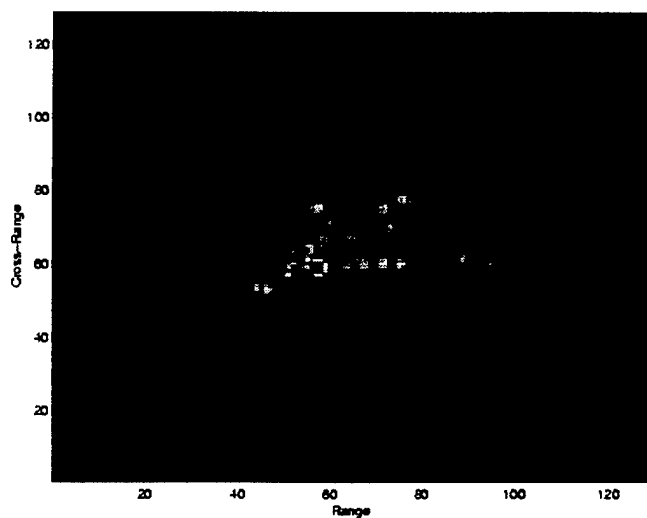
Fig. 3.   A TIRA target at azimuth=146°.

(a) Motion compensated image using AJTF processing.

(b) Reference image based on ARDS motion data.

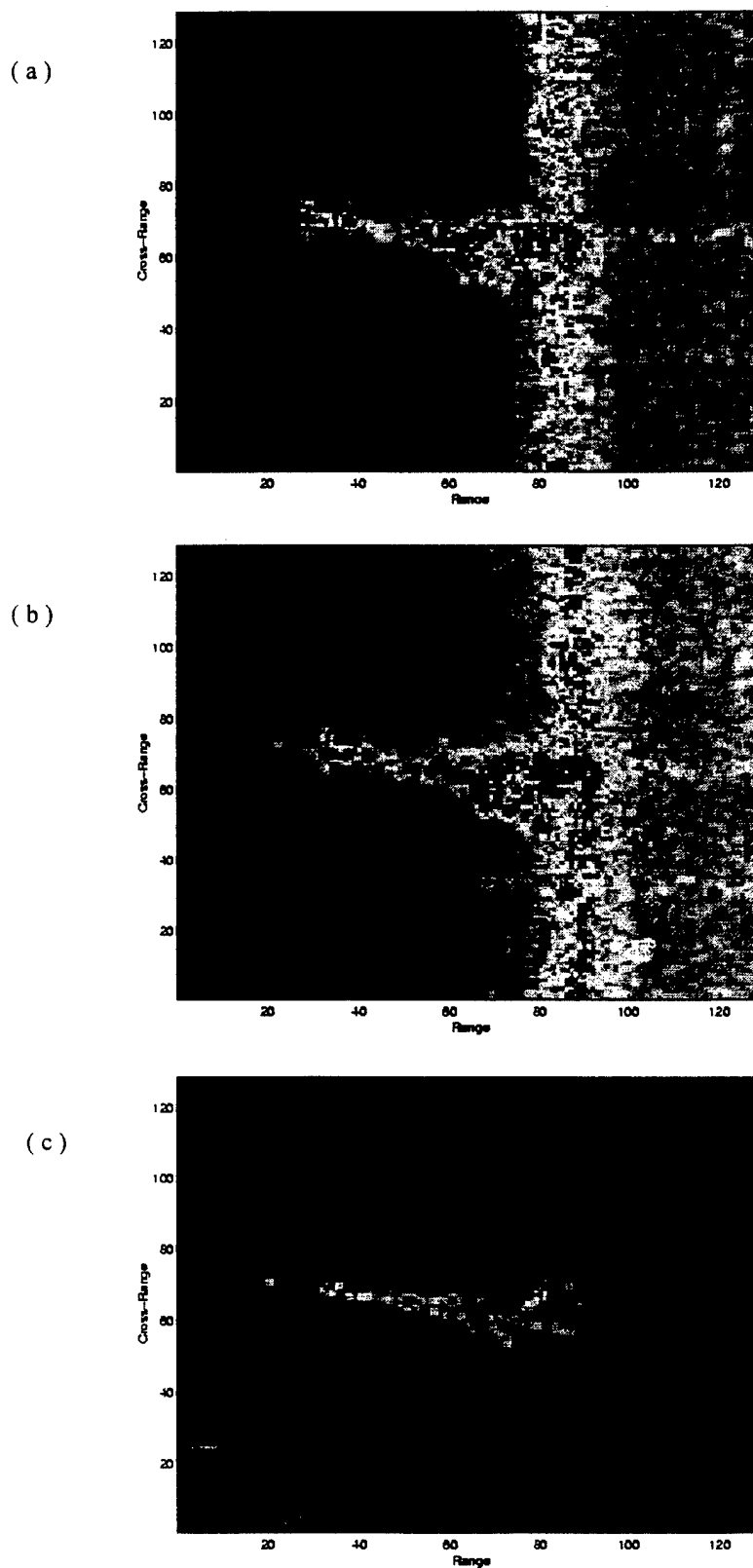(c) Synthetic image from Xpatch simulation.

Fig. 4.   A TIRA target at azimuth=-56°.
         (a) Motion compensated image using AJTF processing.
         (b) Reference image based on ARDS motion data.
         (c) Synthetic image from Xpatch simulation.

Fig. 5.   A TIRA target at azimuth=30°.
(a) Motion compensated image using AJTF processing.
(b) Reference image based on ARDS motion data.
(c) Synthetic image from Xpatch simulation.
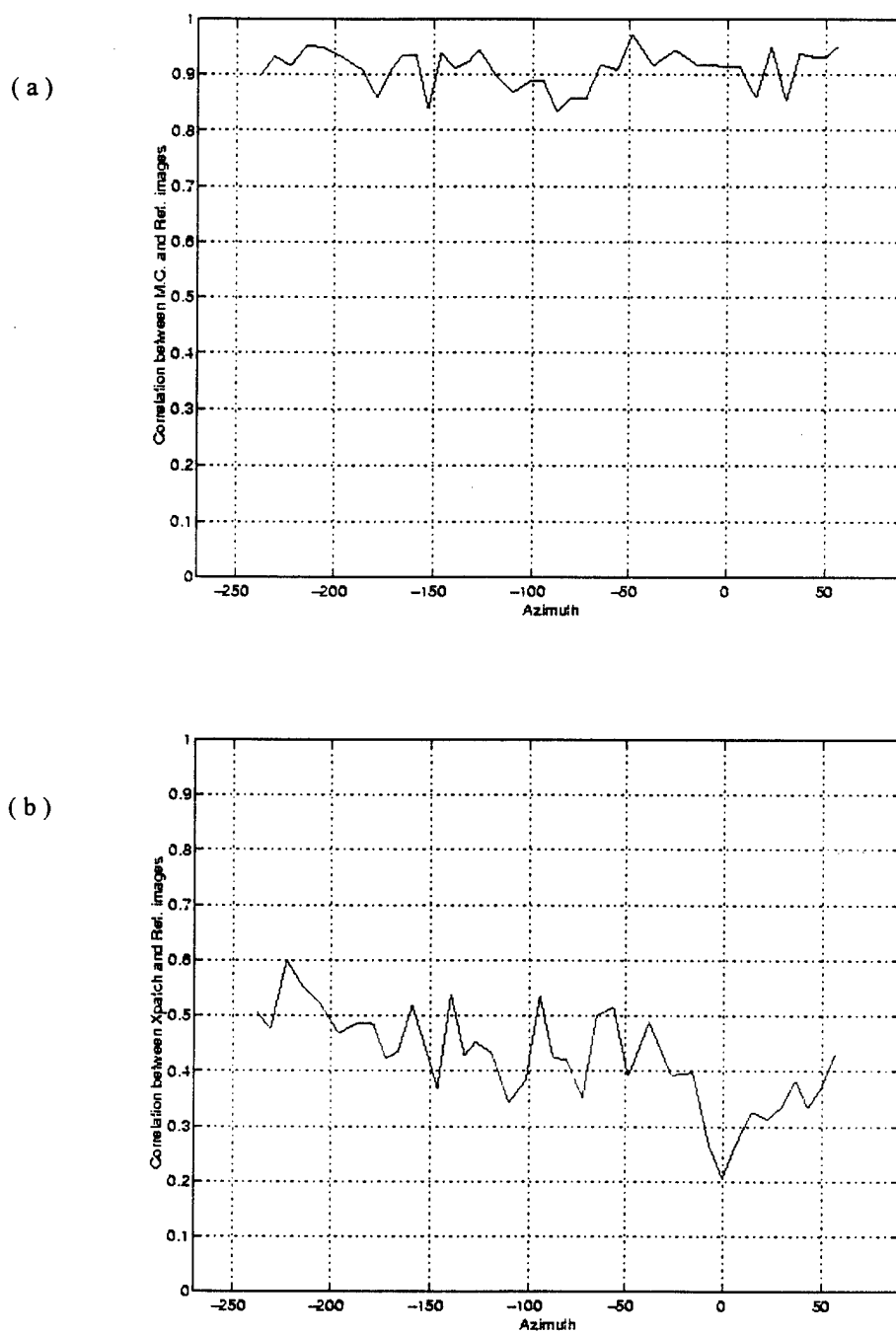
(a)

(b)

Fig. 6. Correlation coefficients versus azimuth look angle between:
(a) Motion compensated images and ARDS-derived reference images.
(b) Xpatch simulated images and ARDS-derived reference images.

Clutter Reduction for Synthetic Aperture Radar Images Using Adaptive Wavelet Packet Transform

Hai Deng[*] and Hao Ling
Department of Electrical and Computer Engineering
The University of Texas at Austin
Austin, TX 78712-1084

1.Introduction

Synthetic Aperture Radar (SAR) images of ground targets generally consist of target features and clutters from background scattering [1]. In automatic target recognition (ATR) applications, it is desirable to remove the clutter from the actual target images before ATR processing. The standard way to suppress clutter is to apply an appropriate threshold level to the whole SAR image to remove the clutter. However, this approach assumes that the target signal-to-clutter ratio (SCR) is large enough, otherwise results in either some target feature loss or remnant clutter residue. In this work, we set out to develop a decluttering algorithm to automatically extract the target image from a SAR image by maximizing SCR using the adaptive wavelet packet transform (AWPT) [2]. The wavelet packet basis is the generalization of the conventional wavelet basis [3] and has been applied for image compression [4] and moment matrix sparsification [2].

Our approach is to transform the SAR image to a new domain using an appropriately chosen set of wavelet packet basis. Since a typical target image usually consists of point scatterers and region features, which are respectively high frequency and low frequency signals, the multi-scale wavelet basis is well suited to focus the target image. Clutter image, on the other hand, is statistically uncorrelated from pixel to pixel. Therefore, the transformed clutter image under the same set of bases should remain uncorrelated. We therefore expect that the SCR can be increased in an appropriately chosen set of basis. The cost function of our AWPT algorithm is chosen to describe how well the target signal is focused in the transform domain. An efficient basis search algorithm is implemented to find the best wavelet packet basis. Our algorithm is tested using the MSTAR SAR data set [5] and show that an improved SCR can be achieved using the algorithm.

2. SAR Image Representation with Wavelet Packet Basis

A discrete SAR image s(m, n) can be represented as:

$$s(m,n) = t(m,n) + c(m,n) \quad 0 \le n, m < N \tag{1}$$

where t(m, n) and c(m, n) denote the target image and the clutter in the SAR image, respectively. We define a set of orthogonal and complete 2-D wavelet packet basis functions:

$$\{U_{p,q}^{j}(k,l) \quad 0 \le j < J, \ 0 \le p,q < 2^{j}, \ 0 \le k,l < N2^{-j}\} \tag{2}$$

where j denotes the scale index, and $J = \mathrm{Log}_2(N)$; p, q are the modulation indices; and k, l are the position indices. The 2-D wavelet packet basis function can be generated from the product between two 1-D wavelet packet bases:

$$U_{p,q}^{j}(k,l) = \psi_{p}^{j}(k)\psi_{q}^{j}(l) \tag{3}$$

ψ is a 1-D wavelet packet basis that can be generated from the scaling function and the basic wavelet function using the "2-scale equation" [2-4].

The transformation of a SAR image s(m, n) using the wavelet packet basis is:

$$\tilde{S}_{p,q}^{j}(k,l) = \sum_{m}\sum_{n} s(m,n)U_{p,q}^{j}(k - 2^{j}m, l - 2^{j}n)$$

$$= \sum_{m}\sum_{n} t(m,n)U_{p,q}^{j}(k - 2^{j}m, l - 2^{j}n) + \sum_{m}\sum_{n} t(m,n)U_{p,q}^{j}(k - 2^{j}m, l - 2^{j}n)$$

$$= \tilde{T}_{p,q}^{j}(k,l) + \tilde{C}_{p,q}^{j}(k,l) \tag{4}$$

where $\tilde{T}$ and $\tilde{C}$ are the transform coefficients of the target image and the clutters in the image with the wavelet packet basis.

If we define SCR of a SAR image as the ratio of average target amplitude to the standard deviation of the clutter, the SCR of the image before and after the transform are $\bar{t}/\sigma(c)$ and $\tilde{\bar{T}}/\sigma(\tilde{C})$ respectively. The clutters function c(m, n) denotes the reflectivity of different resolution cells in the highlighted background areas, and are independently and identically distributed [6]. It can be shown that their wavelet packet transform coefficients $\tilde{C}$ are still uncorrelated [7], and the standard deviation of clutter does not change after the basis transform. But the signals from target area are related to themselves, it is possible to increase target amplitude with a basis transformation. Therefore, with a specific SAR image we need to find the best wavelet packet basis to maximize the transformed target image magnitude adaptively.

3. Adaptive Search Procedure and Implementation

To find the best wavelet packet basis and implement the basis transform, we need to define a cost function to describe how well the transformed target signal is concentrated with a wavelet packet basis. The best basis is the one that makes the transformed signal have the minimum cost. The most commonly used cost function is the entropy function. Because of the complexity of evaluating entropy function, we use energy concentration function as cost function in this application. For a transformed SAR image it is defined as:

$$Cost = \sum_{j,p,q}\sum_{k,l} \left| \tilde{S}_{p,q}^{j}(k,l) \right|^{P} \quad 0 < P < 2 \tag{5}$$

Because there are many possible wavelet packet bases in (2) for the transform, it is impractical to try each of them to find the best basis. An effective Quad-tree decomposition algorithm was generalized from that proposed in [8] to find the best 2-D wavelet packet basis with regard to an additive cost function. The algorithm decomposes the original image using 2-channel filtering with a pair of Quadrature filters stage by stage from spatial domain to spectrum domain. With cost labeled at every stage, the decomposition tree is searched from the last stage to the first stage. The best decomposition tree can be found after the search

process with total computational complexity of about $O(N^2 \log N)$ for the algorithm. A scale-dependent threshold is applied to the transformed image. Because there is a weak correlation between clutter samples, we increase threshold level slightly as the scale increases. The threshold level is chosen as:

$$Th_j = K\sigma_c \sqrt{j/J} \qquad (6)$$

where j is the scale index, J is the maximum scale, σ_c is the clutter standard deviation, and K is a constant. With the thresholding processing, most clutters are removed in the wavelet packet basis domain, and the image is inverse-transformed back to spatial domain to restore the original target image using the same tree for decomposition. Although SCR is much improved in the restored image, it is impossible to remove the clutter completely through that processing. We apply a very small second threshold to the restored image, and then clustering processing to get rid of all clutter residues.

4. Test Results

To test the effectiveness of the processing scheme, we apply it to the MSTAR SAR image data. Fig. 1 shows one of MSTAR images in which target is a ground vehicle with vegetation clutters. There are several strong point scatters in the front of the vehicle, but the reflection from the back part is relatively weak. With direct thresholding processing, as demonstrated in Fig.2, some crucial parts of the target are lost. However, if we apply the AWPT algorithm to the same image, the restored image is shown in Fig. 3. All key features of the original image are kept through the processing. We chose Daubechies filter with order of 6 as wavelet filter, the first threshold parameter is 1 and the second threshold is $0.05\sigma_c$. In both processing methods, there is some target information loss. Fig. 4 shows the signal-to-clutter ration with average target amplitude loss for the two processing methods. It is observed that for a fixed target image loss the new AWPT method always achieves a higher SCR value than the traditional direct thresholding processing. Similar results are obtained when the algorithm is applied to other MSTAR data.

References

[1] D. R. Wehner, *High Resolution Radar,* Artech, Norwood, MA, 1995.

[2] H. Deng and H. Ling, "Fast solution of electromagnetic integral equations using adaptive wavelet packet transform," to appear in *IEEE Trans. Antennas Propagat., 1999.*

[3] C. K. Chui, *An Introduction to Wavelets.* Academic Press, New York, 1992.

[4] R. R. Coifman, Y. Meyer, and M. V. Wickerhauser, "wavelet analysis and signal processing." In *Wavelets and their applications,* pp. 153-178, Jones and Barlett, Boston, 1992.

[5] MSTAR SAR data set, Wright Lab., 1996.

[6] H. L. Van Trees, *Detection, Estimation, and Modulation Theory, Part III,* Wiley, New York, 1971.

[7] P. Moulin, "A wavelet regularization method for diffuse radar-target imaging and speckle-noise reduction," *J. Math. Imag. and Vision,* pp. 123-134, No. 3, 1993.

[8] R. R. Coifman, and M. V. Wickerhauser, "Entropy-based algorithms for best basis selection," *IEEE Trans. Info. Theory,* Vol. 38, pp.713-718, March 1992
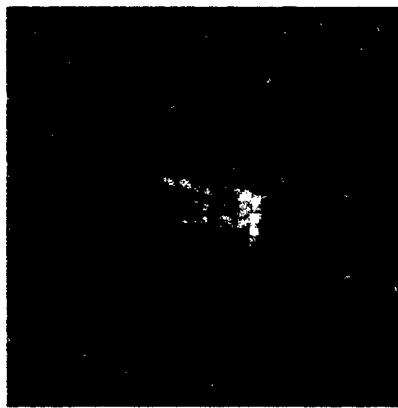
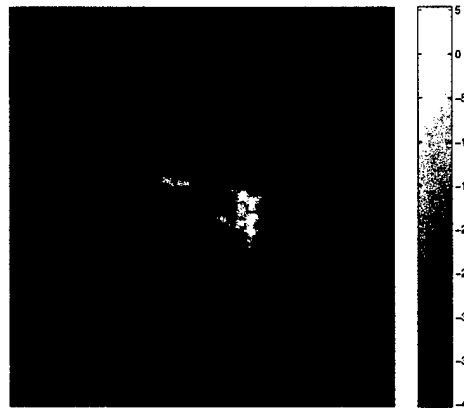Fig. 1. SAR image of a ground vehicle with clutter

Fig. 2. Clutter rejection using direct thresholding method
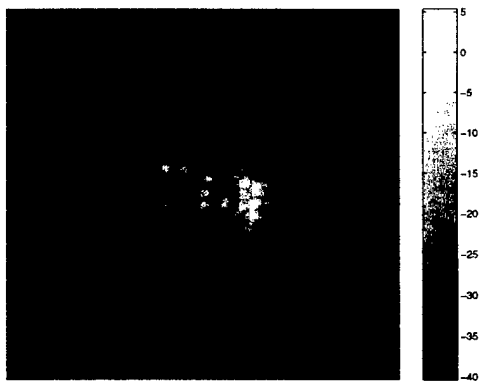

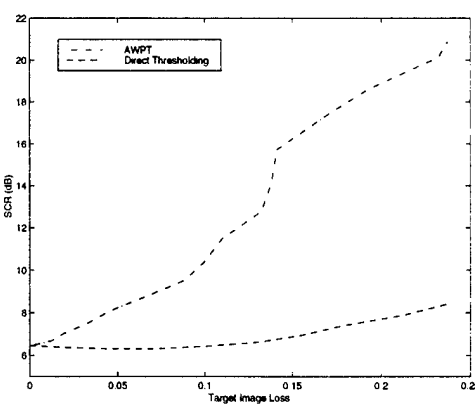Fig.3. Clutter rejection using AWPT method

Fig. 4. SCR vs. target image loss for the two processing methods.